THE UNIVERSITY of ADELAIDE

The effect of solid particle recirculation on the efficiency of a cavity-type solar receiver

Md. Rabiul Islam Sarker

School of Mechanical Engineering

The University of Adelaide

South Australia 5005

Australia

A dissertation submitted in fulfilment of the requirements for the degree of Ph.D. in Engineering

on the 12th March, 2015

PhD Thesis

Final version

12th March 2015

Thermo-fluid group

School of Mechanical Engineering

The University of Adelaide

South Australia 5005

Australia.

Typeset by the Author using MS Office 2010

Printed in Australia

To my late parents

Abstract

High temperature steam or gas is used as the working medium for operation in advanced power conversion units, such as gas turbines or combined cycle power plants. The use of Concentrated Solar Power (CSP) technologies for energy generation relies on the heating of fluids to high temperatures. Conventional tubular or porous absorber volumetric receivers usually suffer from a relatively low thermal efficiency, less than 70%, and from high thermal losses. The solid particle solar receiver, in which the incoming solar radiation is directly absorbed by the solid particles and inner walls of the cavity receiver, promises to achieve higher thermal efficiency due to the enhanced heat transfer to the working fluid and the reduction in thermal losses. The main challenge in designing a high temperature solar receiver is to maximize the solar energy absorption and its efficient transfer to the working fluid, e.g. air. The objective of this research project is to characterize the thermal behaviour of a proposed cavity-type solar receiver concept based on the application of recirculating solid particles to achieve high temperature outlet air. In this concept, solar energy is absorbed by recirculating solid metallic particles, which, at the same time, transfer the absorbed thermal energy to the surrounding air in a cavity-type receiver. The cavity-type solid particle receiver is a well-insulated enclosure, designed to capture the incident solar radiation effectively, which allows the incident radiation directly through an aperture.

In this study, a well-insulated cavity-type enclosure was designed and constructed. The designed solar receiver consisted of an externally insulated cylindrical cavity with a circular aperture at the top covered by a quartz glass, a recirculating fan installed at the bottom of the chamber and with an inlet and an outlet installed on the chamber wall. A series of experiments were conducted to characterize the fluid dynamics and thermal behaviour of the solar receiver. The results showed that the direction of the total air flow velocity was vertically

upward from the outer periphery of the fan and vertically downward through the centre of the receiver. The measured air flow velocity was normalized by against the particle terminal velocity. The results showed that the normalized flow velocity was 3 times higher than the particles terminal velocity and 45 times higher than the minimum fluidization velocity of particles for the same case. Hence the particle can be recirculated in the cavity. The particles' concentration at different regions of the solar receiver was also measured using a laser-based light-scattering technique. Black SiC of 70micron and 200micron SiC particle were used during this experiment. The effect of particle size and fan RPM on the particle concentration at different regions of the solar receiver was optimized using the test results of the particle concentration measurements.

At an RPM of 1250, the measured opacity of the particle cloud's concentration was 0.95 for 70micron and 0.80 for 200micron particle at a specific freeboard height of the cavity. It is an indication that particles' concentration and opacity at a different region is dependent on the particle size and air flow velocity. The results showed that the particle concentration and opacity increased exponentially with the RPM. The opacity is a measure of the irradiation penetration characteristics of the Xenon arc radiation beam into the cavity.

The calculation of Stokes number and turbulence intensity from these measurements helped in understanding the slip velocity and velocity fluctuation of air and particles in the cavity. The maximum Stokes number was 0.50 for 70micron particle whereas it was 4 for 200 micron particle measured at 500RPM. Hence, when comparing the Stokes numbers it becomes clear that the slip velocity was higher for 200micron particles which denote more interaction with air. Turbulence intensity measurement showed that an average turbulence intensity of 38% was observed near the cavity wall and 30% at the centre of the cavity. Therefore, a better forced convection heat transfer was expected between the particle, air and cavity wall surface in the proposed receiver.

Finally a thermal test was performed to assess the thermal performance of the designed solar receiver. Black SiC and brown alumina particles at two sizes (70 and 200microns) were used in these experiments. The results showed that the air temperature in the solar receiver, when radiated by a 5kW Xenon arc lamp, increased by up to 83K resulting in a thermal efficiency of 55% for the proposed solar receiver. Here the air flow rate was set to 0.0055kg/s at an inlet temperature of 295K with no particles or fan forced circulation. When particles were added to the receiver, a 0.034% volume fraction, and the installed fan induced forced recirculation in the receiver the air temperature at the outlet of the receiver increased by 123K and the thermal efficiency reached 89% for the same air flow rate as before. The results of normalized thermal and power generation efficiency indicate that the use of recirculating particles enhances the thermal efficiency by 49% and power generation efficiency by 90%, when compared with the air only cavity-type solar receiver. Moreover the proposed recirculating flow receiver exhibits a more uniform temperature distribution than a conventional cavity-type solar receiver due to better mixing of air and particles, along with more effective radiation and convection heat transfer between them.

A stand-alone feature of this solar receiver concept is that the air with particles is directly exposed to concentrated solar radiation monotonously through the recirculating flow inside the receiver and results in an efficient irradiation absorption and convective heat transfer to the air. The increase of thermal and power generation efficiency of more than 50% proved that the developed concept has the potential to enhance heat transfer from metallic particles to air through maximizing the heat carrying capacity by the particles and air from the receiver.

Declaration of originality

This work contains no material that has been accepted for the award of any other degree or diploma in any university or other tertiary institution and, to the best of my knowledge and belief, contains no material previously published or written by another person, except where due reference has been made in the text. I give consent to this copy of my thesis, when deposited in the University Library, being made available for loan and photocopying, subject to the provisions of the Copyright Act 1968. I also give permission for the digital version of my thesis to be made available on the web, via the University's digital research repository, the Library catalogue, the Australasian Digital Theses Program (ADTP) and also through web search engines, unless permission has been granted by the University to restrict access for a period of time.

Signed:

(Md. Rabiul Islam Sarker)

Acknowledgement

With great thanks I acknowledge the generosity of many people that supported this research project. I would like to start by thanking Dr Maziar Arjomandi and Professor Bassam Dally for their support, advice and guidance throughout my PhD program. Their generous sharing of academic and practical expertise assisted me at all stages of my PhD process. I would like to thank the academic and general staff of the School of Mechanical Engineering for their help and support during my post graduate studies. In particular, Dr Zhiwei Sun, Dr Yunpeng Xue and Mr. Dahe Gu for their suggestions and help during the experiments, Mr Garry Clark, Mr. Richard Pateman, Mr. Steven Smith and Mr. Pascal Symons for technical assistance with the experimental rig construction and Mr. Billy Constantine for his help with information technology support. I would like to also thank all the friends that I have made in the School of Mechanical Engineering for their advice, assistance, comic relief, creative diversions and friendship over the years.

Special acknowledgment goes to Mr. Marc Simpson who spent considerable time assisting me with the solar simulator apparatus at the Mechanical Engineering Thebarton Research Laboratory, his technical support, interesting conversations and advice will always be remembered.

This work was financially supported by Commonwealth funding's from the Australian government and Commonwealth Science and Industrial research Organization (CSIRO). Special thanks go to Dr Sarah Millar who was the advisor from CSIRO under the Energy flagship scholarship. I would like to thank the Australian Government and CSIRO for their valuable financial support during this project.

Most importantly, I extend a million thanks to my family members, including my two children Ayesha and Joty, and especially to my wife Saeeda Akther, and father in law Mirza Md Naofel Uddin and mother in law Siddika Begum. I could not have completed this work without your wonderful love and support during the course of this project. A special

thanks to my elder brothers for their love and affection throughout my study. This thesis is dedicated to my father Md Abdur Rahman Sarker and my mother Khodeza Begum who would have been very proud to see me complete this major milestone in my life.

Contents

List of Figures

List of Tables

Nomenclature

η	Efficiency
α	Absorption coefficient
$Q_{aperture}$	Power at aperture
ε	Emissivity
$A_{aperture}$	Aperture area
T	Temperature
Q	Solar power (Watt)
C	Concentration ratio
$r_{aperture}$	Aperture radius
r_{opt}	Optimum aperture radius
μ	Standard deviation
F_{peak}	Maximum flux density
I	Scattered light Intensity
l	Reference path length of medium
λ	Wavelength
x	Particle size
n	Index of refraction
θ	Scattered angle
c	Particle concentration
v_t	Terminal velocity
v_t^*	Dimensionless terminal velocity
μ_g	Viscosity of gas
ρ	Density
g	Acceleration
d_p	Particle diameter
D	Receiver diameter
τ	Response time
Nu	Nusselt number
Re	Reynolds number
Pr	Prandtl number

St	Stokes number
h	Heat transfer coefficient
A	Cavity surface area
I_G	Incident irradiation
k_f	Thermal conductivity of fluid
U_0	Free stream velocity of fluid
α_{sf}	The porosity of the porous medium
α_p	Particle volume fraction
V_{rms}	Root mean square air velocity
V	Total velocity of air
V_y	Axial component of air velocity
V_θ	Tangential velocity component
V_t	Volume of the whole receiver
M	Suspended particle concentration in air
N	Rotational speed of fan
CSP	Concentrated Solar Power
CST	Concentrated Solar Thermal
SPSR	Solid Particle Solar Receiver
HTM	Heat transfer medium
HTF	Heat transfer fluid
CPC	Compound Parabolic Collector
PLVCR	Pressurized Loaded Volumetric Ceramic Receiver
DIAPR	Directly Irradiated Annular Pressurize Receiver
NREL	National Renewable Energy Laboratory
SNL	Sandia National Laboratory
DLR	German Aerospace Centre
CIEMAT	Organisation of Plataforma Solar de Almeria
CSIRO	The Commonwealth Scientific and Industrial Research Organisation , Australia

Suffix

a	air
c	cavity
g	gas
m	mixture

p	particle
τ	thermal
o	overall
a,in	inlet air
a,o	outlet air

Chapter 1
Introduction

1.1 Introduction

The environmental impacts of the combustion of fossil fuels motivate research into clean alternative technologies. Burning of hydrocarbon fuel is the main cause of global warming and environmental pollution. Global warming is significantly altering the atmosphere by increasing the Earth's surface temperature and melting polar ice caps resulting in elevated sea levels. During the 20th century atmospheric temperature increased by 0.6±0.2°C and sea levels rose by 0.2m [1]. Increasing atmospheric temperature affects human physical and biological systems and also impacts on ecological systems [2]. In addition, non-renewable energy sources, such as fossil fuels, are gradually being exploited and it is postulated that fossil fuel sources will be depleted in 21st century. Hence, renewable energy sources, such as solar, are increasingly being developed and utilised as sustainable alternatives to fossil fuels.

In response to global warming and rising sea levels, developed countries set emissions targets for carbon based fuels under the United Nations Framework Convention on Climate Change (Kyoto protocol). In particular, Australia recently ratified the Kyoto protocol setting targets for greenhouse gas emissions. Australia has agreed to a target of 7% energy demand from renewable sources by 2030 and 25% by 2050 in order to offset greenhouse gas emissions [3]. Thus, to mitigate the environmental impacts of burning fossil fuels and meet Kyoto protocol

targets, it is necessary to search for renewable and sustainable technologies with market potential.

There are various clean energy sources available on the Earth's surface such as solar, wind and hydropower. In recent years, technologies based on renewable energy sources have become technically feasible and widely available due to the necessity of addressing global warming and associated environmental impacts. Figure 1.1 shows that renewable energy is one of the solutions for reducing environmental pollution. The technologies based on solar, wind or hydropower is free from CO_2 and other chemical pollutant which results in support to reduce CO_2 emission and global warming.

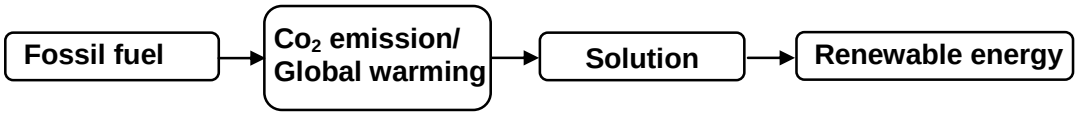

Figure 1.1 Concentrated Solar Power (CSP) offers an integrated solution to environmental pollution in the coming decades.

Of the range of renewable energy sources available for development, solar energy stands out as an underutilised and underdeveloped sustainable energy source. The amount of solar energy that reaches the Earth's surface in one hour is greater than the energy consumed by humans in one year [4]. The effective use of this huge amount of solar energy can potentially meet the demand for clean energy and assist to reduce environmental pollution.

Solar energy technology has great potential to satisfy power demand in Australia and in turn reduce reliance on carbon based fossil fuels. Figure 1.2 shows countries with peak solar energy recorded in the Sunbelt region, including the Middle East, USA and north-western Australia. Most countries, except those above latitude 45^0N or below 45^0S, are subject to an annual average irradiation flux in excess of 1.6 MW-h/m^2. Australia lies in a region of high annual average irradiation flux (Figure 1.2). In order for solar technologies to be considered a realistic alternative to fossil fuels, solar energy must be captured and stored in a cost effective fashion. Currently, solar energy is mostly used

as a primary source for process heating or electricity generation. Concentrated solar power (CSP) plant and photovoltaic (PV) cell plants are the most effective ways to produce electricity using solar energy. A techno-economic assessment of CSP and PV revealed that, for the same rated power and under the same environmental conditions, a CSP plant produces more energy than a PV plant [5]. Consequently, the economic return is higher for CSP and similarly, the required CSP plant area is comparatively smaller than the PV plant for the same rated power. As a result, CSP is a promising technology to produce electricity compared with existing solar energy technologies.

1.2 State of the art

Concentrated solar thermal power systems (CSP) are renewable sources of energy with the potential towards a sustainable energy future [6]. Australia, USA, Spain, Germany and Israel are the leading partners in CSP operated solar thermal systems as shown in Figure 1.3. In Kogan creek, Australia, a 44 MW solar thermal booster pant is under construction. In addition, CSIRO 1.2MW solar thermal plant is now in operation [7].

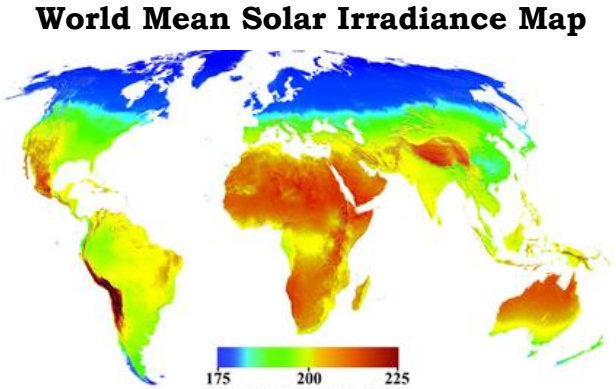

Figure 1.2 World solar energy map [8].

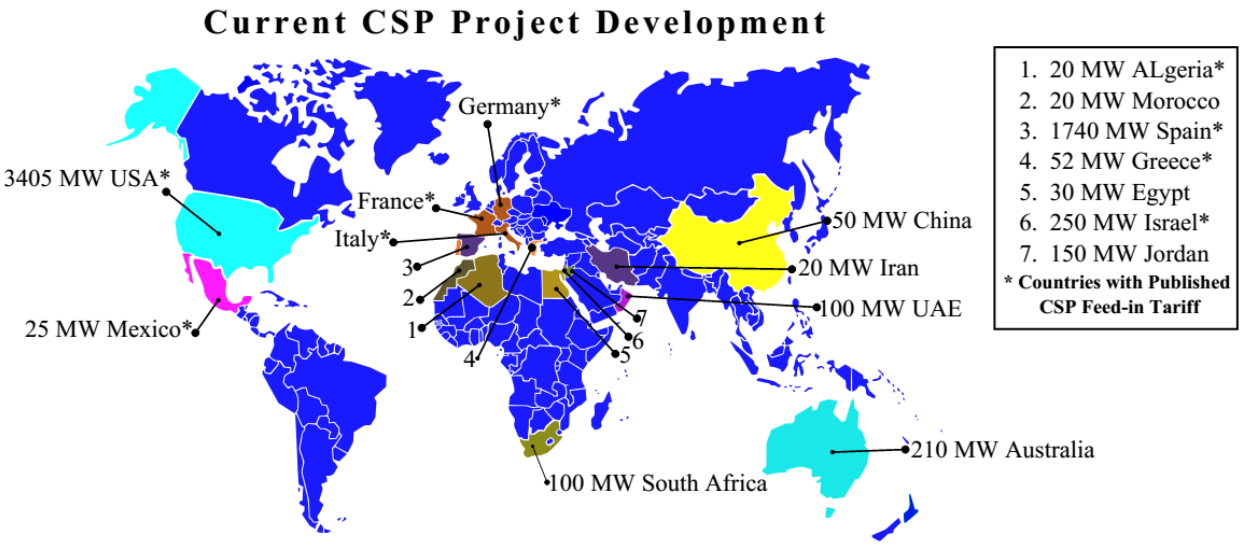

Figure 1.3 Current large scale CSP project goal [9, 10].

Based on current global power demand, present CSP based power systems are small when compared with other renewable technologies, such as wind, hydropower and photovoltaics. Different CSP technologies are available in the market, including parabolic dishes, power towers, Fresnel reflectors and cylindrical parabolic trough collectors. In each of these systems solar radiation is concentrated by mirrors or lenses onto a receiver where solar energy is converted to thermal energy. CSP systems are limited in their capability to produce high temperature fluids which depend on the concentration ratio of the system. Concentration ratio ranges from 10 to 100 for a parabolic trough and 100 to 1000 for dish and power tower systems. Accordingly, the temperature of a conventional receiver ranges from 400^{0}C in a low temperature trough to over 1000^{0}C in a dish and central receiver system [11]. Figures 1.4 and 1.5 show different types of CSP systems and temperature limits.

A Parabolic Trough or Linear Fresnel Reflector (Figure 1.5) is a type of solar thermal energy collector constructed as a long parabolic mirror, usually coated in silver or polished aluminium, with a metallic tube running along its length at the focal point. The mirror reflects sunlight to the metallic absorber tube, and subsequently steam or hot fluid is produced. The absorber of a trough system is capable of raising the temperature of the fluid to 400^{0}C-600^{0}C [12]. This type of system is

limited to being used for operating Rankin cycle or process heating. Currently, most projects utilising CSP are based on this system.

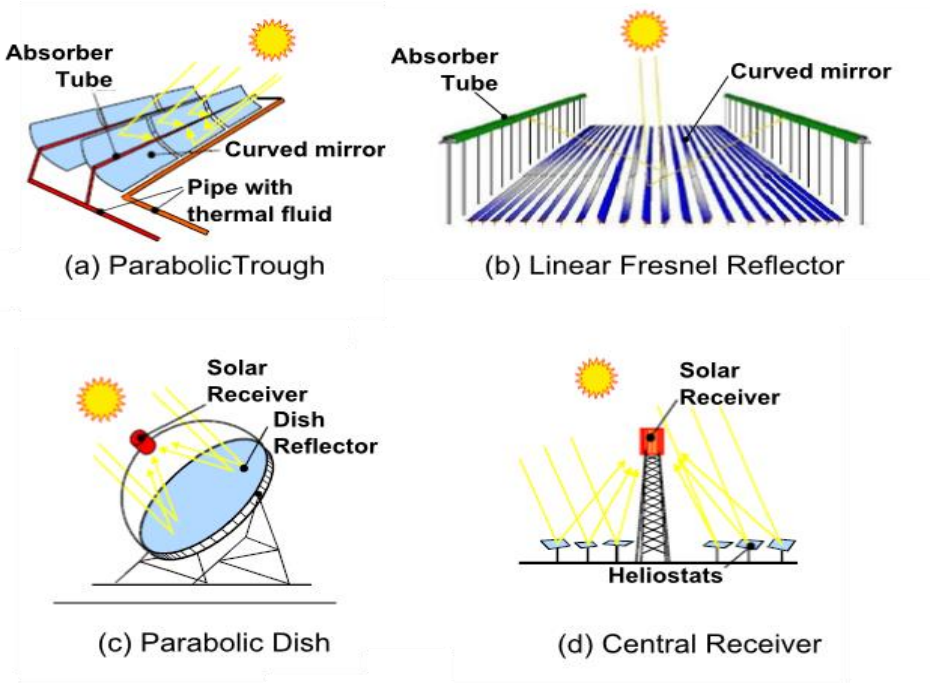

Figure 1.4 CSP systems including (a) Trough system (b) Fresnel system (c) Dish system and (d) Tower system [13].

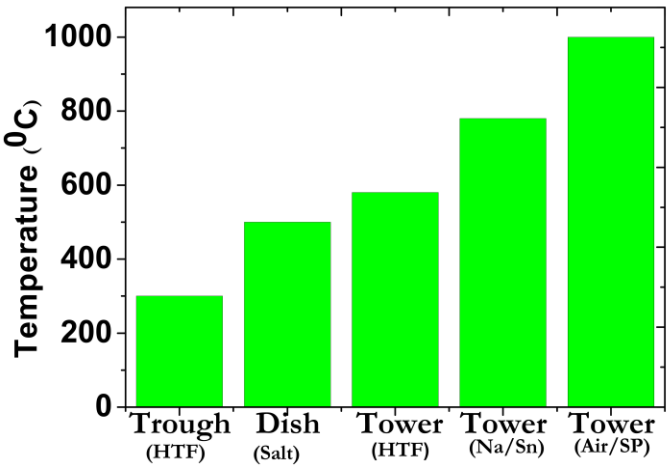

Figure 1.5 CSP based system operating temperature scenario [14].

A Dish Stirling (Figure 1.5) system uses a large reflective parabolic dish which is similar in shape to a satellite television dish. The dish reflector focuses sunlight onto a single point where a receiver captures the heat to produce steam or hot air. This system is capable of increasing the temperature of the fluid to 600^{0}C-1000^{0}C [12]. Typically, the dish is

coupled with a Stirling Engine in a Dish-Stirling System, but sometimes a steam engine is used. The Stirling Engine creates rotational kinetic energy using heat from the heat transfer fluid that can be converted to electricity using an electric generator. In recent years, small projects with a Dish Stirling System have been planned for operation in the USA, Spain and Australia.

The present study focuses on a central receiver system or central power tower receiver system. The schematic of this system is shown in Figure 1.6. In this system the sun's thermal energy is focused onto the solar receiver using thousands of tracking mirrors, called heliostats. The solar receiver, located on a tower, resides in the centre of the heliostat field and therefore is termed a central receiver system. The solar receiver transfers absorb heat into the heat transfer fluid (HTF) which is used to feed high temperature heat into a power conversion unit. Within the tower receiver, concentrated sunlight heats the heat transfer medium (molten salt or air) to over 1000^0C [12]. The heated medium then flows into a thermal storage tank where it is stored, maintaining 98% thermal efficiency, and eventually pumped to a steam or hot gas generator as shown in Figure 1.6. The steam, or hot gas, drives a standard turbine to generate electricity. A high concentration ratio of central receiver collectors improves the viability of the system for large scale production over other types of concentrating solar thermal technologies [15]. The central receiver system's potential can be enhanced by improving the thermal storage, back up and the receiver itself. Improvement of the solar receiver is the focus of this study, rather than thermal storage systems.

The current state of a CST (Concentrated Solar Thermal) receiver limits its operating temperature to about 1000^oC [16], which negatively affects the turbine efficiency. While thermal storage is an option for maintaining sufficient operating temperatures at the turbine inlet. A hybrid model concept of the CST receiver system (Figure 1.6), operating with a fossil fuel based co-firing mechanism, can maintain the operating temperature at peak load periods. Based on plant operating

temperature, 12-18% supplementary fossil fuel was used for continuous operation of solar plant [7].

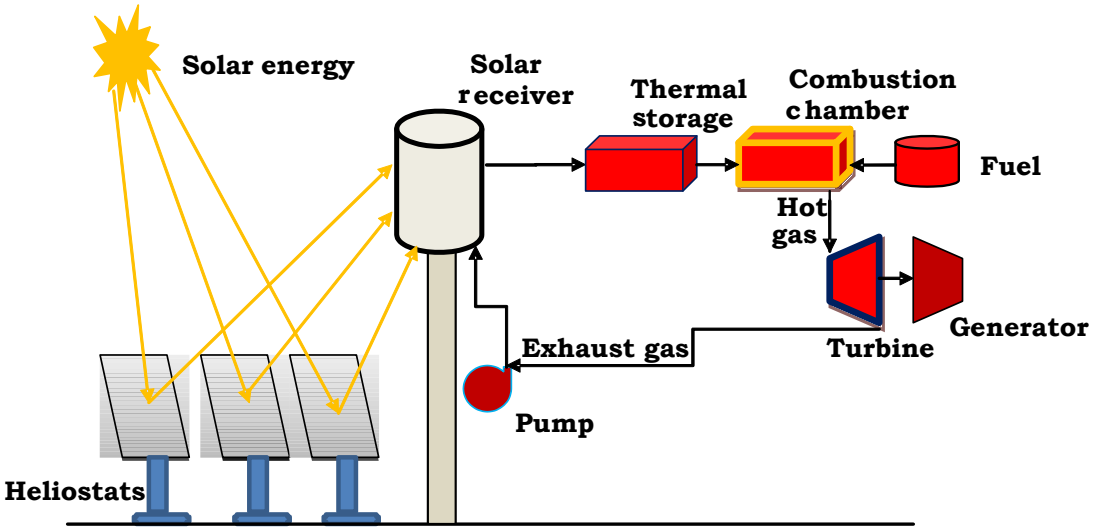

Figure 1.6 A hybrid solar power tower plant.

The main advantage of the central receiver system is its capability of absorbing 80-85% of the reflected energy and of transferring this energy to a heat carrying fluid. This study aims to improve the CSP plant by increasing the heat transfer efficiency of the central tower solar receiver. This will be achieved by enhancing radiation absorption and convection to the air through the use of recirculating metallic solid particles in the receiver.

1.3 Motivation

Most of the current CSP plants operate on the Rankine cycle. However; the Rankine cycle operated power plant efficiency is comparatively low. The Brayton cycle offer 40% more thermal efficiency than Rankine cycle at comparable power level [17]. The high temperature Brayton cycle operated solar thermal power plant (gas turbine plant) is a better option for achieving higher plant efficiency [18]. The absorbed solar energy is converted much efficiently by the gas turbine operated CSP plant. As a result, the required collector area is reduced significantly and thus reduced cost for solar electricity. Gas turbines, operated with central receiver based solar fields require a fundamentally different design from those for steam turbines. Gas turbines require very high

temperature air (>1000^{0}K), therefore a heat transfer medium is required to overcome the poor heat transfer characteristics of air (low density and thermal conductivity). However, air is readily available, easy to handle, nontoxic and non-corrosive. Consequently, air does not have restrictions on temperature in principle to keep the air in single phase at more than 1000K. Indeed, a different approach in designing the solar receiver and a different heat transfer medium (HTM), rather than air or steam alone, is required which can operate the high temperature Brayton cycle.

In the current research, the concept of internally recirculating metallic particles and air as a heat carrying medium in a cavity type volumetric solar receiver is proposed. The proposed receiver is expected to enable an efficient heat carrying capacity and supply high temperature air. The reported literature on particles in receivers has mostly focused on using solar energy for the chemical processing of reacting particles. However, the non-reacting particle was used in the freely falling particle concept to achieve high temperature solid particle rather than high temperature fluids such as hot air. Hence, this study investigates the potential application of internally recirculating non-reacting particles and air in a cavity type receiver. The special features of this receiver are:

(i) particles and the cavity inner wall absorb solar radiation directly;

(ii) an efficient forced convection heat transfer phenomenon between the air-particle mixtures provides efficient energy transfer to air.

Therefore, this type solar receiver has the potential to produce a high temperature working fluid suitable for use in a Brayton cycle.

The basic difference between the working principle of a conventional tubular type air or steam receiver and a cavity type solid particle receiver is that the use of solid particles in a cavity type receiver enables the absorption of more heat than when air alone is used in a tubular receiver (see Figure 1.7). The solid particle solar receiver concept uses concentrated solar flux reflected from a field of heliostats into a cavity type absorber where solid particles and the inner cavity

wall absorb concentrated solar irradiation directly. It has been demonstrated that the use of solid metallic particles as a working medium in a high temperature solar particle receiver/reactor provides efficient absorption of concentrated solar irradiation [3-8]. The present receiver is a volumetric and cavity type receiver, meaning that solar irradiated flux is absorbed by the whole volume and cavity inside surface. The volumetric absorption and cavity effect is advantageous because:

(i) it reduces temperature difference between the absorbing medium and working fluid which results in higher thermal efficiency;

(ii) it increases multiple internal reflections which results in more absorption of energy; and

(iii) it eliminates the receiver material limitation in exposure to high flux radiation.

The higher surface temperature of the absorber results in greater re-radiative loss in a tubular receiver. In addition, to avoid surface damage, the solar flux must be limited on most surface type absorbers, and even on many volumetric absorbers. Excessive solar flux on those receivers can lead to hot spots which may result in thermal cracks or failure. In a particle receiver, particles as an absorbing medium eliminate deficiencies such as excessive solar flux and high temperature re-radiative losses.

A solar receiver or reactor operating with particle clouds requires supplementary excess air to convey and maintain a desired particle concentration in the air [19, 20]. This excess gas requires more supplementary solar process heat, which results in unacceptably low solar receiver efficiency [21, 22]. In the proposed solar receiver, the flow of particles and air is controlled by a standalone designed system that helps to avoid the need for a supplementary gas supply. The forced recirculation characteristics of this concept are expected to increase the gas residence time. Consequently, an increase in the outlet temperature of the air is expected, when compared with the

conventional external type receiver concept. As a result, higher thermal efficiency and high temperature gas is expected from this novel system. Additionally, the particles serve as the storage medium, eliminating the need for additional piping and heat exchanger equipment. In a solid particle receiver, particles itself act as a heat carrying and storage medium and can exchange heat to the heat transfer fluid without any intermediate medium or device. High temperature power cycles and thermochemical processes require particularly high temperatures fluid. Therefore, the developed concept makes a contribution to the operation of this type of power cycle with the high temperature of the working fluid.

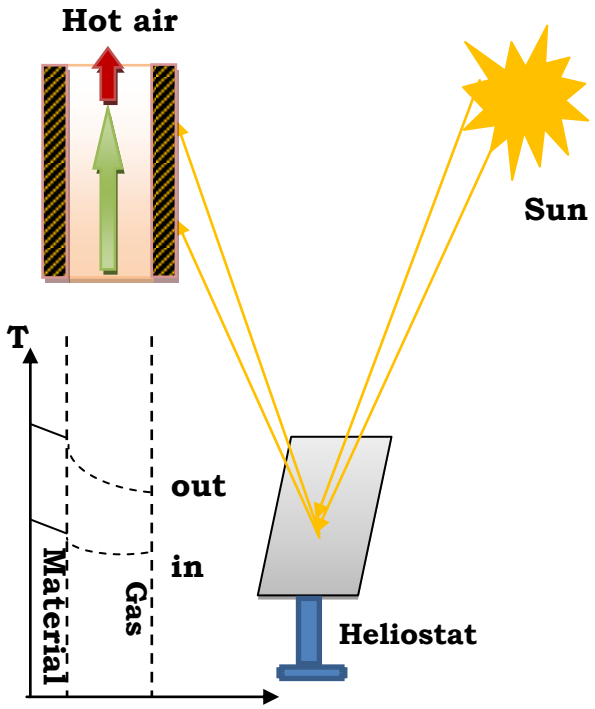

Figure 1.7a External type solid particle solar receivers [11].

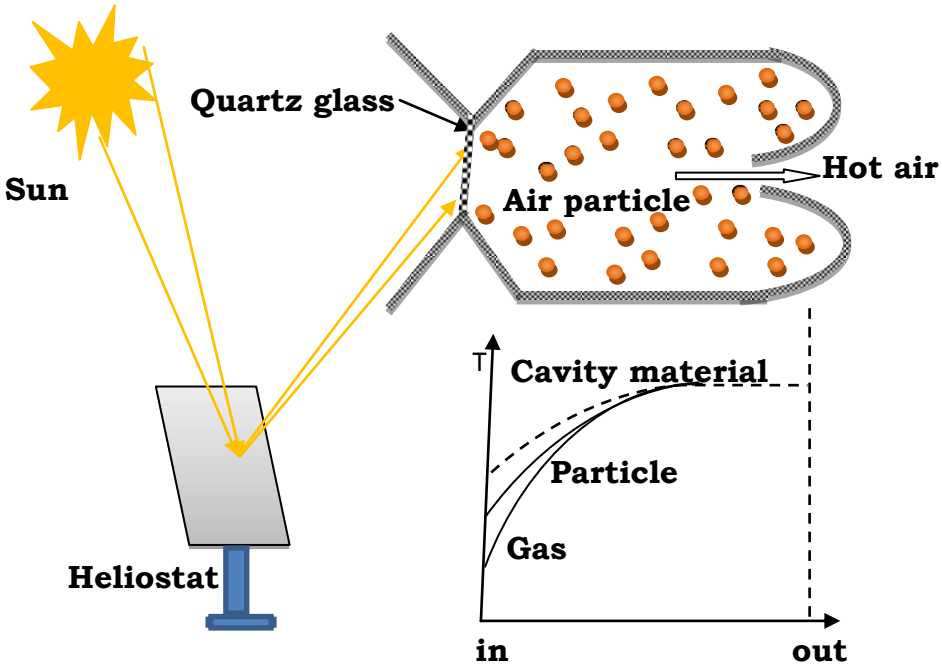

Figure 1.7b Cavity type (right) solid particle solar receivers [11].

1.4 Project goal and scope

Solid particle solar receivers for solar power towers have recently been under intense investigation, specifically Brayton cycle systems where high temperature gas is supplied from different types of volumetric or tubular receivers [6]. The present study focuses on a new cavity type solar receiver consisting of an insulated vessel, closed by a quartz glass window, and forced recirculation of metallic solid particles with air. Research on the application of particles for heat transfer enhancement [23-25] is mainly concerned with temperature increases of solid particles for further processing, rather than air temperature, and most testing has been conducted using freely falling particle receivers. Moreover, previous studies involved particles in a vortex flow type cavity reactor for solar gasification; i.e. there was no investigation of using non-reacting particles and air for heat transfer enhancement purposes in a cavity type directly irradiated solar receiver. Hence, this study investigated the effects of using an internally recirculating metallic particles and air mixture on thermal behaviours of a cavity type solar receiver.

The present study investigates the fluid dynamics behaviour of the air and the particles, the radiation absorption of the particles, thermal exchange between the particles and air, and the receiver wall temperature distribution in a cavity type solid particle solar receiver. These are all fundamental aspects for the evaluation of the working temperature of the system. In particular, the present investigation explored the effect of fan RPM on the fluid flow field. In addition, particle concentration variation will be addressed during this investigation, at different rotational speeds of the fan. Flow behaviours are investigated to determine sensitivity of any variables, such as the normalized terminal velocity, Stokes number, turbulent intensity and so forth. This investigation also will identify the optimum rotational speed to obtain a condition whereby no particles are deposited on the aperture window.

This study also investigates the effect of adding metallic particles to the recirculating air flow on the thermal performance of this standalone receiver. To maximize solar energy absorption, this study provides an estimation of the optimum particle volume fraction and rotational speed of the fan. Specifically, this investigation characterizes the effect of the recirculation of air with particles on the thermal performance of a cavity type solar receiver. The particle concentration at variable recirculation rates of air and the effect on the receiver's thermal performance are also investigated.

1.5 Thesis outline

Previous work in the area of concentrated solar tower receivers and associated contributions to the field are discussed in Chapter 2. Moreover, the research gap and aims of this project are presented in that chapter.

Chapter 3 presents the concept of recirculating solid particle solar receivers, including a preliminary comparative analysis of a cavity type receiver with different HTM and thermal efficiencies.

Chapter 4 focuses on the design and construction of the experimental facility. Design of the recirculating flow cavity type receiver, instrumentation and parameters of the solar simulator are described in detail in this chapter. Investigative methods of fluid and particle behaviour and thermal performance are also discussed herein.

The experimental analysis of flow behaviour in the receiver is discussed in Chapter 5. In particular, air flow patterns in the cavity and measurements of particle concentration at different forced recirculation rates are analysed in this chapter.

Thermal performance parameters, such as the exit air temperature, thermal efficiency and power generation efficiency of the receiver, are analysed in detail in Chapter 6, using the experimental results. The thermal performance parameter is analysed with respect to the mass flow rate of air, particle concentration, particle size variations and air recirculation rates, and particle free board heights. These analyses facilitate the development of the optimum performance parameters of the recirculating receiver.

In Chapter 7, a summary of the work and concluding remarks are presented and related to the study aims, along with recommendations for consideration in future studies.

Chapter 2
Background Literature

2.1 Introduction

Over the last three decades several experimental and numerical analyses have been conducted with the aim of improving the performance of the Concentrated Solar Tower (CST) system. In particular, research and development efforts have focused on CST technology in a number of countries, mainly Israel (Wiseman Institute), Australia (CSIRO), the United States (Sandia national laboratory, National Renewable Energy Laboratory), Europe (DLR, Germany and Platforma Solar de Almeria), China, India and the UAE [26, 27]. The knowledge gained from such research attention indicates that the CST receiver is the key component with the potential to enhance CST plant performance significantly. The solar receiver is the unit which absorbs concentrated sunlight and transmits the energy to a heat transfer medium.

External, or tubular type, and cavity, or volumetric type, solar receivers are used to produce high temperature gas for operating the Brayton cycle in a CST power plant [11]. As an early technological approach, bundles of steel tubes were used as tubular receivers (see Figure 2.1) and placed on top of a tower to absorb concentrated solar radiation from the heliostat field. During the early 1980s in Europe, tube solar receivers were developed for a 20MW air cooled central receiver project. However, during experimental trials the tubes of that receiver failed due to inadequate heat transfer and local overheating of the tubes [28]. Thus, in the 1990s a volumetric concept was developed using a wire

mesh solar receiver [29], as shown in Figure 2.2. The wire mesh receiver had a superior heat carrying capability as compared with the tubular receiver and achieved hot air of 800^0C to operate a 1MW steam cycle. Consequently, various improvements in tubular and volumetric receivers have been proposed and developed over the last three decades. While several approaches with different designs of the central receiver have been tested at laboratory scale and megawatt scale, an economically viable design has yet to be developed. Therefore, current improvements of tubular receivers, volumetric receivers and special cavity type solid particle solar receivers are important to review in this context.

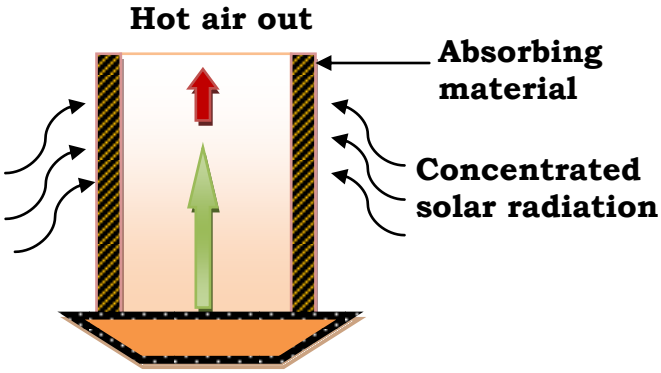

Figure 2.1 Tubular receiver [30].

2.2 Tubular receiver design

A tubular receiver generally consists of panels of many small (20-56mm diameter) vertical tubes welded side by side to resemble a cylinder. A typical tubular receiver is shown in Figure 2.1. In this receiver, the bottom and top of the vertical tubes are connected to tube headers that deliver the heat transfer fluid to the bottom of the subsequent tube. Thus, the fluid is recirculated from the bottom of each tube and then heated fluid is collected from the top of the tubes. Generally, tubular receivers are cylindrical in shape, with a length to diameter ratio limited to1.

The key challenges in designing a tubular type receiver are the large convective and radiative heat losses sustained at high operating

temperatures [31]. In a tubular type receiver, solar flux is directly absorbed by the exterior surface of the tubes. Thus, heat losses from a tubular receiver result from exposure of the outer surface to the atmosphere and an increase in the receiver surface area increases the heat loss. However, a reduction of the receiver surface area is limited by both the maximum operating temperature of the absorber, and the heat carrying capacity of the heat transfer fluid (HTF). The better the heat carrying capacity of the HTF, the lower the absorber temperature, so heat loss can be minimized [32]. Despite this, tubular receivers produce an outlet gas of below 800^0C and absorb a solar flux of less than 1000kW/m^2 [33].

In a tubular receiver, heat transferring from the outer irradiated surface to the gas flowing over the inner surface of the receiver is an indirect heat transfer process that makes the system inefficient. In addition, high temperature tubular receivers are subjected to rapid transient thermal loads that can adversely affect the life of the receiver [28, 34]. The energy transfer from the outer to the inner surface of the tubes is influenced by the geometry and thermal conductivity of the tube material. Lower thermal conductivity and large wall thickness lead to a high temperature at the outer surface, which in turn increases emission losses from the tube. At the inner surface of the tube, energy carried by the heat transport medium (fluid or gas) depends on the thermal properties and surface quality of the tube material.

In designing a tubular receiver, an important factor to consider is material constraints imposed due to high operating temperatures and the limitations of the concentration ratio [35]. These disadvantages are potentially less important when using a volumetric receiver. Hence, the tubular receiver is being replaced by volumetric type receivers with a more favourable heat transfer capability. Nonetheless, tubular type receivers are still under development and tested at the laboratory scale to operate the Brayton cycle [28].

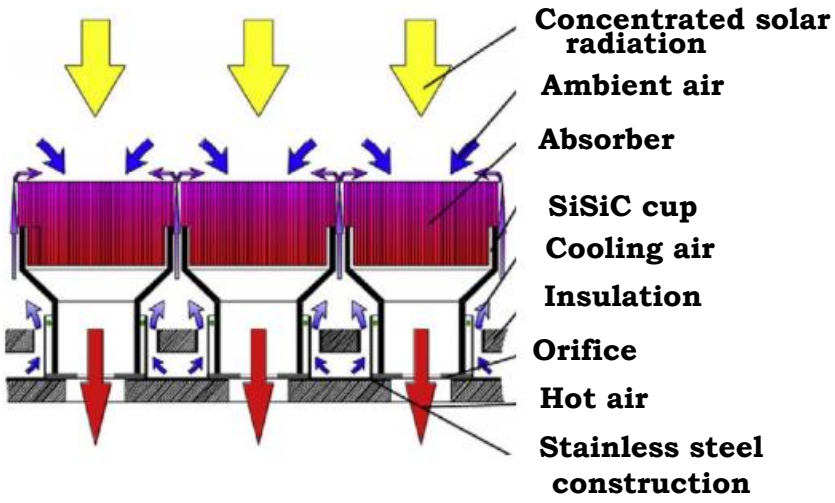

Figure 2.2 Open volumetric HiT receiver [11].

2.3 Volumetric receiver design

The volumetric type solar receiver was developed to overcome the heat loss problems of the tube receiver. A typical volumetric receiver is shown in Figures 2.2 and 2.3. In a volumetric receiver, radiation reflected from the heliostats passes through an aperture into a box-like structure or cavity before impinging on the heat transfer surface. The absorbing surface may be a stationary porous matrix or micron size moving metallic particles. The volumetric effect of the porous matrix type absorbing surface is used to absorb solar radiation and then transfer absorbed heat to the fluid flowing over the surface of the absorber that is directly irradiated. Consequently, reflected energy from the inside surface hits the backside of the front layer of the absorber and does not leave the receiver. Ultimately, it acts as a light trap. In addition, emission loss is minimized by allowing solar radiation into the deeper region of the porous structure [31].

Geometric configurations of the volumetric receiver are generally of two types: a matrix type porous metallic structure or a hollow cavity type configuration. Volumetric matrix structure receivers are generally built with a multitude of porous shapes of metal or wire meshes, foam or foil arrangements. Volumetric receivers made of metal ceramic or other

appropriate materials have a specific porosity and large surface area. Such materials are installed in the volume of a cavity so that concentrated solar radiation is absorbed in the depth of the porous structure through which a gaseous fluid is passed, as shown in Figures 2.4 and 2.5 [11]. The material requirements for this type of volumetric receiver are:

(i) resistance to high temperature,

(ii) high porosity to allow concentrated solar radiation to penetrate into the volume of the material,

(iii) high cell density to achieve the large surface area necessary to transfer heat from the material to the gaseous fluid flowing through the channels, and

(iv) high thermal conductivity [36].

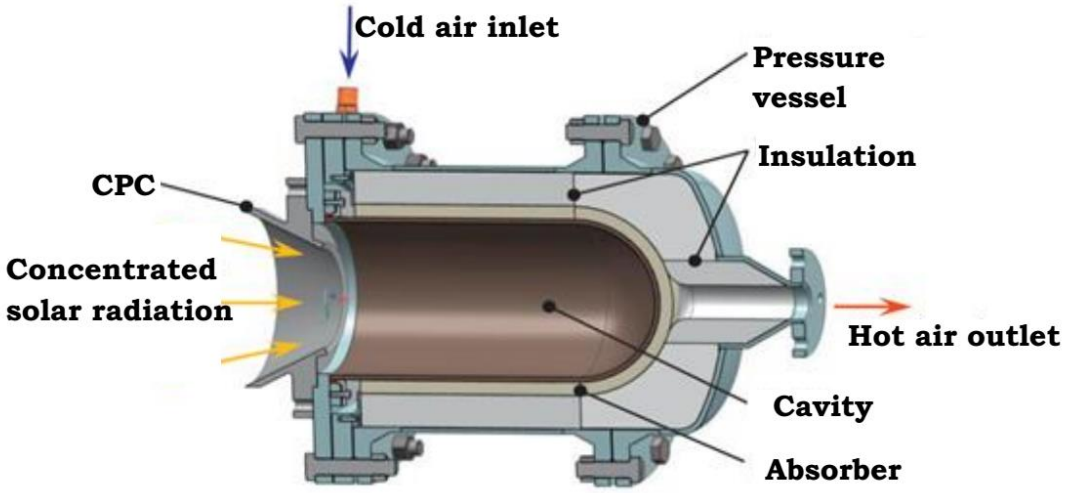

Figure 2.3 Cavity type volumetric receivers [37].

Figure 2.4 Ceramic foam as an irradiation absorbing material used in a volumetric receiver [38, 39].

Figure 2.5 Silicon carbide fibre mesh, metallic and silicon carbide ceramic carrier catalysts [38, 39].

Flow instability presents a problem for the porous structure absorber and reduces the absorber lifecycle. Pitz-Pall et al. [40] observed that air flow characteristics between high temperature and low temperature sides of porous structure volumetric receivers differed. Temperature difference was found to cause changes in air density and pressure between the two sides. Fluid flow instability was observed for honeycomb porous structures as a result of two sided pressure differences and different mass flow densities of the air. In contrast, for other types of absorbers, such as wire mesh ceramic foam, a stable flow was observed. The instability of the gas flow in a volumetric receiver can cause local overheating on the aperture, resulting in poor performance through melting or cracking [41]. However, improved porosity and large specific area of ceramic foam (SiC) improved cooling of the aperture surface, thereby, reducing the overheating problem and radiative losses. Further design improvements are required to establish this receiver at a commercial level but this is not a concern of this investigation.

In a cavity type volumetric receiver, the working fluid is heated by incoming radiation directly into the cavity volume. The absorber inside the cavity receiver, and in some cases the transparent window, reduces heat loss via convection and re-radiation to the outside environment. The geometrical configurations of the cavity itself help to reduce the convective and re-radiative losses and influence efficiency significantly. Concerning re-radiation losses, the cavity has distinct advantages over the external type volumetric receiver. The cavity type volumetric receiver with a transparent window helps to reduce reflection losses of impinging concentrated solar radiation and in some cases the loss is

negligible [35]. Receivers of this diverse group have been developed for both parabolic dish and solar tower receivers.

The advantages of the cavity type volumetric receiver are its compact design, ability to absorb relatively high solar fluxes, high operating temperatures and high pressure capabilities [42]. High pressure cavity receivers work with a glass window, whereas atmospheric pressure based volumetric receivers are windowless. Without a window, the application of volumetric receivers is limited. Thus, there are two types of volumetric receivers, namely open volumetric and closed volumetric receivers.

2.3.1 Open volumetric receivers

Receivers which operate under atmospheric pressure are known as open volumetric receivers. The working principle of open volumetric receivers is shown in Figure 2.2. The absorbing matrix of this type receiver is exposed to the ambient atmosphere without a glass window. In this type of receiver, a steel wire or porous material absorbs concentrated solar radiation inside the volume of the structure and transfers absorbed heat to a fluid passing through the structure. The assembly of multiple open volumetric receivers on top of a solar power tower is shown in Figure 2.2. In this system, hot air is produced and used for the production of superheated steam then powers a Rankine cycle. Atmospheric air is drawn by the absorber which is then heated by concentrated solar radiation at 600^0C to 800^0C.

Examples of laboratory scale operated open volumetric solar receivers include Sulzer1,2, TSA, SANDIA foam, and HiTREc I and II. A pre-commercial state solar thermal power tower plant with a high temperature air receiver has been built in Julich, Germany, as a complete system in MW scale, using this technology [16]. As relatively simple structures, good manageability of HTM air is the main advantage of the open volumetric type receiver. However, open volumetric solar receivers are not suitable to operate at high temperatures (above 1000^0C). In addition, its limited ability to sustain

high thermal stress at elevated temperatures is another limitation of the open volumetric receiver.

2.3.2 Closed volumetric receivers

A volumetric receiver operated under high pressure with a transparent window is usually treated as a closed volumetric receiver. The transparent window helps to separate the receiver cavity from the ambient air and enables a high pressure operation. The working principles of two different closed volumetric receivers are presented in Figure 2.3. Pressurized air enters through the inlet of a closed volumetric receiver rather than atmospheric air. The special features of this concept over an open volumetric receiver are the use of secondary concentrators to concentrate the solar incident radiation on the inner cavity surface and the shield surrounding the absorber structure. When pressurized air passes over the porous ceramic absorber, it is heated up by incoming concentrated solar radiation passing through the transparent window and leaves the receiver at the air outlet or exit. The hot gas is then used directly in the conventional gas turbine of a hybrid combined cycle system. The window system separates the HTF from the outside environment and reduces the heat loss associated with the outside atmosphere.

Much experimental and analytical study has been undertaken in order to improve receiver efficiency and the temperature of the working fluid by improving the cavity configuration and material structure [42-46]. Volumetric receivers that have achieved improved performance in a pilot scale plant include the Pressurized Loaded Volumetric Ceramic Receiver (PLVCR), Directly Irradiated Annular Pressurized Receiver (DIAPRs), REFOS solar receivers, multistage volumetric receivers and two slab selective receivers. To reduce radiated heat losses, a new concept of the two slab selective volumetric receiver was proposed by B. Variot et al. [47]. In this receiver, the irradiated front slab was composed of transparent glass beads or silica honeycomb and the second slab was composed of ceramic fibre material surrounded by a solar transparent glass. The semitransparent first slab was designed to

enable solar radiation to penetrate through from the first to the second layer and reduce re-radiation loss. An outlet temperature of 1100K and 70% thermal efficiency was measured by this solar receiver. However, it was discovered that the thermal exchange capability between the air and the front wall of the two slab receiver material was poor, which imposed limitations on the temperature of the outlet air.

In 1989, DLR proposed a solar receiver named PLVCR [48] which featured a foam absorber installed into a volume closed by a front cover of quartz glass. Air was blown through the absorber and directly irradiated by solar radiation. The PLVCR was tested at Sandia solar furnace and it was concluded that the receiver was capable of delivering 960^0C outlet air temperature with an efficiency of 57% at 4.15 bar pressure [11]. The main disadvantages were reflection loss, cooling, inefficient sealing of the window and thermal stress on the window.

The Directly Irradiated Annular Pressurized Receiver (DIAPR, see Figure 2.6) was built by the Weismann Institute of Science (1990-1992). It was tested for an $11kW_{th}$ power input [43] and then for a 30-$50kW_{th}$ power input (1994-1996) at the same facility. This receiver was made of alumina silica with three parts, namely (i) a porcupine volumetric absorber (ii) a frustum-like high pressure window and (iii) a secondary concentrator. The window, used for separating the cavity of the receiver from the outer ambient air, allows for a high pressure (up to 20 bars) operation and minimization of reflection losses. The DIAPR had the capability to supply air that provides a temperature of up to 1200^0C and 71% thermal efficiency [41]. The developers suggest that improvement could be achieved through optimization of the porcupine structure and inlet and outlet passage to increase the average convective heat transfer rate.

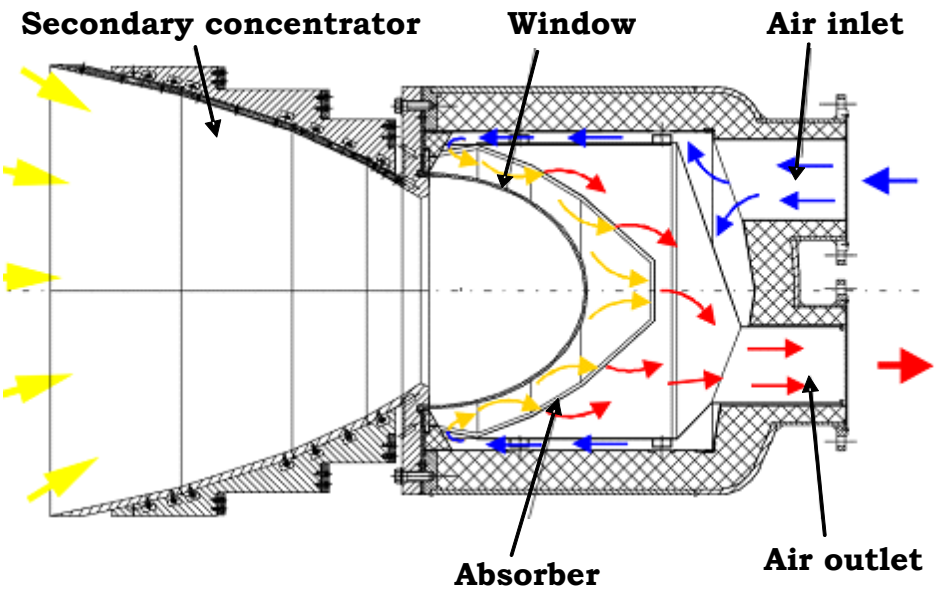

Figure 2.6 Direct absorption cavity type solar DIAPAR receiver [49].

A comparative study completed by Karni et al. [42] compared a porcupine absorber, a honeycomb structure absorber and an absorber with foam material in the DIAPR receiver. Porous monolithic multichannel silicon carbide (SiC, reSiC) of honeycomb shape was used in a honeycomb structure design receiver, which enhanced the heat transfer capability, providing high absorptivity and conductivity [50]. The porcupine absorber consisted of an array of pin fins, called porcupines, used to enhance the heat transfer rate to air. The beneficial features of this receiver include the good penetration capability of solar radiation and effective heat transfer capability, with strong 3D flow mixing. Furthermore, local overheating is prevented by allowing homogenous cooling of the front aperture [42].

The measured efficiency of the foam, honeycomb and porcupine structures were 0.58, 0.68, and 0.87, respectively, while the exit gas temperature were 547^{0}C, 561^{0}C, and 830^{0}C, respectively, for the same condition of solar flux [42]. The temperature of the front surface of the porcupine structure was significantly lower when compared with the foam and the honeycomb, especially near the centre. Moreover, while in the same solar radiation flux, the foam and the honeycomb surfaces melted and cracked, whereas the porcupine receivers exhibited

comparatively better heat transfer performance and a higher temperature of outlet air.

To minimize convection losses, a multistage DIAPR receiver [51] was designed as an improvement over the simple DIAPR. The special feature of this receiver is the connection of two receivers in series. One is a high temperature receiver stage (the simple DIAPR) and a low temperature stage is implemented as a partial ring of intermediate temperature producing cavity tubular receivers (pre-heaters), surrounding the central high temperature stage [43]. This multistage feature increases the irradiance level of the system and helps to heat the working fluid gradually when it passes through the different stages. The experimental investigation showed that the addition of the low temperature stage helped to limit the exit air temperature to 1000^0C, while the allowable operating limit was 1200^0C at 17-20 bars, with an incident solar flux of 3600-5300kW/m^2. The overall thermal efficiency of the receiver was 70-80%. In practice, the series of various cylindrical parts increased the pressure drop and heat losses in the connecting pipe of the receiver. Hence, optimization of the Multistage DIAPR receiver design is still essential to reduce these losses and pressure drops.

To achieve improved performance comparative with the DIAPR, the REFOS receiver [52] was built for the REFOS (1996) and SOLGATE projects (2001). The special feature of this receiver is a Compound Parabolic Collector (CPC) with a domed quartz glass window and volumetric wire mesh absorber. The CPC was used to increase solar flux and protect the receiver structure. The domed quartz glass was capable of withstanding a pressure of 19.5 bars and helped reduce reflective losses when compared with the flat shape glass window of the DIAPR. Experimental test results show that the REFOS receiver is capable of absorbing 350kW$_{th}$ of concentrated solar radiation at a solar flux of 1000kW/m^2 per module and attains an outlet air temperature of 800^0C at a pressure of 15 bars. Metallic wire mesh was used as an absorber for the medium temperature application, whereas the ceramic

foam absorber was used for high temperature applications in the REFOS project. In the SOLGATE project, a cooling air jet was passed over the window to stabilise the operation at high temperatures, achieved via an outlet air temperature of 960^0C.

A novel pressurized air receiver was proposed by Hischer et al. [53] in order to operate a combined cycle plant. This receiver consisted of an annular reticulate porous ceramic material bounded by two concentric cylinders. This concentric cylinder and porous absorber feature enhanced the convective heat transfer owing to the cross air flow system inside the receiver. Test results, with a solar concentration ratio of 3000sun, showed that the receiver attained an outlet air temperature of about 1000^0C at 10 bars pressure and 78% thermal efficiency. The maximum concentration ratio that could be used by this type of receiver is 3800sun. At a higher concentration ratio the receiver wall fails for thermal stress developed at the receiver surface [53].

Review of the volumetric absorber shows the main issues associated with the closed volumetric absorber are the transparent window thermal stress capability and limitations of the optical properties at high temperatures with sealing and cooling problems [11]. Thus, the outcome of this review of the volumetric receiver is that volumetric receivers remain under investigation for different cavities and different working fluids and few landmark discoveries have yet to be achieved. The radiation absorption and heat transfer capacity of air alone as a HTM is very poor. Hence, the use of air alone as a heat carrying medium into a cavity type solar receiver cannot provide an efficient solution to achieve high temperature air.

2.4 Solid particle solar receiver

An innovative concept of the cavity type solar receiver is the solid particle solar receiver (SPSR). This receiver type was proposed in order to overcome design deficiencies in other receiver types. As discussed earlier, flux limitations, high temperature stress and fatigue are issues in tubular and volumetric receivers of porous absorbers. The use of

metallic solid particles in a direct or indirect concentrating solar receiver resolves the flux limitation of those receivers. Metallic particles act as an absorber, or HTM, capable of withstanding high temperature. Hence, metallic particles in the receiver increase the solar absorption efficiency and consequently reduce losses associated with the porous absorber volumetric receiver and tubular air receiver. In a tubular receiver, the use of particles is not efficient as particles are heated by the walls as an intermediate medium and much of the solar energy is absorbed. The use of particles in a cavity type receiver removes the intermediate wall and concentrated solar irradiation is absorbed directly by the particles in order to heat the working fluid and act as a storage medium.

The main application of a solid particle solar receiver with a concentrated solar thermal (CST) system is the generation of high temperature fluids to operate high efficiency power cycles, chemical applications, or biomass processing. A schematic view of a solid particle solar receiver is shown in Figure 2.7 and Figure 2.8. The working principle of this concept is based on a curtain of falling particles (Figure 2.8) [24], or suspension of submicron particles (Figure 2.7) [54], into a cavity in which the particles are heated to a temperature in excess of 1000^0C. In this concept, heat exchangers are not required as an intermediate step within the receiver system.

A theoretical feasibility study of solid particles' suspension in a gaseous medium to exchange heat was initially conducted in the 1970s [54, 56]. In this conceptual receiver design, submicron carbon particles were suspended into air and heated by concentrated solar radiation in a pressurized cavity receiver (Figure 2.7). This feasibility study [54, 56] was performed to achieve high temperature CO_2 gas at 1100K for operating a Brayton cycle. In this concept, the receiver efficiency can reach up to 90%, depending on variable parameters such as particle concentration, size ambient temperature and optical properties, and the mass flow rate of the air.

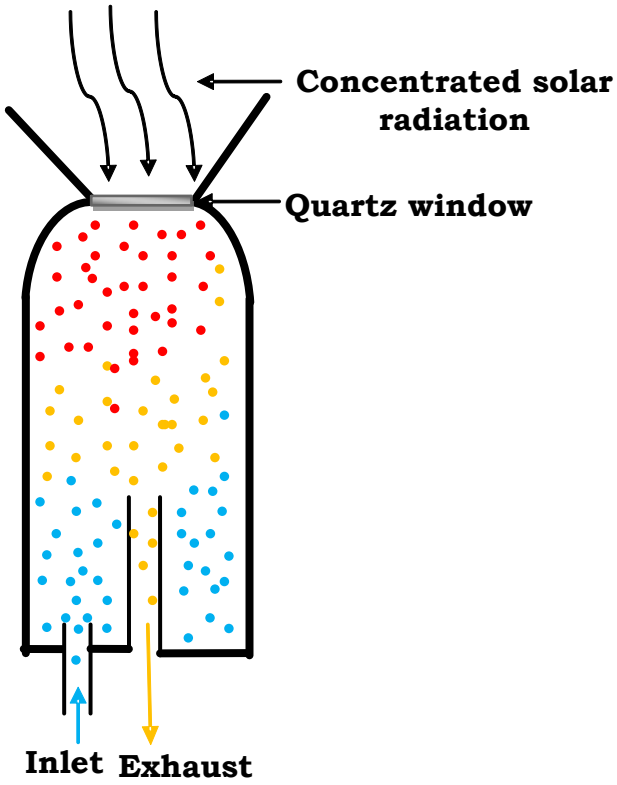

Figure 2.7 Conceptual design of small carbon particle solar receiver [55].

Challenges for this type of pressurized receiver include development of a suitable window capable of sustaining sufficient pressure and development of a solid gas suspension system that maintains a desired particle concentration and temperature in the receiver's cavity. Thus, it is necessary to develop such a system that can maintain both a uniform particle concentration and temperature field inside the receiver.

The application of metallic particles in a solar receiver was suggested in the early 1980s by Martin et al. [57] who proposed the concept of freely falling particles in an open cavity type solar receiver. Metallic particles were used in this concept to enhance the absorption of solar irradiation as an effective HTM and were targeted to achieve a particle temperature of above 1000^0C. The working principle of the freely falling particle solar receiver is shown as a schematic in Figure 2.8. Initially, a model of this concept was developed to predict the temperature and the efficiency of energy absorption as a function of particle size and mass flow rate [58]. The results of this model show that the temperature of

the particles at the exit cloud reaches 1100K with a power input of $75MW_{th}$ at the aperture, resulting in a thermal efficiency of 70% [59].

Results generated by the freely falling particle receiver trials were supported by Segal et al. who tested a prototype solid particle solar receiver at Sandia National Laboratories (SNL) [24, 60]. These authors reported that for the maximum given amount of power, $2.5MW_{th}$, the temperature of the particles was raised by 250^0C. They observed that particle temperature increased at higher power input or lower mass flow rate of particles. In analyses of the freely falling particle solar receivers, interactions between falling particles and atmospheric natural air flow were investigated on entry through the open cavity during operation. The freely falling receiver produces high temperature solid particles as a primary HTM, rather than a high temperature gas, while for power generation, fluid temperature is important to operate the Brayton cycle.

In practice, forced recirculation of fluid or particles is analogous to use a serpentine flow field in a conventional central receiver [61]. A vortex flow reactor (Figure 2.9) or internally recirculating flow reactor concept was applied to achieve a serpentine flow field. Metallic particles were used in a vortex flow and internally recirculating flow type direct absorption solar cavity receiver for gasification of biomass materials [62, 63] using coal/steam, coal/metal oxide, and natural gas/methane. These methods exposed the coal particles directly to solar flux, providing an efficient heat transfer directly to the reaction site where the energy was needed [20]. Most solar reactors [64-71] designed to date operate at temperature above 1000^0C to produce solar fuel, solar gasification, or process minerals and the like.

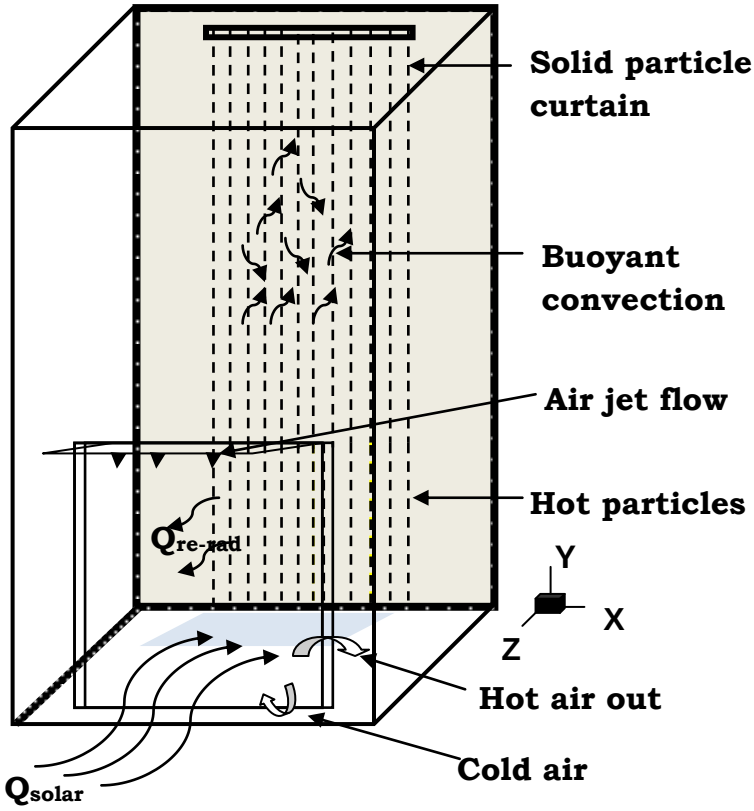

Figure 2.8 A conceptual design of a freely falling solid particle receiver [55].

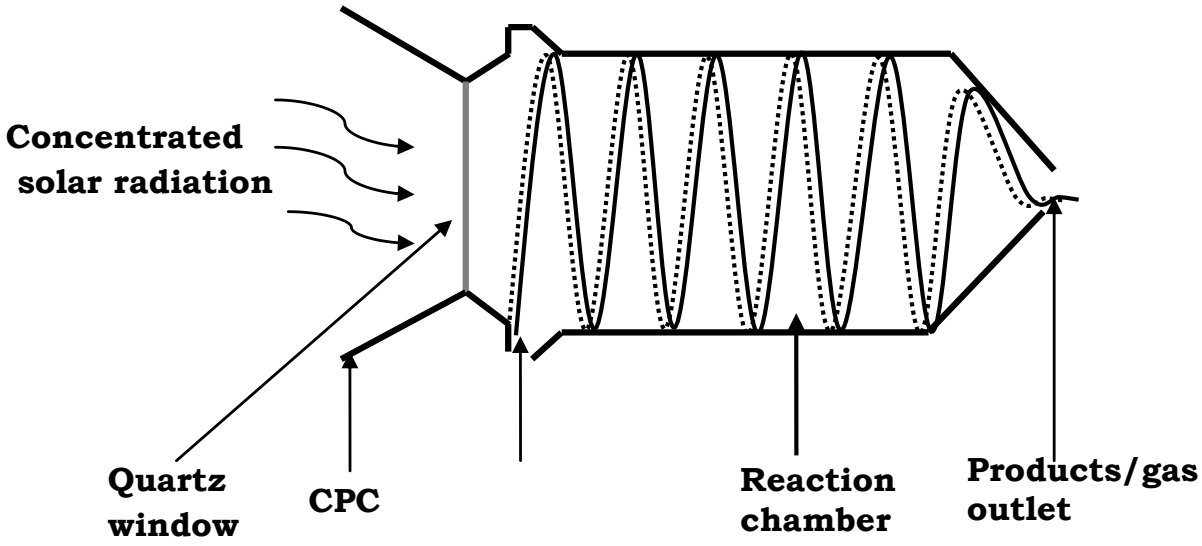

Figure 2.9 Schematic of a cavity type, direct absorption, vortex flow solar chemical reactor [20, 62].

Coke particles were gasified in an internally circulating fluidized bed reactor (Figure 2.10) operated as a direct absorption reactor, which

produced syngas by applying simulated visible light [63]. This concept is promising for solar gasification as it has advantages such as a higher residence time of reactants in the reactor and uniform temperature distribution throughout the cavity. Internal forced recirculation of reactant particles increases exposure time of solar radiation. With a 6kW Xenon lamp, a maximum 12% chemical storage efficiency was attained when the input beam was 0.9kW. This process requires sufficient external air supply to achieve recirculation of the reactant in order to reduce the system operating temperature.

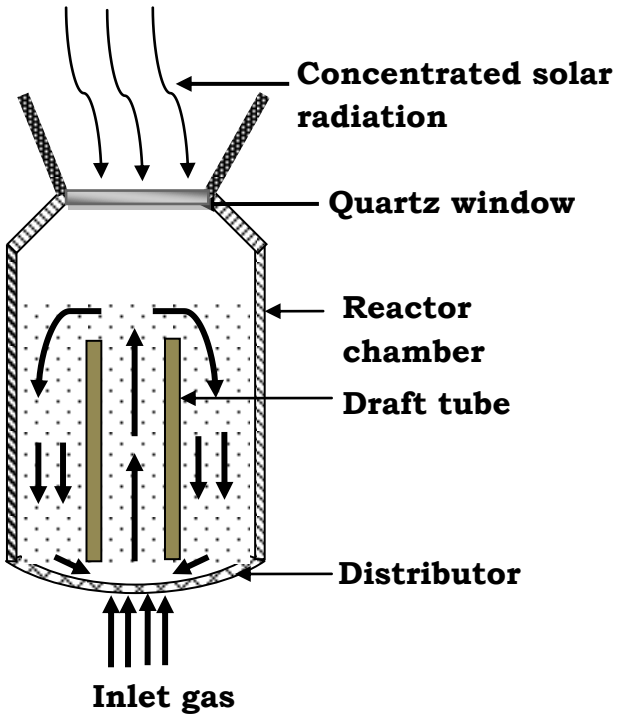

Figure 2.10 Conceptual design of an internally recirculating solar chemical reactor [55].

In the majority of reported studies, metallic or biomass particles were used in a cavity type volumetric receiver for biomass gasification, mineral processing, producing CO_2 or producing high temperature particles as a primary HTM. To achieve high temperature air as a direct HTM in a cavity type receiver, the potential of the application of air and internally recirculating non-reacting particles within the concentrated solar receiver was not considered. In order for the receiver or reactor to operate with particle clouds [19, 20] supplementary excess air is

required to convey and maintain a desired particle concentration in the air. This excess gas requires more supplementary solar process heat which results in an unacceptably low receiver efficiency of the solar receiver [21, 22]. It is therefore worthwhile studying the fluid flow and thermal characteristics of the proposed concept of recirculating particle flow solar receivers.

2.5 Heat transfer and heat transfer media

Two different heat transfer principles, namely direct and indirect heat transfer, are used in solar tower systems, as shown in Figure 2.11. In the direct heat transfer approach, energy captured from solar radiation is transferred by the receiver directly to the working fluid of the power cycle.

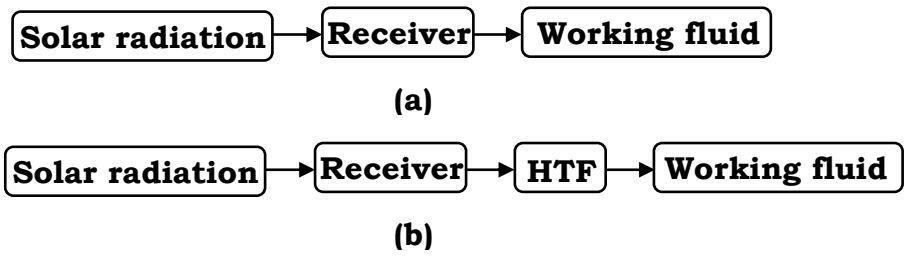

Figure 2.11 (a) Direct and (b) indirect heat transfer modes in a CSP receiver.

While an indirect heat transfer receiver system, energy captured from the concentrated solar radiation is transferred to the heat transfer media (HTM) and subsequently the hot HTM heats up the working fluid for the power cycle. Heat carrying fluids, such as air and water, are often used as direct heat transfer media in CSP based power plants, but helium, molten salt/liquid sodium and solid particles may also be used [72]. Generally, solid particles are used for combustion in biomass processing or mineral processing in a solar reactor. Solid particles, as a heat transfer medium, have been mostly used as a secondary medium to heat the working fluid of the power cycle using a heat exchanger as an additional system.

The effects of using a mixture of air and non-reacting-particles as a primary HTM in a cavity type receiver are not fully understood. It is

important to investigate the parametric sensitivity of non-reacting particles and air as a heat transfer medium in a recirculating flow and directly irradiated solid particle solar receiver. Therefore, in the proposed cavity type solar receiver, particle flow with air is controlled by forced recirculation of the air-particle mixture. The special features of this standalone receiver are:

(i) there is no requirement for supplementary gas to fluidize the particles;
(ii) the particles act directly as a solar radiation absorbing and heat transfer media; and
(iii) Controlled forced recirculation of the air-particle mixture is maintained.

2.6 Effect of particle concentration, particle size and recirculation rate

The thermal efficiency of a solid particle solar receiver depends on the particle flow rate and cavity temperature. An increase in particle flow rate reduces the cavity temperature and increases the cavity thermal efficiency [73, 74]. Thermal efficiency of up to 85% is possible when adjusting the optimum mass flow rate of the particles. Both the thermal efficiency and particle outlet temperature can be increased by reducing the particle diameter in a freely falling particle receiver [59]. Evans et al. [73] reported that convection losses increase with smaller particles as a result of the longer residence time and greater optical thickness in a freely falling particle receiver. Also, these authors found that an increase in the particle mass flow rate into a freely falling particle receiver increases curtain opacity [23]. Higher opacity reduces particle optical thickness and consequently reduces cavity temperature due to the lower penetration of incident irradiation. A curtain with higher transparency (at reduced opacity) allows the particles to receive relatively more direct flux and thus a comparatively higher temperature can be achieved [61]. However, a dense curtain of particles increases

absorption efficiency and consequently reduces re-radiation through the window.

Kim et al. [23] observed that smaller particles create a much darker cloud curtain for a constant mass flow rate of particles. Transparency of the particles' curtain depends on the particle size [23]. At a specific mass flow rate of particles, transparency of the smaller particles' curtain is lower, as compared with larger sized particles. However, the surface to volume ratio is higher for smaller particles when compared with the larger particles. In a numerical analysis using a north facing and face down solid particle solar receiver, Khalsa et al. [75] showed that absorption of incident and reflected concentrated solar radiation was reduced for the particle curtain with lower opacity. Subsequently, lower opacity increases the cavity wall temperature and increases the thermal emissions from the hot cavity walls, hence increasing the radiative loss from the walls. It has been suggested, that an effective use of particle forced recirculation patterns might allow an optimum curtain opacity to decrease the effect of the reduced outlet particle temperature [76].

Longer exposure time of solid particles in the solar flux enables increased solar energy absorption and hence enhances the convection and radiation heat transfer from particles to the air. The residence time of the particles [77] into a given solar incident irradiation and the use of forced recirculation of the heat transfer medium [75, 78] are two means for increasing the particle temperature in a cavity type receiver. Results from a sun test demonstration of a 2.5MW_{th} freely falling solar particle receiver suggested that particle forced recirculation can increase the particle temperature in excess of 900^0C, rather than 250^0C in a single pass curtain [61]. Hence, the forced recirculation characteristics of the current concept will increase both the particle residence time and gas in the solar irradiation. As a result, an improvement in thermal performance of the solar receiver is expected.

The exchange of heat energy from micron size particles to the surrounding gas in a gas-particle heat exchanging medium is an

important subject in many research areas, such as in a solid particle solar receiver or reactor and in a combustion system. Studies have shown that suspension of solid particles in a conventional fluid (water/air) has great potential to improve the heat transfer properties of that conventional fluid [79, 80]. This concept led to the development of the small particle heat exchange receiver (SPHER) at the Lawrence Barkley Laboratory, USA in which carbon particles were suspended to absorb radiant solar energy [54, 81]. W. Yuen et al [82] observed that the rate of heat transfer from particle to gas is strongly dependent on particle size and mass loading. In an experimental study, Klein et al. [83] showed that the average temperature difference between particle and gas increases from 2 to 27^0C when the particle radius is increased from 150nm to 500nm. However, the rate of heat transfer decreases as particle radius increases [82]. According to the Rayleigh absorption effect, the normalized heating rate of gas is independent of particle radius in the case of very small particles. Additionally, the particle recirculation rate and particle suspension density have been identified as the dominant factors influencing heat transfer between the reactor/receiver wall and the particle and gas mixture in a circulating fluidized system [84]. Here, the recirculation rate of particles is defined as the turnovers of the recirculating particles over a cross sectional area of a receiver/reactor. Where, the suspension density of particles is defined as the density of the particles suspended in a certain volume of a receiver's cavity.

2.7 Particle selection

To select appropriate particle material for a CST receiver with particles, the following three important characteristics must be considered [54]:

(i) high solar radiation absorption coefficient [55],
(ii) low propensity to reduce agglomeration, and
(iii) high resistance to fracture.

In addition, the particles must be inexpensive and readily available in the local market. Feasibility studies were performed to evaluate the appropriate particle material for freely falling SPSR in SNL by Falcone

et al., Hurby et al, and Rightley et al. [77, 85-87]. Silicon carbide, alumina, silicon and zircon, to name a few, have been widely used in freely falling particle receivers. For this present study, particle selection was based on optical characteristics, agglomeration and fracture strength. The studied particles, alumina, silica and zircon, are the preferred high temperature ceramic materials for improved behaviour over agglomeration. The compressive and fracture strength of the particles depend on their critical impact velocity [25]. Static heat treatment is required to examine the toughness of the material. Furthermore, cycling paced particle sample testing in a solar receiver provides the resultant effect of solar cycling on compressive strength. To satisfy the physical and economic characteristics of a SPSR, additional particles and high temperature ceramic material must be considered to provide a optimal particle selection in the development of SPSR. In a freely falling particle experimental analysis, alumina was used for its high density and better thermal properties. Micron size black SiC and alumina particles have been selected considering their favourable thermal and physical properties, as shown in Table 2.1.

Table 2.1 Properties of SiC and Al_2O_3

Properties	**Brown Al_2O_3**	**Black SiC**
Particle density	3600[kg/m^3]	3120[kg/m^3]
Thermal conductivity	18[W/m-K]	120[W/m-K]
Specific heat	880[J/kg-K]	750[J/kg-K]
Solar absorptance	0.73[-]	0.90 [-]
Solar emissivity	0.80[-]	0.90 [-]

2.8 Project aim and objectives

Continuous forced recirculation of particles and the effect of turbulent interaction of air with particles have not been investigated in the published literature regarding cavity type solid particle solar receiver. Hence, the present study aims to investigate the fluid dynamics and thermal performance of a cavity type solid particle receiver in which

solid particles continuously recirculate with a stream of forced flow air. In particular, the effects of different mass flow rate of air, different particle size, volume fraction and forced recirculation rate are examined. Note that in previous investigations of solid particle solar receivers, air was not used as a heat carrying medium with particles, and thus there is significant scope for further research to investigate the thermal performance of a solid particle solar receiver considering the above mentioned parameters. This work is of particular importance as air is readily available, non-toxic and non-corrosive and does not have temperature restrictions to remain single phase.

The specific objectives of this study, identified through a review of the published literature on the application of solid particles for heat transfer enhancement, are:

(i) To study the flow characteristics of air and recirculating particles behaviour in the proposed cavity type solid particle solar receiver;

(ii) To investigate the thermal performance of the proposed receiver and its sensitivity to particle volume fraction and mass flow rate of air;

(iii) To investigate the effect of particle size and type on the thermal performance of the receiver;

(iv) To investigate the effect of the recirculation rate of air and particle free board height on the thermal performance of the solar receiver.

Chapter 3

Problem statement and concept development

3.1 Introduction

This chapter discusses heat transfer models within a cavity receiver using air and a mixture of air and particles. Analysis focused on both natural and forced convection heat transfer, with only air as HTM, and the importance of using solid particles with air as the HTM in in a cavity type solar receiver. In order to analyse convection heat transfer to air in a cavity type receiver, a cylindrical shaped cavity was used, as shown in Figure 3.1. To simplify the analysis, a one dimensional heat transfer model was chosen. Air was considered as the HTF with an inlet temperature of 300K at an atmospheric pressure. The cavity was directly irradiated by a radiation source. The irradiance distribution was assumed to be uniform within the cavity. The radiative properties of the cavity were simplified such that it acted as a black body cavity. Hence, solar absorptivity and emissivity of the inner surface of the cavity was close to1.

To achieve uniform convection over the whole volume of the cavity, the surface temperature of the cavity was assumed to remain constant. The fluid properties were assumed to be constant over the temperature range. In addition, all properties of the fluid were considered to be independent of pressure, except the dynamic viscosity and density. Density was calculated considering the ideal gas law for changing the temperature and pressure. Consequently, the kinematic viscosity was altered according to the calculated density of the fluid.

Formulation of the steady state energy conservation for a cavity type solar receiver is given as:

$$Q_{solar} - Q_{sensible} - Q_{reradiation} - Q_{cond} - Q_{conv} = 0 \qquad (3.1)$$

Here Q_{solar} = Energy input from solar heliostat field;

$Q_{sensible}$ = Energy carried by the HTM;

$Q_{reradiation}$ = Loss of heat energy due to re-radiation;

Q_{cond} = Loss of heat energy due to conduction through the cavity surface;

Q_{conv} = Loss of heat energy due to convection to the outside environment.

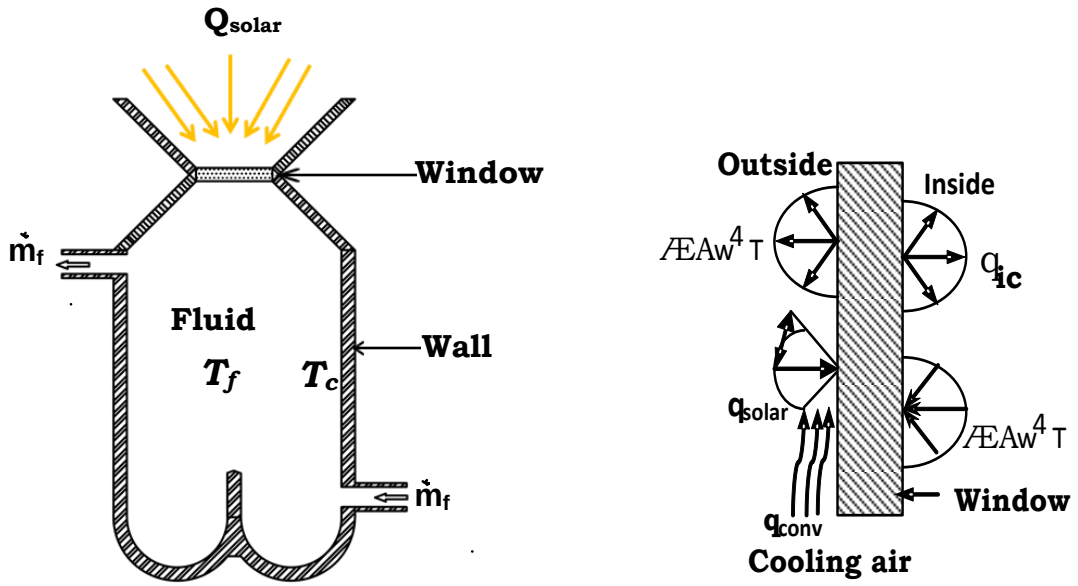

(a) Cavity receiver **(b) Glass window**

Figure 3.1 Schematic of the cavity receiver model with details of the different heat transfer modes.

Considering an air flow rate of $\dot{m}$, the energy carried by the HTF is calculated as follows:

$$Q_{sensible} = \dot{m} c_p \Delta T = \dot{m} c_p (T_{a,o} - T_a) \qquad (3.2)$$

Also, $Q_{sensible}$ is calculated by assuming a heat transfer coefficient due to convection as follows:

$$Q_{sensible} = hA\Delta T = hA(T_c - T_a) \qquad (3.3)$$

Where, T_c is the cavity temperature and T_a is the ambient temperature. Including the re-radiation conduction and convection losses, Equation (3.1) can be written as

$$Q_{solar} = Q_{sensible} - \sigma A_{aperture} \varepsilon T - A(T_c - T_\alpha)/R_{cond} - h_c A_p (T_c - T_\alpha) \quad (3.4)$$

Solving Equation (3.4) gives the value of $Q_{sensible}$ and T_c and consequently $T_{a,o}$ is obtained using Equation (3.2).
Hence, the thermal efficiency of the receiver accounting for the ratio of incident solar radiation to useful sensible heat in the pressurized air and particles is given by:

$$\eta_{thermal} = \frac{Q_{sensible}}{Q_{in}} = \frac{Q_{sensible}}{A_{aperture} I_G} \quad (3.5)$$

where $A_{aperture}$ is the area of the aperture and I_G is incident radiation passing through the quartz window.

3.2 Cavity receiver with air

In this analysis, the fluid temperature inside the cavity is investigated for natural and forced convection modes. For natural convection, it is assumed that the inlet air is passed over the inner cavity surface at a very low velocity.

The internal convection heat transfer coefficient can be calculated as:

$$h_g = \frac{Nu_D D}{k_f} \quad (3.6)$$

The Nusselt number for natural convection on the vertical wall of the receiver is calculated by the following Equation [88]:

$$Nu_D = 0.67 (Ra_l)^{1/4} \quad (3.7)$$

Here Ra_l indicates the dimensionless Raleigh number associated with natural convection.

The Nusselt number for forced convection on the vertical wall of the receiver is calculated by the Equation (3.8) [89]:

$$Nu_D = 0.102 . \mathrm{Re}_D^{0.675} \, \mathrm{Pr}^{1/3} \quad (3.8)$$

Here, Re_D and Pr indicates the dimensionless Reynolds number and prandtl number associated with forced convection. The number Re_D is calculated based on the cavity diameter, D.

Solving the above Equations, convection heat transfer is calculated to obtain the heat carried by the HTF.

3.3 Cavity receiver with ceramic honeycomb /foam

As discussed in Chapter 2, a porous, absorbent material, such as ceramic foam and ceramic honeycomb, can increase the heat absorption and heat transfer capacity. In this analysis, a one dimensional model of a closed volumetric receiver composed of ceramic foam/honeycomb was considered. As previously outlined, the aim of this analysis was to determine the fluid temperature and receiver's surface temperature.

It was assumed that the cavity was partially filled with porous material. As the cavity was closed, loss due to reflection and re-radiation from the porous surface was assumed to be minimal. The outlet fluid temperature was calculated using the following heat balance Equation:

$$Q_{solar} + h_v V_t \frac{(T_{a,o} - T_a)}{\ln\left(\frac{T_c - T_a}{T_c - T_{a,o}}\right)} = 0 \qquad (3.9)$$

The volumetric heat transfer coefficient h_v was calculated as:

$$h_v = h_{sf} . \alpha_{sf} \qquad (3.10)$$

Here, the interfacial heat transfer coefficient, h_{sf}, was calculated by the following Equation [90]:

$$h_{sf} = \frac{k_f + (2 + 1.1\mathrm{Pr}^{1/3} . \mathrm{Re}_d^{0.6})}{d_p} \qquad (3.11)$$

The Reynolds number, $\mathrm{Re_d}$, was calculated using the following correlation,

$$\mathrm{Re}_d = \frac{\rho d_p U_o}{\mu_f} \qquad (3.12)$$

Here d_p is the particle diameter and U_0 is the fluid flow velocity into the receiver.

In this receiver, front faces of the foam structure irradiate first and then the irradiation penetrates as deeply as possible due to the porous nature of the foam. Neglecting heat conductivity and solar radiation absorption by the fluid, and applying the steady state condition, the energy balance gives the fluid temperature along with length of the absorber [90]:

$$\frac{T_c - T_{a,o}(x)}{T_c - T_a} = \exp\left(- \frac{A.x}{\dot{m}.c_p} \left[\frac{1}{x} \int_0^x h_v(x).dx \right] \right). \qquad (3.13)$$

Here x denotes the variable length of the absorber. Solving Equation (3.13) gives T_c for the whole length of the receiver. In addition, the solution of Equations (3.10), (3.11) and (3.12) gives the heat transfer coefficient due to convection between the porous structure and air.

3.4 Cavity receiver with air and particles

The addition of recirculating particles into the receiver changes the thermal properties of the working medium, which contributes to the improvement of the thermal performance of the proposed solar receiver. Metallic particle clouds were modeled assuming a non-gray absorbing, emitting and scattering medium exposed to solar radiation. Particles, assumed to be chemically inert, were subjected to thermal radiation. The thermal behavior of the solid particles in the receiver involves particle absorption of heat from solar radiation, and then exchange with other particles and cavity walls through conduction and radiation. Air in the cavity exchanges heat with particles and cavity walls through convection. The particles and cavity wall irradiate to other particles and to the sky through the quartz window.

To evaluate the impact of recirculating particles on heat absorption by air, four different volume fractions (0.10%, 0.20%, 0.30% and 0.40%) of metallic particles in air were considered. Using the effective mixture properties correlation and a code developed by Matlab, a semi-

analytical approach was undertaken to determine the heat transfer coefficient of the mixture. The volume fraction of particle suspension in air is determined as:

$$\alpha_p = \frac{V_s}{V_t} \tag{3.14}$$

Where, V_s denotes the volume of solid particles and V_t denotes the total volume of the air and particle mixture. Bauxite (Al_2O_3) was selected as the metallic particle for its favourable thermal and physical properties (as shown in Table 2.1), such as high solar irradiation absorption characteristics and thermal conductivity.

The forced convection correlation in a cavity (pipe) flow was used for Nusselt number calculation and the effective mixture properties follows the correlation described in [91-93]. The thermal conductivity and heat transfer coefficient of the mixture, as functions of the volume fraction of the metallic particles, were analysed using the correlation reported in [92, 94].

The heat transfer coefficient and Nusselt number calculation are calculated as follows:

$$h_p = \frac{Nu_{eff}\, D}{k_{eff}} \tag{3.15}$$

And using the modified Dittus and Bolter Equation provides

$$Nu_{eff} = 0.023 \mathrm{Re}_{eff}^{0.8}\, \mathrm{Pr}_{eff}^{0.33} \tag{3.16}$$

The analytical results show that an increase in volume fraction of the metallic particle leads to an increase in the convection heat transfer coefficient from particles to air (see Figure 3.2). Thus, an increase in particle volume fraction results in an increase in mixture density and higher thermal conductivity, which contributes to the improvement in thermal performance.

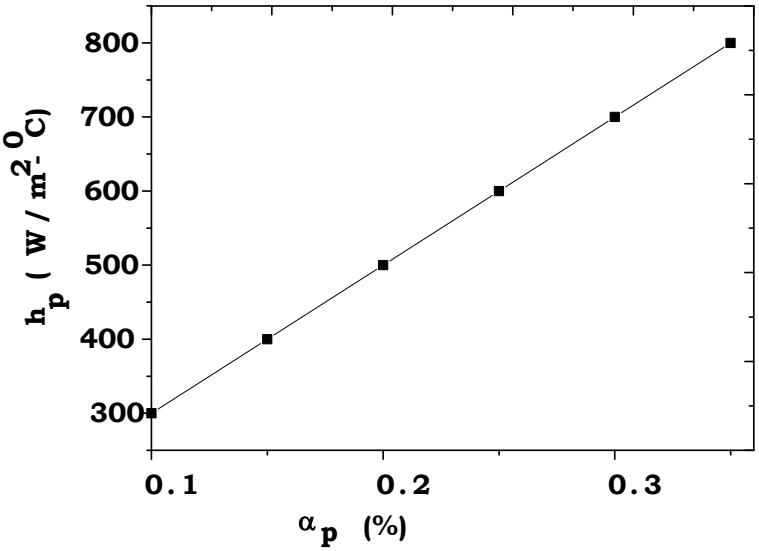

Figure 3.2 Effect of the particle volume fraction on convection heat transfer coefficients between the particles and air.

3.5 Synthesis of the models

Different types of solar receivers have associated advantages and disadvantages, as shown in Table 3.1. A tubular receiver receives an indirect heat transfer to the HTM, suffers from thermal losses and fails to carry the thermal stresses developed at high temperatures [28]. Volumetric receivers, with a porous foam and honeycomb structure absorber, have issues with the limitations of material temperature, high pressure drop and are susceptible to breakage in high temperature operations [11]. A cavity type volumetric receiver with recirculating particle is alternative option which can ensure about 90% thermal efficiency [28].

Table 3.1 Comparison between the different types of solar receivers [28].

Design	Advantages	Disadvantages
Tabular	Simple design	Thermal re-radiation loss and thermal stress
Volumetric Foam/honeycomb	Acceptable temperature and quadratic presure drop	Presure drop high and re-radiation losses more and suitable window
Cavity with particle	High temeprature fluid with low pressure drop	Suitable window, particle deposition and cooling problem

The directly irradiated cavity type receiver and air particle mixture as a HTM was identified as a feasible option to achieve the main objective of this project. The function of the air particle mixture is to absorb solar radiation volumetrically and reduce re-radiation losses. Moreover, the window and the wall of the receiver are at lower temperatures due to the cavity effect and overcome the limit of the operating conditions associated with thermal stress. Air mass flow rate is considered to influence thermal performance in the three cases of cavity receiver conditions, as discussed in Sections 3.2, 3.3 and 3.4. Figure 3.3 shows the exit temperature and efficiency of the receiver under these differing conditions. Results were obtained by solving Equations (3.2), (3.3) and (3.4).

In this analysis, it is assumed that the cavity is directly irradiated by a radiation source of 5kW. Figure 3.3 shows that the cavity type receiver exhibits a higher outlet temperature of air with a mixture of air and particles as an HTM in forced convection mode compared with the natural convection mode. A higher convection heat transfer coefficient from particles to air (see Figure 3.2) provides higher thermal efficiency and higher outlet temperature in the case of an air-particle mixture used as the HTM.

The transfer from the particles and walls to air was increased when the heat transfer coefficient of particle to air was increased. In addition, Figure 3.3 shows that forced circulation inside the receiver improves thermal efficiency and consequently reduces losses. As identified in Chapter 2, a reduced outlet temperature of air was observed when additional gas (air) is used to induce forced convection (mostly via fluidization) within the receiver. To better understand this issue, further analyses were conducted, as reported below, using a numerical model.

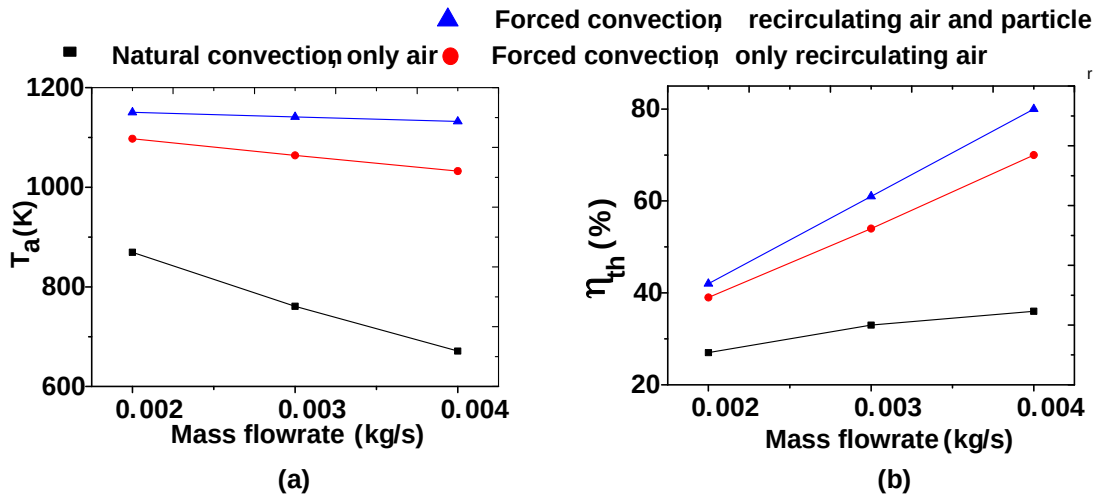

Figure 3.3 Variation of (a) outlet air temperature (b) thermal efficiency with the mass flow rate of air into a cavity type solar receiver

In order to understand the thermal field of a cavity type solar receiver, a 3-D computational fluid dynamics (CFD) model was developed. The cavity type solar receiver was constructed as a cylindrical shaped black body cavity receiver which receives concentrated solar power (5kW) through an aperture isolated by a transparent quartz window at the top. The quartz window ensures the isolation of the internal working medium from the ambient atmosphere. The emissivity of the internal cavity wall is assumed to be 1 to achieve the black body effect.

The commercial CFD package ANSYS Fluent 14.5 was used in this study. The basic geometry, with dimensions and adapted mesh, used in the model is shown in Figure 3.4. The dimension was selected assuming the receiver as a black body cavity. For a cylindrical cavity type receiver, apparent absorptivity is greater than 0.979 and surface absorptivity greater than 0.5, when ratio of the cavity diameter to aperture diameter is around 1.7 and ratio of the cavity depth to diameter is 2 [20]. Operating condition was selected, based on preliminary experimental receiver. Inlet air was at ambient temperature, pressure was atmospheric at inlet and outlet. Cavity was assumed insulating receiver.

The geometry was meshed using a uniform hexahedral mesh grid. The grid sensitivity study showed that 180,000 cells were sufficient to ensure grid independent results. The convergence criteria were set to

10^{-5} for all residual variables and the solution was converged after ~30,000 iterations.

In this analysis, the air and micron size Bauxite (Al_2O_3) metallic particles were used as the HTM for developing a two phase flow model. A uniform particle size of 500 micrometre diameter was assumed. Particle size was assumed based on comparative calculation of the terminal velocity and fluidization velocity of the particle and assumed superficial velocity to fly that size particles.

In this study, the flow field was modelled using a steady state RNG $k-\varepsilon$ turbulence model with the standard wall function and used viscous heating with a wall thermal effect. Due to coupling between the Energy and Momentum Equations, viscous heating plays an important role in the modelling of fluids which undergo strong temperature changes resulting in variation of fluid viscosity [95].

The calculated Reynolds number was above 12,000 based on the mass flow rate of air at the inlet and air flow was assumed to be turbulent in the receiver. Use of the standard wall function provides a commonly used approximation for the near wall velocity for turbulent flow. Compared with a standard $k-\varepsilon$ model, which uses a constant value for the Prandtl number, the RNG $k-\varepsilon$ turbulence model employs an analytical formula for the turbulent Prandtl number. This model also provides an analytically derived formula for the effective eddy viscosity that accounts for a low Reynolds number effect. Therefore, compared with a standard $k-\varepsilon$ model, the RNG $k-\varepsilon$ model is expected to provide superior performance for swirling flows, boundary layers separation and forced recirculation. The effect of buoyancy was also included in the model. The pressures at the inlet and outlet boundaries were assumed to be atmospheric. The turbulence kinetic energy and dissipation rate were calculated using the inlet flow condition. The ducted fan effect was modelled with a momentum disk situated at the bottom of the duct.

The mass flow rate was averaged over the fan rotor area. The tangential flow component was calculated by the tangential velocity at different

fan radius and set by a polynomial function, whereas the radial component was set to zero considering the axial flow fan. The tangential component was set as follows:

$$U_\theta = \sum_{n=1}^{N} f_n r^n ;\ -1 < N < 6 \qquad (3.17)$$

U_θ is the tangential velocity on the fan surface in m/s, f_n are the tangential velocity polynomial coefficients and r is the distance from the centre of the fan.

The pressure jump was set according to pressure developed by the velocity of flow and considered as a polynomial function. The polynomial function was set as follows:

$$\Delta p = \sum_{n=1}^{N} f_n v^{n-1} \qquad (3.18)$$

Where, Δp is the pressure jump, f_n are the pressure jump polynomial coefficients, and v is the local fluid velocity normal to the fan.

The particle (Al_2O_3) movement inside the receiver was governed by a time integrated force balance on each particle. The forces considered here were particle acceleration, drag and gravity. A discrete phase model (DPM) was used to track trajectories of the non-reacting Al_2O_3 particles in a Lagrangian frame. Stokes' Law was applied for calculation of the drag force. The gravity effect was added to the fluid flow Equation. The particle to particle interaction was assumed to be negligible which is valid for the volume of particles at approximately less than 10%. Dispersion of particles due to interaction with turbulent flow was forecasted using a stochastic tracking modelling technique. A step length factor of 10000 and time scale of 10 was used for modelling stochastic tracking scheme. A surface injection was set and 10 injections per tracking were enabled to track the particles path line. In Stochastic tracking model, the interaction of a particle with a succession of discrete stylized fluid phase turbulent eddies was simulated by the Discrete Random Walk Model. In addition, the fluctuating velocity component was simplified using the Gaussian probability distribution with enabling eddy life time equation.

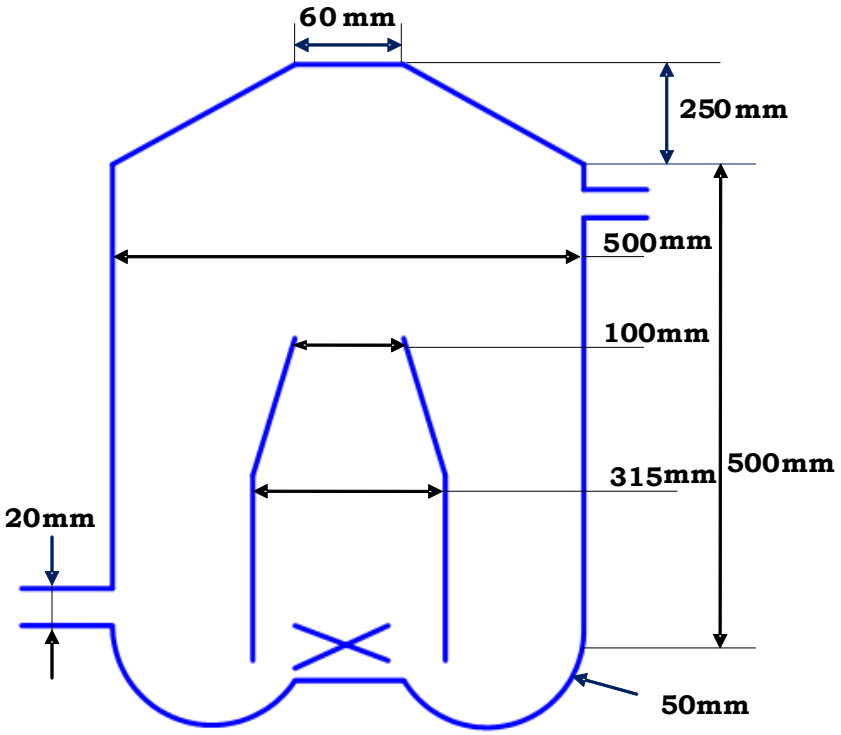

Figure 3.4 Schematic of a cavity type solar receiver model.

Particles were assumed to initiate movement by ducted-fan induced suction acting upon them from the lower part of the receiver and return to this area at every forced recirculation of the particles and air. It was assumed that no particles could escape from the outlet. Two-way turbulence coupling was used for the particles' discrete phase analysis. The initial temperature of particles was assumed to be equal to the ambient temperature. The convection and radiation model (Discrete Ordinate) was coupled with the air flow and particle model. The particles' scattering and absorption properties were chosen according to particle global properties, as shown in Table 2.1.

In the Discrete Ordinate (DO) radiation model used for calculating the radiation field inside the receiver, the Irradiative Heat Transfer Equation was solved for a finite element. The magnitude of the solar irradiation flux (W/m^2) was introduced to the cavity through the aperture and calculated using the estimated power input per unit area of the aperture. It was assumed that the wavelength of the solar beam was in the range of ($0\text{-}4.5\,\mu m$). A temperature dependent fluid density was assumed in this model considering ideal gas behaviour. This

temperature was used as an ambient blackbody boundary temperature to calculate re-radiation from the internal walls of the cavity to the aperture. The cavity inner wall was treated as a specular, reflective surface where particles and the cavity wall re-radiate energy which is partially reflected back to the cavity where part leaves the cavity through the quartz window. The temperature of the thermally insulated outer receiver boundary was assumed to be 300K.

To investigate the effect of the forced recirculation of solid particles as a heat transfer enhancement medium, three basic cases were studied and compared, namely:

(a) only air is utilized as the heat transfer medium without forced recirculation;

(b) only air is utilized as the heat transfer medium with forced recirculation;

(c) air and particles are employed as the heat transfer medium with forced recirculation.

The mass flow rate of injected air and all other working parameters were kept constant for the cases studied. The investigation was carried out considering the mass flow rate of air to be 0.00356kg/s, and the forced recirculation rate of air to be 0.22kg/s with a 10% particle by mass fraction.

Temperature contours within the solar receiver for different working conditions are presented in Figure 3.5. Figure 3.5.a presents the temperature distribution within the receiver without forced recirculation. In this configuration, a non-uniform fluid temperature distribution is observed, as the cavity wall absorbs solar radiation and then transfers the energy to the fluid via natural convection. A very high temperature region near the aperture was observed due to the lack of cooling effect of slow moving air at the aperture. Overheating of the aperture was resulted in radiation losses and very high thermal stresses on the glass window.

Forced recirculation resulted in more uniform temperature distribution inside the receiver due to the forced convection effect of air flow (see Figures 3.5.b and 3.5.c). The average outlet temperatures of the receiver under different configurations (a, b and c) are 580K, 620K and 830K, respectively. Thus, the solar receiver with recirculating air flow and metallic particles showed the greatest working performance. Hence, this finding was justified with further numerical analyses.

The mass flow rate of the injected air flow is an important factor in determining the thermal performance of the proposed solar receiver. In this section, the impact of the air flow rate on solar receiver performance is examined using different thermal performance parameters, including the average temperature of the exhausted air, thermal efficiency dimensionless efficiency. By varying the mass flow rate from 0.00356kg/sec to 0.00872kg/sec, the average exit temperature of the solar receiver with and without metallic particles is presented in Figure 3.6.

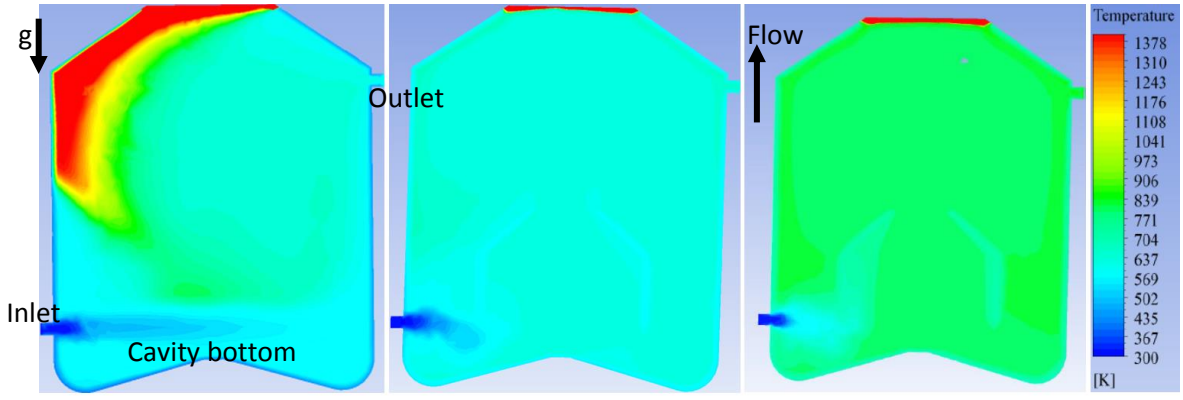

Figure 3.5 Cavity temperature distribution of a cavity type solar receiver (a) Natural convection with air (b) Forced convection with air (c) Forced convection with air and particle mixture.

As shown in Figure 3.6, the outlet air temperature reduces with an increase in the air flow rate and the effect of adding metallic particles is indicated by the higher outlet temperature of the receiver with constant heat flux and a definite amount of particles inside. It is anticipated that increasing the air flow rate increases the dilution of the air-particle mixture at a constant solar flux input and particle concentration.

Therefore, the specific heat capacity of the air-particle mixture increases which diminishes the outlet gas temperature.

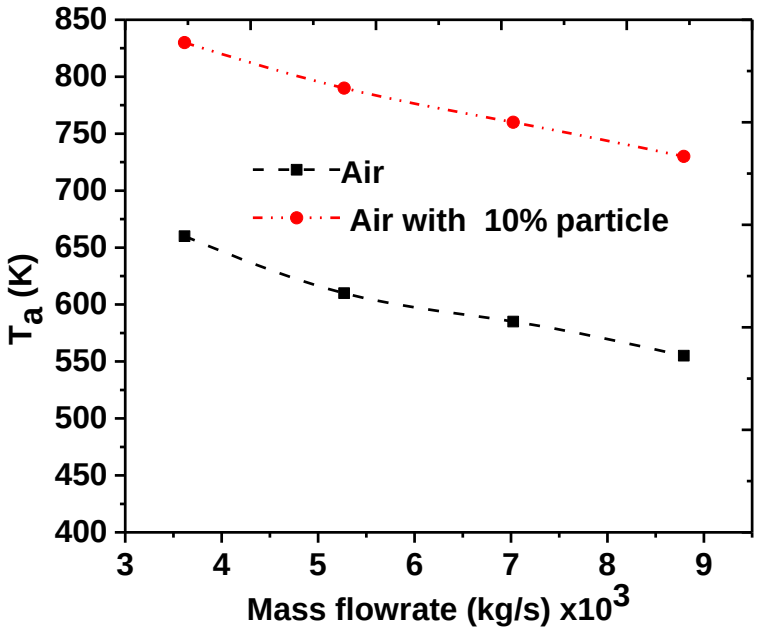

Figure 3.6 Variation of outlet air temperature with the mass flowrate of air in the solar receiver

The thermal efficiency of a solar receiver is another important parameter in evaluating its performance, which is defined as the ratio of the heat carried out by the working medium over the incident solar power. It is expressed as follows:

$$\eta_{receiver} = \frac{\dot{m}c_p(T_i - T_f)}{Q_{solar}}. \qquad (3.19)$$

Here, c_p is the specific heat of the heat transfer medium, T_i and T_f indicate the inlet and outlet temperature, $\dot{m}$ is the total mass flow rate of the working medium i.e air for this analysis and Q_{solar} is the input solar power through the quartz window aperture of the receiver. Figure 3.7 shows that the thermal efficiency increases with an increase in the mass flow rate of the working medium and the calculated thermal efficiency of the solar receiver with metallic particles inside is always greater than that without particles. The enhancement of thermal conductivity of the working medium by introducing the micron-size

metallic particles is one of the main reasons which leads to the efficiency improvement [96]. The recirculating flow pattern, which increases the residence time of the working medium, also contributes to higher thermal efficiency due to the greater irradiation absorption and more energy transfer from the particles to air. The uniform distribution of solar irradiation over the whole volume of the receiver, as a result of the converging and diverging geometric shape of the receiver, helps to increase the receiver thermal efficiency. The converging area concentrates the irradiation and then distributes the radiation inside the receiver through the divergent shape of the receiver. The outlet gas temperature was decreased and thermal efficiency was increased with the mass flow rate of heat transfer medium in the forced recirculation flow solar receiver as was seen in the experimental test of the freely falling solar particle receiver [24].

To understand the thermal performance improvement in the solar receiver caused by adding the metallic particles into the recirculating flow, the receiver dimensionless temperature and dimensionless thermal efficiency was determined for the variable mass flow rate of the injected air. Here, the dimensionless temperature, T^* is defined as the ratio of the outlet air temperature of the solar receiver having an air-particle mixture as its heat transfer medium over that having air alone as its heat transfer medium. Similarly, the dimensionless thermal efficiency, η^* is defined as the ratio between the thermal efficiency of the receiver with and without metallic particles in the cavity receiver.

It is noticed that the dimensionless temperature and thermal efficiency both increase (see Figure 3.8) with an increase in the mass flow rate of the injected air. This indicates that the impact of the introduced metallic particles into the recirculating flow on the performance improvement is more significant at a higher mass flow rate of the injected air. This is the effect of an increase in irradiation absorption surface when the particles are mixed with air as an enhancement in heat absorption and heat transfer medium.

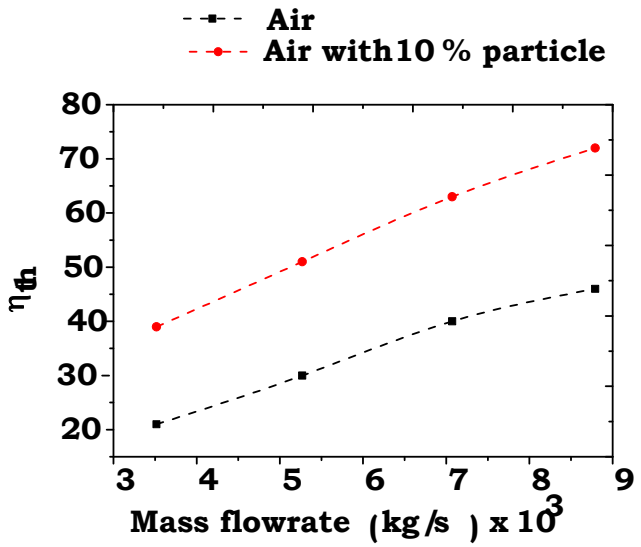

Figure 3.7 Variation of thermal efficiency using air only and air with particles into the recirculating flow solar receiver

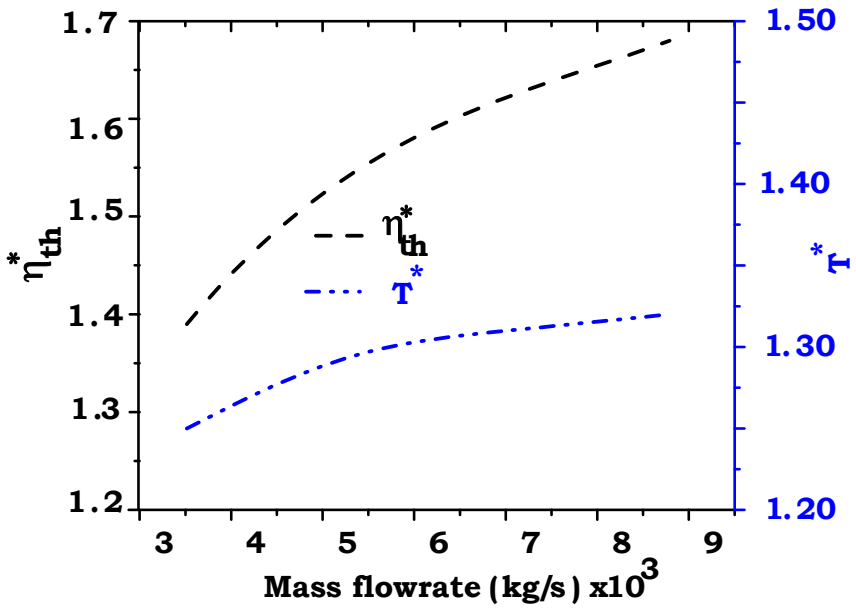

Figure 3.8 Dimensionless thermal efficiency and outlet air temperature as a function of mass flowrate of the injected air.

3.6 Recirculating flow solid particle solar receiver

The proposed solar receiver in this study has two key features, i.e., a recirculating flow field within the receiver and non-reacting metallic particles mixes with the flow. The configuration of the receiver is presented in Figure 3.6. The solar receiver consists of an externally insulated cylindrical cavity with a quartz window aperture at the top, a

duct fan combination system to generate the forced recirculation, an inlet for cold gas and an outlet for heated gas. In this solar receiver, metallic particles are initially stored at the bottom of the cylindrical cavity of the solar receiver and then recirculated by a specially designed duct fan combination system. Air is continuously injected into the receiver and recirculated several times before being exhausted from the outlet at a high temperature. Residence time of the air is dependent on the total flow rate.

In the proposed solar receiver, the air and metallic particles are internally recirculated by the duct fan system. Together with the air flow, the metallic particles move upwards from the bottom of the receiver towards the quartz window and then return to the bottom of the receiver as a result of the suction effect of the fan.

As shown in Figure 3.9, the upwards-moving metallic particles absorb solar irradiation directly which results in an increase in particle temperature. When the particles move back to the bottom of the receiver, absorbed solar energy is transferred to the surrounding air flow to form a high temperature mixture of air and particles. This high temperature two-phase mixture is then transported to the bottom of the receiver, where again energy is transferred from the mixture to the injected colder air and particles in the lower part of the receiver. By having such a mechanism within the receiver, irradiation loss is minimized and heat transfer performance is improved, which results in a higher temperature at the outlet.

For the case of the application of only air in the receiver, the solar flux is absorbed by the cavity wall. Convection heat transfer between the wall and the air causes an increase in temperature of injected cold air. Irradiation loss from the high temperature wall through the window limits the maximum temperature of the working fluid in such a solar receiver. When the solar flux is projected into the solar receiver with circulating air and particles, solar energy is absorbed by both the cavity wall and metallic particles. The recirculation characteristic of

this receiver enhances the convectional heat transfer performance within the receiver as results of forced flow induced by the fan.

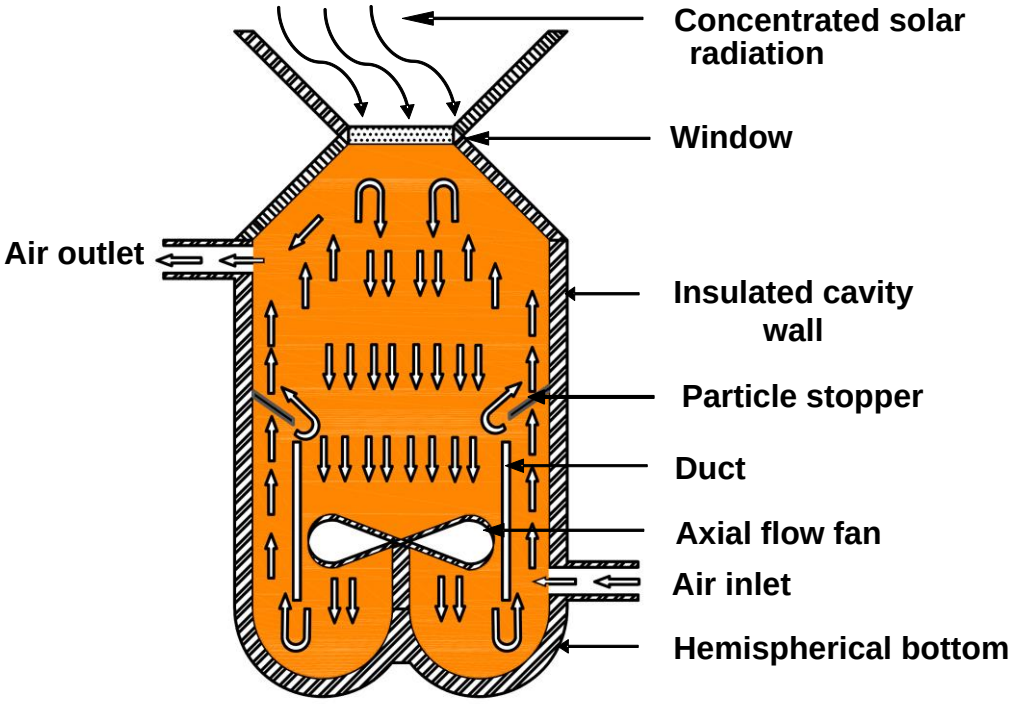

Figure 3.9 Recirculating flow solid particle solar receiver.

The addition of metallic particles can reduce irradiation loss through the quartz window by multiple reflections and absorption among the particles and the cavity. Radiation heat transfer among the particles and cavity wall, and forced convection heat transfer coefficient with the air, play a role in increasing the gas temperature in a turbulent flow thermal medium. An increased fluidization velocity increases the convection and radiation heat transfer coefficient among the particles, cavity wall and the gas and improves energy transfer in a recirculating flow type solar receiver [97]. In addition, the forced recirculation results in an effective mixing of hot and cold gases.

3.7 Summary

This chapter investigated three cases of different heat transfer phenomena and different HTM to develop a concept of cavity solar receiver with solid particles as the HTM for further investigation. Analyses show that the cavity type volumetric receiver with forced

convection exhibits greater thermal performance than the natural convection heat transfer case. Assuming forced convection and introducing a mixture of air and particles at the inlet provided higher outlet air temperature compared with the cavity receiver with only air as a HTM. Forced convection with the forced recirculation effect of air in the cavity receiver provided a uniform temperature distribution in the cavity. Therefore, the concept of continuously recirculating particles in a cavity type receiver was developed as such to provide higher temperatures of outlet air. In the following chapters, experimental analysis of the developed concept is discussed and the developed conceptual solid particle solar receiver is described.

Chapter 4

Experimental setup and Methodology

4.1 Introduction

Conceptual principles of the proposed solar receiver were described in the previous chapter. Design detail, material requirements and construction of the receiver are introduced here. This chapter also provides information on the equipment and methodology used for experimental measurements.

4.2 Experimental investigations

To develop a better understanding the concept described previously in Section 3.6, a recirculating flow solid particle solar receiver (SPSR) was designed and built. The prototype receiver was later used to conduct a series of experiments to investigate the characteristics of the air flow field, internal recirculating particles flow field and thermal behaviour of the receiver. The flow velocity inside the receiver was measured to determine the flow pattern and optimize the speed of the fan to suspend micron sized particles. Flow pattern was determined by measuring the flow velocity at different fan speeds and different axial and radial locations of the receiver. Different dimensionless parameters (described in the following chapter) used to describe the observed flow patterns. These dimensionless parameters were useful to select required fan speed for different size particles. The fan speed was quantified in such a way that forced recirculation of the particles was achieved without interaction with the quartz glass at the aperture. In

the event that particles were deposited on the glass at a particular fan speed, solar radiation was reflected or partially absorbed by the glass. This resulted in reduced thermal efficiency of the solar receiver. Hence, an understanding of the particle flow pattern at different revolutions per minute (RPM) of the fan was needed to ensure the window was free of particles and in order to enhance mixing of the air and particles.

A non-intrusive laser based technique was applied to measure the recirculating particle concentration. A relationship was developed between the particle concentration and fan speed to measure the particle concentration in the receiver. The thermal efficiency of the solar receiver was observed to change due to variations in particle concentrations at the free board region at different forced recirculation rates which then was used to find the optimum amount of particles in the free board region.

To understand the effect of recirculating particles inside the receiver, a thermal test was performed using three different case studies:

(i) a thermal performance test at different fan speed and at different mass flow rates of air;
(ii) a thermal performance test at different fan speed with a constant volume fraction of particles and different mass flow rates of air;
(iii) Both test cases were repeated where the free board height of the particles was altered.

These analyses were conducted to understand the effects of varying parameters on temperature of the heat carrying fluid and thermal efficiency of the receiver.

4.3 SPSR design

The main components of the SPSR receiver design are:

(i) a quartz window;
(ii) a receiver cavity with conical aperture part;
(iii) a ducted axial flow fan; and

The design of the receiver was based on the selection of appropriate material and receiver geometry and sizing, as discussed in the following sections.

4.3.1 Receiver material

Temperature limitations of materials present a challenge to solar receiver design. High temperature material is required to avoid melting and cracking problems at a high concentration ratio of solar heat flux.

The choice of absorber materials depends on the following factors:

(i) physical properties, such as the modulus of elasticity, melting point, thermal inertia and yield strength;

(ii) cost of materials;

(iii) ease of fabrication; and

(iv) corrosion resistance of the outer and inner surfaces to the surroundings and heat transfer fluid, respectively;

Based on the above criteria, it was concluded that the materials selected for the solar receiver must be able to resist extreme conditions, such as an oxidizing environment, high temperature, higher thermal cycle, thermal shock and so forth. Despite maintaining other mechanical properties, the materials should have higher absorptivity for solar irradiation, low emissivity and high thermal conductivity. A consideration in the selection of materials includes the type of solar receiver. Based on the receiver type, the material of the receiver body may be metal or ceramic. For a cavity type volumetric receiver, alloy steel or ceramic board is used, depending on the temperature limits of the designed receiver and may be coated with reflective paint to retain inner cavity absorptivity [20, 24].

Based on the modelling described in Section 3.5, a maximum temperature of 800^0C was expected in the presence of a 5kW radiation source. Thus, stainless steel (SS316) was selected for the current solar receiver whose properties are shown in Table 4.1. Stainless steel is capable of sustaining high thermal cyclic shock and carrying a thermal load of more than 1300^0C. This material is suitable for a heat

exchanger as it provides resistance to corrosion and increased strength at an elevated temperature. In addition, Stainless steel was capable to sustain the more than 1000^0C. Hence it was capable to resist the thermal creep. The stainless steel was not coated with paint, but with a sol gel coating to increase absorptivity.

Table 4.1 Properties of stainless steel (SS316).

Properties	Value
Density	8.00 kg/m^3
Thermal conductivity	16.3/m-K
Specific heat	500 J/kg-K
Thermal expansion	13.75 X10^{-6} m/K
Emissivity	0.9
Melting point	1673K
Modulus of elasticity	193GPa

4.3.2 Quartz window

The main purpose of the receiver window is to separate the receiver cavity from the atmospheric air and allow solar radiation into the cavity of the solar receiver. A good window must satisfy all design requirements over thousands of heating and cooling cycles and over a number of pressurization and depressurization cycles over a long period of time.

There are many glass materials available which can potentially be used for a solar receiver window, such as fused quartz, titanium based glass, borosilicate glass and so on. Fused quartz (fused silica) is a glassy material with excellent optical properties and thermal stability at high temperatures and is easy to fabricate in a desired shape. The mechanical and thermal properties of other materials are inferior when

compared with fused quartz for applications involving high temperatures and longer periodic functioning.

The material selection criteria and design requirements of the quartz window were described by Mande et al. [35]. Light transmission capability is one of the most important selection parameters in the design of a glass window. Figure 4.1 shows transmittance of different glass materials. High temperature quartz fused silica is generally used for the windows of solar furnaces or combustion furnaces. It is assumed that a 5kW xenon lamp may presumably produce a maximum 800^0C at the aperture window. Therefore, a 3mm thick and 85mm diameter quartz glass was selected for the aperture covering. The minimum commercially available glass thickness was 3mm. Thick glass refracts less light than comparatively thin glass. Considering its stress capability, the 3mm thick glass was chosen for this experiment.

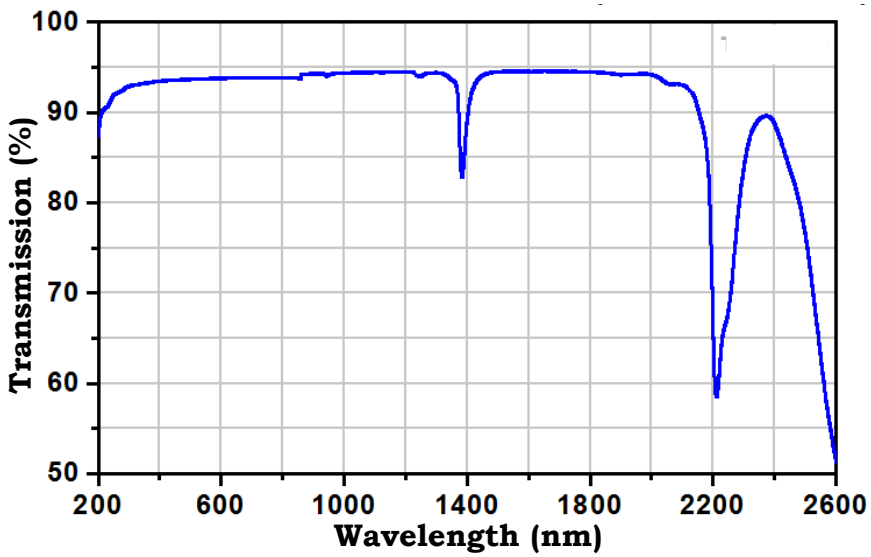

Figure 4.1 Transmittance characteristics of fused quartz glass [98].

4.3.3 Receiver sizing and geometry

The proposed receiver was designed as an insulated cylindrical enclosure to capture incident solar radiation effectively in order to allow radiation to pass through a small opening (aperture). The cylindrical shape is effective in producing multiple absorptions and reflections inside the enclosure, known as the cavity effect. For optimal

thermal performance of the cavity receiver, it is essential that the cavity surface is a black body absorber. For a cylindrical cavity type receiver, apparent absorptivity is greater than 0.979 and surface absorptivity greater than 0.5, when the ratio of the cavity diameter to aperture diameter is around 1.7 and the ratio of the cavity depth to diameter is 2 [20].

At temperatures above 1000K, the net power absorbed by the cavity receiver is affected by radiative losses through the aperture. Thus, aperture size is the most important dimension for determining the amount of power in and out of the cavity. Solar energy absorption efficiency is defined as the net rate at which energy is absorbed, divided by solar power coming from the concentrator. For a perfectly insulated cavity receiver (with no convection or conduction heat losses), the absorption efficiency is given as follows:

$$\eta_{absorption} = (\alpha Q_{aperture} - \varepsilon A_{aperture} T^4) / Q_{solar} \qquad (4.1)$$

This efficiency also depends on the concentration ratio of the system, which is expressed as:

$$C = Q_{aperture} / I A_{aperture}. \qquad (4.2)$$

The concentration ratio of a technically feasible central tower receiver is generally over 1000 [20]. To improve this concentration ratio further, a secondary reflector, often called a compound parabolic concentrator (CPC), is suggested for use with the CSP receiver. Higher concentration ratios allow for a smaller aperture to reduce re-radiation loss. Conversely, larger apertures intercept more sunlight and increase re-radiation loss. Therefore, the optimum aperture size for a maximum $\eta_{absorption}$ results from a compromise between maximizing incident radiation and minimizing re-radiation loss and is determined as follows:

$$\partial \eta_{absorption} / \partial r_{aperture} = 0 \qquad (4.3)$$

The incident flux distribution at the focal plane is assumed to be Gaussian (with maximum flux density F_{peak} and radial standard deviation μ).

Assuming a black body cavity receiver ($\alpha = \varepsilon = 1$) and a simplification of Equation (4.3) yields the optimum aperture radius:

$$r_{opt} = \left[-2\mu^2 \ln(1 - Q_{aperture} / 2\pi\mu^2 F_{peak} \right]^{0.5} \quad (4.4)$$

Equation (4.4) serves to guide the determination of the aperture size for maximizing efficiency. The optimal aperture radius varies from 2.6 to 2.9 μ with respect to peak solar flux intensities between 1000 to 12000 suns. Considering a desired input power of 5kW and F_{peak}=2500kW/m^2; μ=250mm that represents 75% full load, the aperture diameter was calculated to be 60mm.

Taking into account the ratio between the depth and diameter of the cavity, the receiver's cylindrical cavity is proposed at a length of 750mm, 500mm inside diameter, with an aperture diameter of 60mm. The cylindrical cavity was made out of 1.5mm thick stainless steel (SS316) sheet metal and the 60mm aperture was covered by an 85mm diameter, 3mm thick, clear fused quartz glass. A 250mm high, 45^0 inclined conical top was designed to connect the receiver body with the 60mm aperture. The conical top also reduces the amount of re-radiation. The beam diameter of the solar simulator was 12mm at the focal point and diverged from this point. The diverged beam diameter was about 50mm at a distance of 50mm from the focal point. The aperture of the receiver was positioned such that a beam of less than 60mm entered into the cavity aperture. Hence, there was no requirement to design the top conical CPC to concentrate the diverged beam.

Figure 4.2 shows the assembly of the receiver and a photograph of the whole receiver setup. The aperture glass window was actively cooled by air flowing from the outer side and had an aerodynamic protection curtain to keep the inside clear from the particles and/or condensable

gases. Eight air curtains (see Figure 4.3) were used at an angle of 30 degrees in a radial direction into the flange holding the quartz glass.

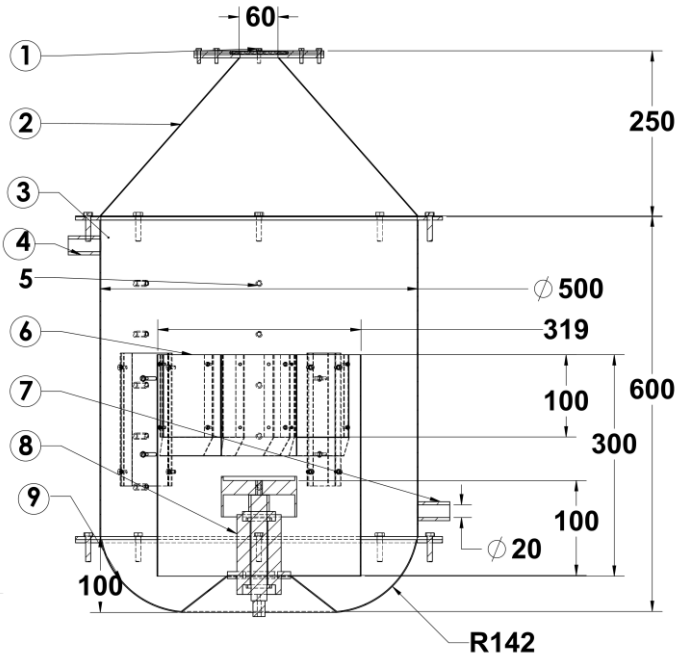

1.	quartz glass	2.	conical top for the aperture	3.	cylindrical receiver
4.	hot air outlet	5.	thermocouple port	6.	fan duct
7.	ambient air inlet	8.	fan holding assembly	9.	hemispherical bottom surface to hold the particles

Figure 4.2 Assembly of the designed receiver and a photograph of the manufactured receiver.

A 20mm inlet port was attached to supply ambient air into the cavity. The inlet port was located 150mm from the bottom of the receiver to mix cold air and particles in the hemispherical shaped bottom of the receiver. The hemispherical shape avoids flow separation and reduces the pressure drop of the gas. In addition, the bottom was designed to act as a particle container during operation. A bearing with a holding cup was placed at the centre of the hemispherical bottom that holds the shaft of the axial flow fan. The fan and motor shafts were connected using a coupling device to avoid misalignment between the two shafts. To exhaust the hot air, which is used for power production, an outlet port of 20mm in diameter was attached 250mm from the aperture. A filter made of sintered stainless steel was attached at the exit to prevent particles from leaving the receiver. To recirculate the particles and air mixture, a ducted fan system was hung inside the cavity, as described in the following section.

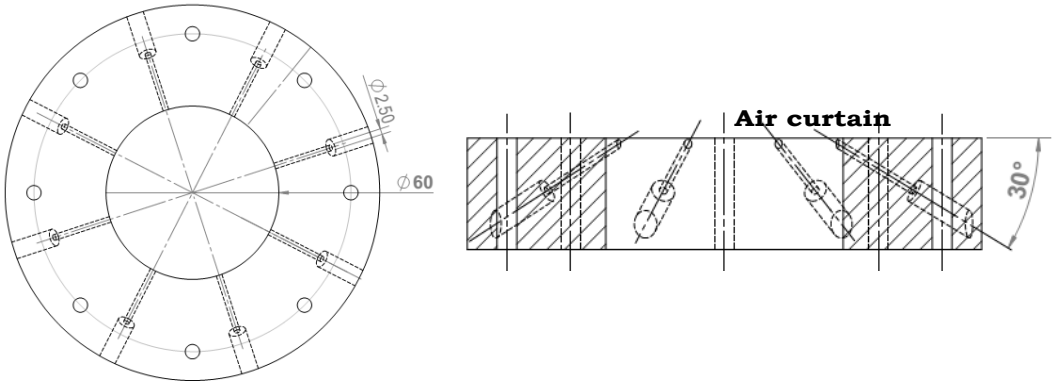

Figure 4.3 Schematic of the designed jet passage surrounding the aperture.

4.3.4 Ducted axial flow fan

As described in Section 3.6, an axial flow fan was required to achieve a continuous forced recirculation of the suspended air-particle mixture into the receiver. An axial fan of 315mm outside diameter and 110mm hub diameter was selected. The fan was specially made of stainless steel 9SS316) alloys for high temperature applications and air-particle mixture suspension operation. The fan was run using a 0.75kW motor and an automatic digital control unit was used to control the speed of the fan.

4.4 Air flow measurement

A Turbulent Flow Instrumentation (TFI) Cobra probe was used to measure 3-D velocity and turbulence intensity in the cavity receiver. The schematic of the test setup is shown in Figure 4.4. Velocity measurement accuracy was 0.3% in the range of 2-100m/s. For improved accuracy, the Cobra probe tip was always directed perpendicular to the flow inside the solar receiver cavity. Adjustment of angular position of the probe head was maintained using a tri-square tool and the probe was fastened to the bottom head of the traverse (Figure 4.5). Data from the Cobra probe was transferred to a data accusation driver which was subsequently used for post processing of experimental data. The probe was mounted on a manual traverse in such a way that it did not interfere with the flow field. It is noted that the cavity diameter was 500mm and the probe head width was 1.4mm. Hence, the probe head did not cause any significant disturbance to the internal flow of the cavity.

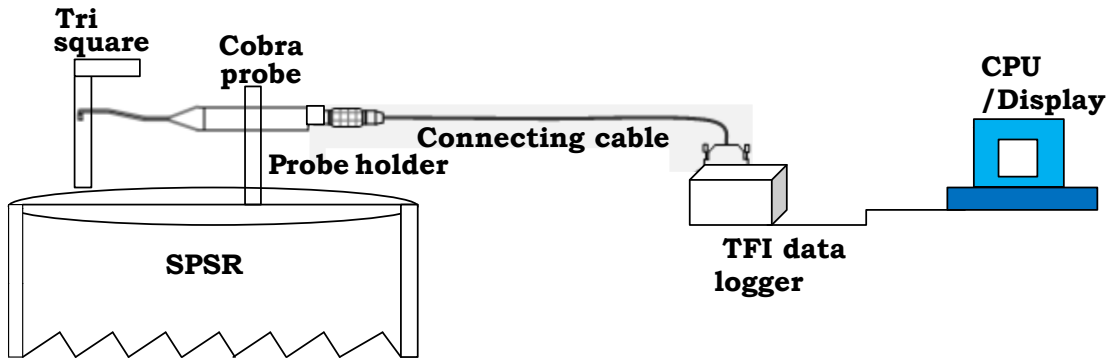

Figure 4.4 Schematic of air flowing measurement setup.

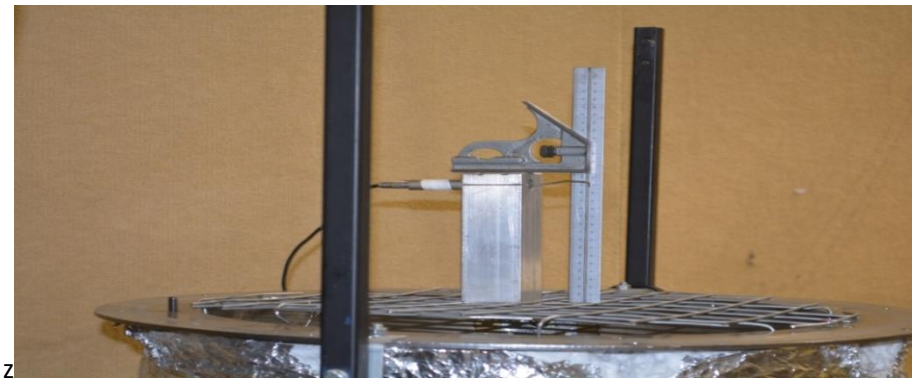

Figure 4.5 Photographic view of alignment test of the Cobra probe.

4.5 Particle concentration measurement

Particle concentration measurement was performed to determine particle flow pattern and particle distribution in the cavity of the solar receiver. This measurement can help to identify the relationship between particle concentrations and thermal performances of the receiver at different a specific fan speeds.

To measure the particle concentration, different methods were considered, such as the ultrasonic attinuation method, ultrasonic impact vibration method, volumetric flask method, and light scattering technique. Among these methods, the light scattering technique is widely used for measurement of the concentration of particles in suspension. This technique is noninvasive in nature and has high sensitivity with the potential for real time detection of particle loading. In this experimental analysis, particle attenuation was measured using the light scattering technique.

The light scattering technique is based on the Beer Lambert Law, which is expressed as:

$$I(s) = I_o^{-\alpha s} \qquad (4.5)$$

Where, α is the absorption coefficient or attenuation and s is the distance along the propagation direction of light. From the experimental values of the intensity of scattered light, I and the intensity of light without being scattered, I_0, α are calculated according to Equation (4.5).

Intensity of light is strongly dependent on the length of propagation within the medium, refractive index and optical properties. Scattering intensity is dependent on the incident wave length, scattering angle, shape, size and optical properties of the system (notably, the refractive index of the suspended particle relative to the suspension medium). Light scattered by an individual particle is described by Mie theory, which is a function of the parameters as described by Equation (4.6):

$$I_{individual} = f(\theta, \lambda, x, n) \qquad (4.6)$$

In the case of a suspended particle medium, the light scattering pattern is determined by the collection of particles in suspension. Therefore, the light scattering pattern is also described as a function of the particle concentration (c) in suspension, as follows:

$$I_{individual} = f(\theta, \lambda, x, n, c) \quad (4.7)$$

Using the above method, the following experimental analyses were conducted for the:

(a) attenuation coefficient for the different particle concentrations in the test cell to establish the calibration curve between the attenuation coefficient and particle concentration;

(b) particle concentration in different regions of the solar cavity at different forced recirculation rates; and

(c) particle concentration at different regions of the solar cavity receiver for different particle sizes at a constant forced recirculation rate.

4.5.1 Experimental setup for particle concentration measurement

Particle concentration measurement in the solar receiver was undertaken using the relationship between the measured extinction coefficient in a homogenous mixture of the same particles and water, with the extinction coefficient measured with respect to fan speed in the cavity receiver. To determine these relationships two experimental systems were designed, as shown in Figures 4.6 and 4.7. The first system, Figure 4.6, was designed to measure particle concentration for a known particle concentration cell with scattered light attenuation. The second system, Figure 4.7, was designed to measure attenuation with respect to rotational fan speed in the cavity. Particle concentration with respect to rotational fan speed was calculated by comparing the plots of the attenuation with particle concentration and fan RPM.

A red diode He-Ne laser was used as a light source for this experiment. The He-Ne laser used for this experiment was operated at a full load condition. During measurement, laser power was set at 5mW to emit a polarised light of 632.8nm wavelength. A chopper device was used to

produce a continuous beam at a specific frequency. Incoming light passed through the chopper, reflected from a beam splitter which was used to divide the light into two signals, a reference signal and an incident signal. The reference signal was then detected by a photomultiplier tube, denoted as Receiver1. The other part of the signal was reflected from a second mirror into a thin lens which was used to focus the beam into the target point of an experimental cell. The thin lens was adjusted in such a way that the incident light beam passed either through the centre of the calibration cell or through the aperture of the experimental test rig.

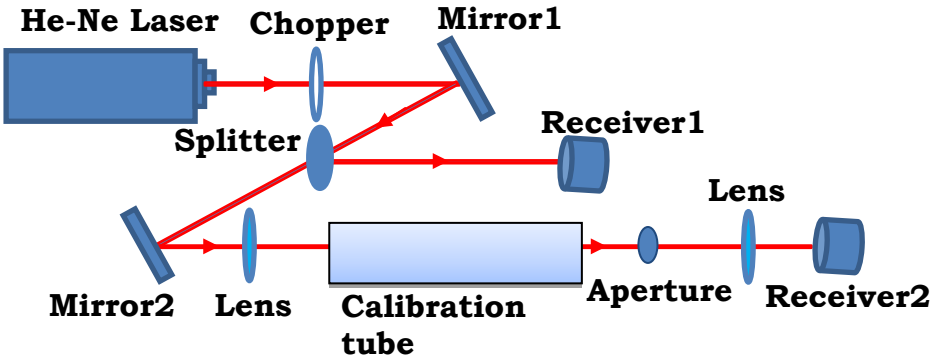

Figure 4.6 Schematic of the optics and calibration cell for the particles' attenuation test at different concentrations of water/particle mixtures.

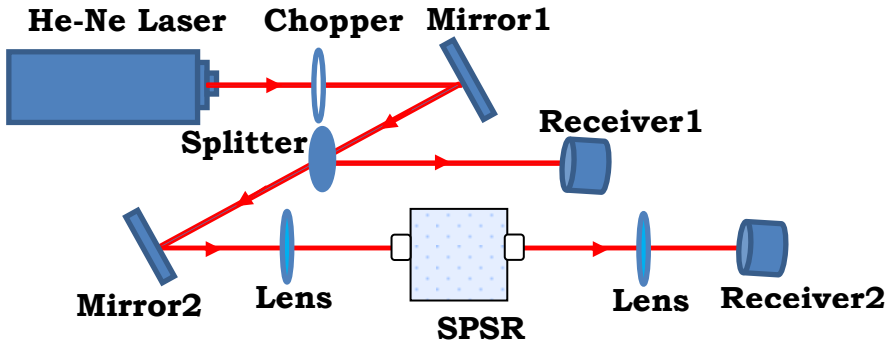

Figure 4.7 Schematic of the laser optics with the solar receiver for particles' concentration measurement.

The concentration was calculated in the sectional volume of the cell, or test rig cavity, through which the incident beam passed. In the calibration setup, an aperture was used to simulate the window of the cavity. An objective lens was placed after the aperture on the other side

of the window to focus the scattered light signal into the centre of the photomultiplier tube, Receiver2. The scattered signal received by Receiver2 was transferred to data acquisition software and recorded as the scattered light intensity. Then, Equation (4.5) was used to calculate the attenuation coefficient for the respective particles concentration. For the protection from the electromagnetic and surrounding light signals, the laser apparatus and signal controller were covered by an aluminium foil box.

4.6 Experimental setup for thermal efficiency measurement

The experimental facility for conducting the thermal performance test of the designed solar receiver is shown in Figure 4.8. The experimental design consists of a 5kW Xenon arc solar simulator (1), a thermocouple (10,11) to measure temperature, an air flow controller with a pressure regulator and an ABB flow meter (7) to measure the flow rate, a speed controller to control fan RPM, a test rig solar receiver and a beam down system with a cooling unit (3). The Xenon arc lamp system comprises a parabolic reflector to concentrate the beam (2) into a focal point with a concentration ratio of 1000. The solar simulator had a similar light spectrum to the sun radiation. A comparison between both spectra is shown in Figure 4.11 [100]. Radiation heat flux of the solar simulator incident on the aperture of the receiver was measured using a separate experimental arrangement at the same power as was used during the experiments (Section 4.7.1).

The solar simulator was designed to such it can be installed horizontally. However, the solar receiver was designed to concentrate the beam vertically down in the solar collector system. Therefore, a beam reflection mirror system (described in Section 4.6.5) was used to reflect the beam vertically downward. The beam reflection mirror was positioned 30mm away from the focal point of the beam, where the beam diameter was 20 mm. The 20mm beam developed a heat flux of 500 suns at the incident point of the mirror. The test rig was located vertically underneath the beam reflection mirror so the reflected beam

entered directly through the quartz glass mounted on the aperture. The distance between the aperture of the solar receiver and angular position of the beam reflection mirror was adjusted in such a way that a beam of 50mm diameter could directly enter the 60mm aperture of the solar receiver without spillage. Nonetheless, a small part of the diffused light passed as spillage and reflected from the quartz glass.

The quartz glass at the window was kept clear using an auxiliary air jet injected in a radial direction. Also, a second auxiliary air jet was used for cooling the beam down mirror. Cooling of the quartz glass and aperture surface helped reduce re-radiation losses as the reflectance of the beam by the mirror increased with the increasing surface temperature of the mirror. To keep the mirror temperature below 100^0C during the test, a continuous cooling air jet was applied. The mirror cooling air also cooled the outer surface of the quartz window as it passed over the window after passing over the reflector.

The total air flow rate was controlled by an ABB flow meter. The air pressure was kept constant using a pressure regulator with the ABB flow meter. In addition, a pressure gauge was attached to the receiver to monitor pressure inside the solar receiver. Subsequently, a safety valve was used to release internal excess pressure. Atmospheric pressure was maintained at inlet and inside the cavity during the experiment. To speed up the experiments, an air preheater was used at the inlet to heat the receiver to 373K. After one and half an hour, preheated air was stopped when receiver was reached to the mentioned 373K. Then; a continuous, specific percentage of ambient air was supplied through the inlet port of the solar receiver.

A particle port was used to introduce a specific percentage of particles into the receiver, which was aimed at the conical CPC part of the receiver. After introducing the particles, the port remained closed during the experiment. Outlet gas was expelled through the outlet port positioned 400mm above, and on the opposite side of, the inlet. A porous sintered disk of 60micron was used to filter the particles from the outlet gas. Outlet and inlet air temperatures, the temperature of

the mirror, receiver surface and receiver cavity volume temperatures were measured using N and K type thermocouples. A detailed discussion of the temperature measurement procedure is described in Section 4.6.1.

4.6.1 Temperature measurement

To calculate thermal efficiency of the receiver, inlet and outlet air temperatures were measured using two K type thermocouples. Two additional K type thermocouples were attached to the surface to continuously monitor the mirror and receiver surface temperatures. These two thermocouples were constructed from a SS316 sheath material with a tip diameter of 0.5mm for each junction. The accuracy of the thermocouple was ±0.75% at a temperature range of 0^0C to 375^0C.

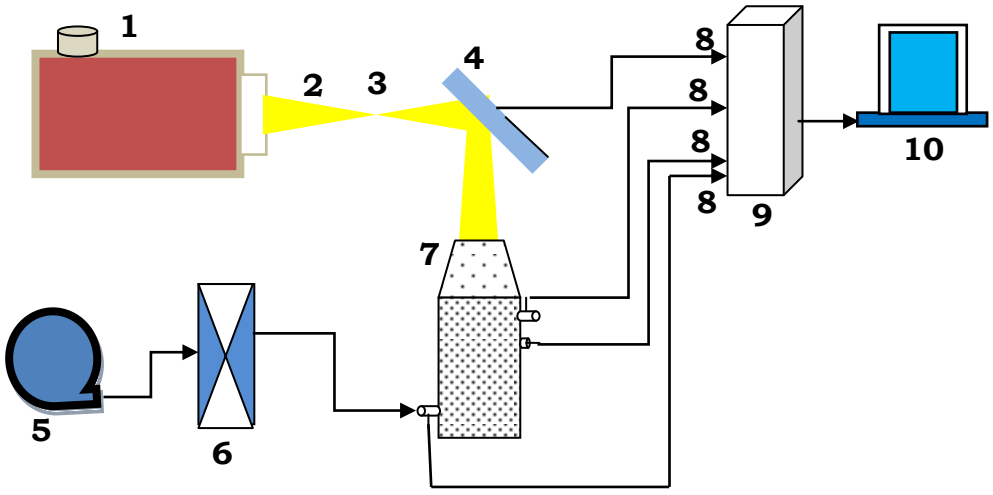

1.	Solar simulator	2.	Radiation beam	3.	Focal point
4.	Aluminium reflector	5.	Compressor	6.	Flow controller
7.	SPSR	8.	Thermocouple signals	9.	DAQ, 10 CPU

Figure 4.8 Schematic of experimental design for thermal testing of the solar receiver.

The receiver cavity temperature was measured using two N type thermocouples. The thermocouples were positioned such they are not exposed to direct irradiation. To measure internal temperature of the solar receiver, twenty thermocouple ports were installed on the receiver wall. The ports were arranged in four columns equi-spaced on the

internal periphery. Since the flow of the receiver was characterized as a recirculating flow, only one port at the top and one at the bottom of the receiver were used.

Outer surface temperature was measured using an infrared thermometer. Thermocouple signals were collected by a data logger. Real time tracer DAQ software was used to convert the signal to time-averaged instantaneous temperatures. Measurements were recorded every five seconds. The average temperature was determined from 1800 temperature signals at each time interval.

4.6.2 Solar simulator apparatus

A solar simulator was used to simulate solar irradiance and spectrum. The three major components of a solar simulator are a light source and power supply rectifier unit, an optical train to modify the output beam and a control system to operate and adjust the performance of the simulator. The general arrangement of the solar simulator apparatus is schematically shown in Figure 4.9. The experimental solar simulator used in the experiments has a 5000 watt Xenon light source that provides scattered beam radiation. The scattered beam from the Xenon arc is converged by an elliptical reflector which is mounted inside a Cinemeccanica lamp housing (see the description in Section 4.6.4). The Xenon lamp in the lamp housing was mounted horizontally at the focal plane of the elliptical reflector. The focal point of the elliptical reflector was at 208±2mm from the outlet of the lamp housing. A highly polished and flat shaped aluminium mirror was positioned at an angle of 45^0 so that the horizontal beam focused from the Xenon lamp house was reflected downwards.

Variable heat flux was achieved at a different location of the converged and diverged beam of the light source. An adjustable metal frame of 2.5m long, 1m wide and 1.2m high was used to support the solar simulator. The horizontal beam position was altered by positioning the adjustable metal frame.

4.6.3 Xenon short arc radiation source

There are a number of important factors to be considered when choosing a light source from a solar simulator. As lamp power is a primary indicator of light intensity, lamp wattage is the main parameter defining the light intensity. Control of voltage and ampere is another factor in controlling the illumination level and beam brightness. Thus, there is a need to control the power setting in order to adjust the lamp to the required irradiance intensity.

The intensity distribution curve of the radiation source matches the global solar radiation intensity curve. Thus, optical components of the lamp-like reflector of the lamp housing should be designed in such a way that it can provide a real intensity curve as per global solar radiation. In order to adjust the radiation intensity of the Xenon lamp, the following criteria were considered:

(i) The focus of the light source depends on the reflector shape and size. Thus, the reflector shape and size were designed as either a point or flat source. A parabolic reflector is generally used for point focusing systems.

(ii) Electromagnetic content irradiating from the light source depends on the spectral distribution of the light source. Spectral distribution exposes the specific wavelength intervals and can reveal the characteristic of narrow band emission lines.

The Xenon bulb (Figure 4.10) used in the solar simulator design is capable of providing a continuous electromagnetic spectrum from 240nm up to 3000nm. Figure 4.11 shows a comparison of irradiance from a typical Xenon short arc lamp compared with solar extra-terrestrial irradiance and for air masses (AM) 7 of 1.5. The results indicate that pronounced peaks are achieved in the Xenon spectrum between 850nm and 1000nm, providing approximately twice as much infrared radiation in proportion to ground level global solar irradiance (Figure 4.11).

Table 4.2 Specification for the Xenon XBO 5000W/HBM OSRM lamp.

Parameter	Value
Rated Lamp wattege	5000 W
Rated Lamp Voltage	34 V
Rated Lamp current	140 A
Luminous flux	225,000 lm
Luminous intensity	27,000 cd

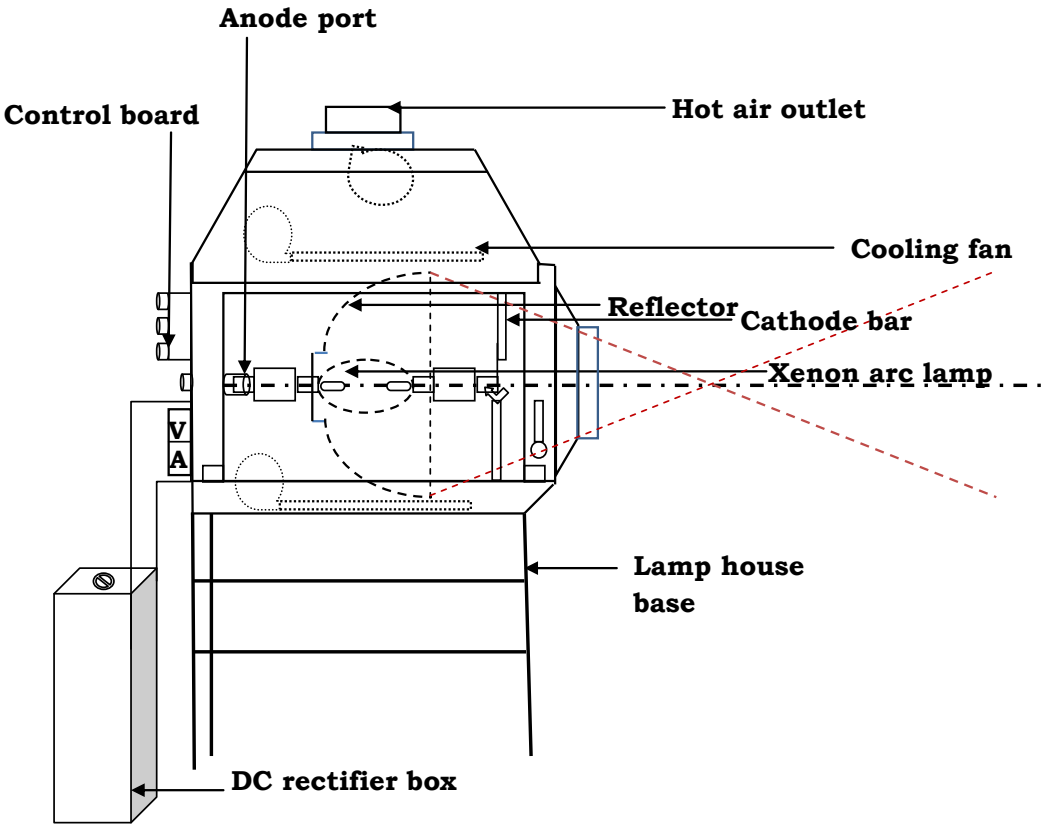

Figure 4.9 Schematic of the solar simulator apparatus [100].

Figure 4.10 Photograph of the HLR Osram 5kW Xenon short-arc lamp used in the experiment.

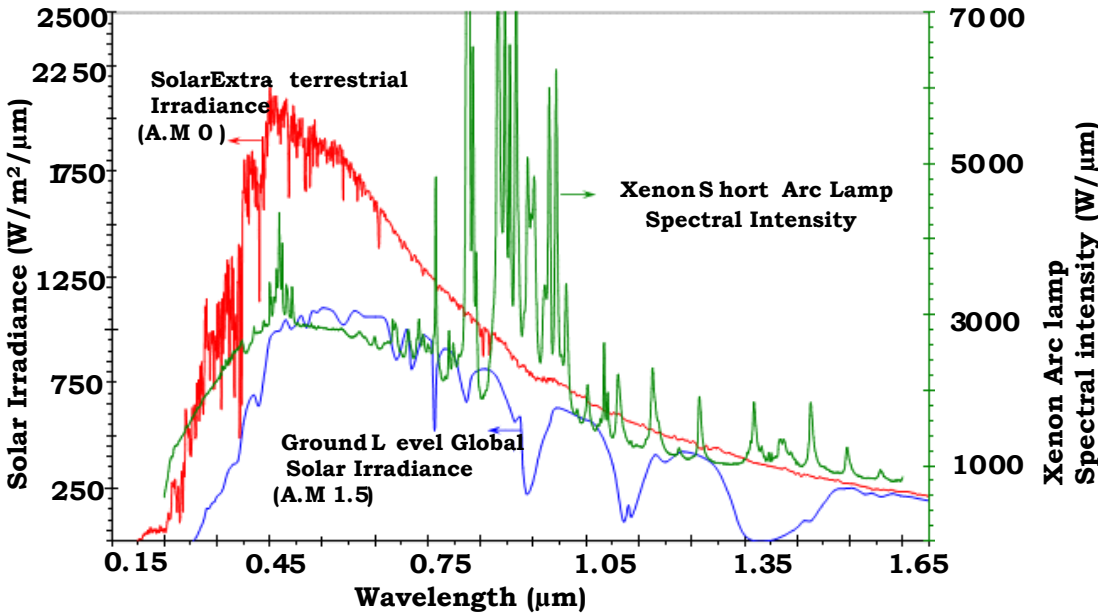

Figure 4.11 Spectral intensity of a Xenon arc lamp compared with extra-terrestrial and ground level solar irradiance [100] .

Cinemacanica-Malino lamp housing was used to locate the 5000 watt Xenon arc lamp for simulating the sun. An IREMN3X1140DM rectifier power supply device was used to supply power to the Xenon arc bulb. To operate the lamp, a three phase 415 Volt AC power was connected to the rectifier to convert the AC to a range of 30-39 Volt and 140 Amp DC.

According to the design of the lamp housing, shown in the schematic of Figure 4.9, the Xenon arc bulb was located horizontally. It provides three dimensional movements for the Xenon bulb using an elliptical reflector. Hence, the focal length of emitted light from the lamp housing can be adjusted as required. According to Nostel et al. [102], reflectivity of the elliptical reflector was estimated at approximately 0.97 over most wavelengths.

The elliptical reflector produces a convergent and divergent beam by concentrating scattered light from the Xenon bulb. The calculated divergent and convergent beam diameter with respect to the rear of the reflector is shown in Figure 4.12. Note, the change in diameter of the illumination spot as the radiation beam converges to the focal point and then diverges again. At the focal point, a diameter of 12mm was produced and was adjusted such that the focal point position moved to 208mm ± 2mm from the front face of the lamp housing. The diverging radiation beam leaves the Cinemeccanica lamp housing horizontally through a 110mm diameter opening from the front face of the lamp housing.

4.6.4 Beam deflection mirror

The recirculating flow solar receiver aperture is in a vertically upward position, so the beam of the solar simulator should be deflected vertically downward, as shown in Figure 4.8. To achieve this, a beam down reflector was used. The position of the reflector was maintained at such a height and separated from the solar simulator lamp house aperture so that the diverging beam diameter could pass through the quartz window supported aperture of the solar receiver. Polished aluminium, glass and stainless steel are generally used as reflectors. In this application reflectance of the reflector was required as high as possible. A metal reflector is easy to produce to a required shape and is cost effective; however metallic reflectors have spectral, absorption and reflection limitations.

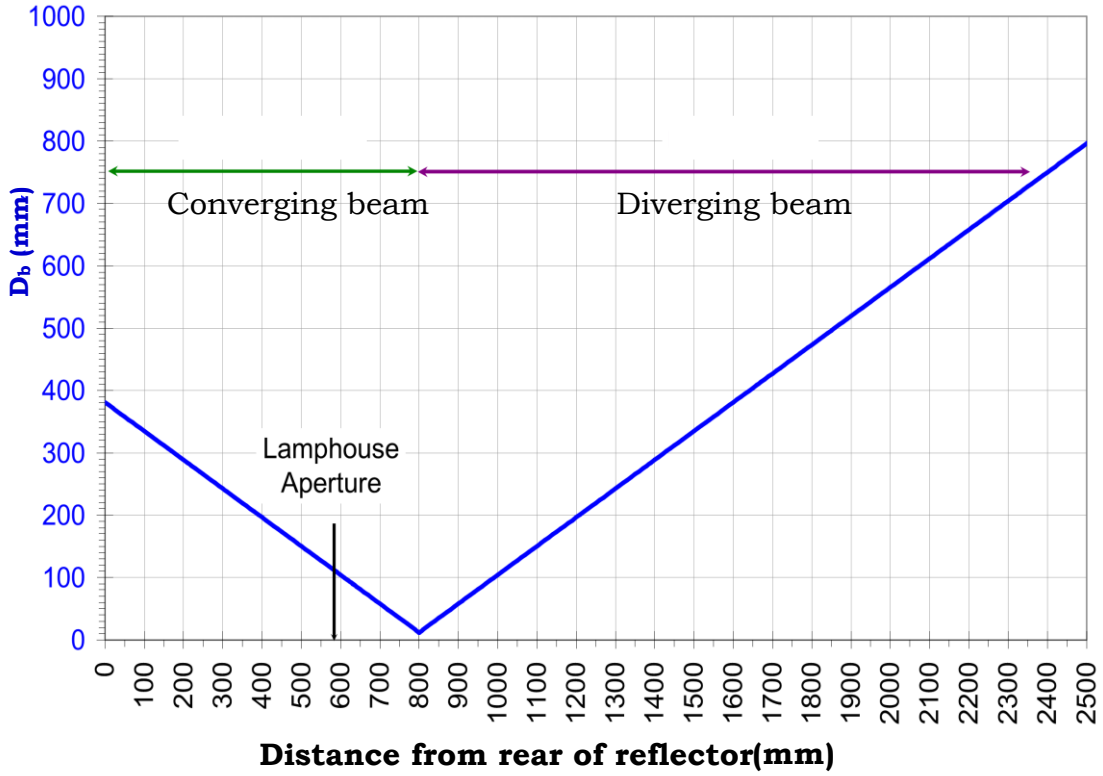

Figure 4.12 Calculated beam diameter. D_b as a function of distance from the rear of the lamp housing's reflector [103].

Figure 4.13 shows reflectance of the emitted radiation by stainless steel, silver, aluminium and glass lies between the wavelength 0.3μm and 2.5μm. Stainless steel has a higher thermal resistance, higher resistance to mechanical wear and chemical corrosion, but comparatively lower reflectance of radiation when compared with aluminium and silver. Specular silver with vacuum deposited clear polyester film has been shown to reach a reflectivity of about 90-95%.

Polishing and coating on the aluminium mirror produces a reflective surface of reflectance above 91%. Aluminium and silver exhibit over 90% reflectance across the entire wavelength. Compared with silver, aluminium is cheaper and easier to machine. In the experimental test, a polished aluminium reflector was mounted to project the beam into the solar receiver. The mirror was made of marine aluminium 5083, with the dimensions 200×140mm^2.

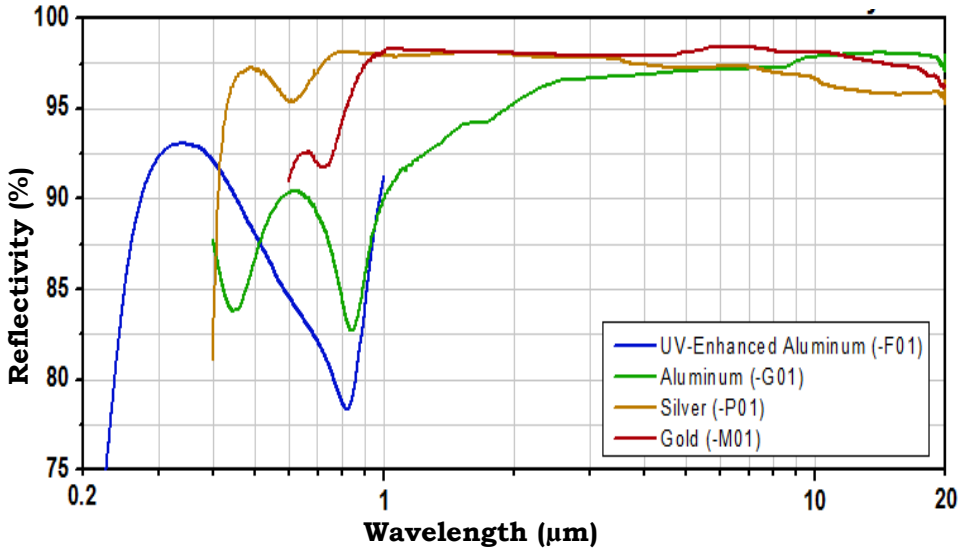

Figure 4.13 Reflectance of stainless steel, aluminium and silver between 0.3µm and 2.5µm [102].

The mirror was polished mechanically and then finely polished using the metal polish liquids Plastic-o, Brass-o, and Silver-o. Additional coatings or a coating of glass on the aluminium polished surface, are effective ways to maximize the reflectiveness of aluminium.

4.7 Heat flux of a 5kW Xenon arc lamp

Solar simulator heat flux is measured by radiation intensity per unit area on the incident surface. Figure 4.9 shows a schematic of the concentrated beam from the Xenon arc solar simulator. The radiation beam emitting plasma arc reflects from the elliptical reflector, which concentrates the radiation beam horizontally through the aperture at the front of the lamp housing. Beam diameter is measured using this focal point and the converging/diverging ray of the elliptical reflector. The elliptical reflector converges the radiation beam to a 12mm diameter at the focal point, which is 210mm apart from the lamp housing aperture front.

Total radiation heat flux of the solar simulator Xenon arc lamp was calculated using the electrical input of the lamp house, the beam diameter and the Xenon arc lamp conversion efficiency from the supplied electrical energy. The supplied Voltage and direct current to

the bulb was recorded to achieve the power developed by the Xenon arc lamp. The recorded Volts and current were 30± 0.2 Volts and 137± 0.2 Amps. The total power was calculated as, P=V x I=4219± 34 watt.

Tables 4.3 and 4.4 show the percentage of energy emitted by the Xenon arc lamp. Table 4.3 shows that total conversion efficiency from electrical power to radiation energy is about 49%. According to this conversion efficiency, the converted radiation beam from the electrical power=2072± 17 watt and average heat flux at a focal point beam of 12mm diameter was 18MW/m^2 as shown in Figure 4.14.

Table 4.3 Solar energy conversion of Xenon light source.

Parameter	Value
Total ultra violet(200nm to 400nm)	2.32%
Total visible(400nm to 700nm)	11.79%
Total infrared (700nm to 1400nm)	34.84%
Total output energy to input	48.95%

Table 4.4 Spectrum analysis of Xenon Lamp light source.

Band	Spectrum Range	Percentage of energy from range	Cumulative percentage
UVC	<280	0.3	
UVB	280-320	1	5.4%
UVA	320-400	1.2-2.9	
Visible	400-700	4.2-5.6	9.8%
Infrared	700-2500	2.6-8.1	65%

Table 4.5 Heat flux transducer specification.

Parameters	Specification
Sensor	64 Schmidt Bolter series
Heat flux range	2000Btu/ft²-sec (150% over range)
Maximum linearity	±2% of full range
Reputability	±0.5%
Temperature capability of sensor	400⁰F
Output signal	10 milliVolt ± 1.5 milliVolts

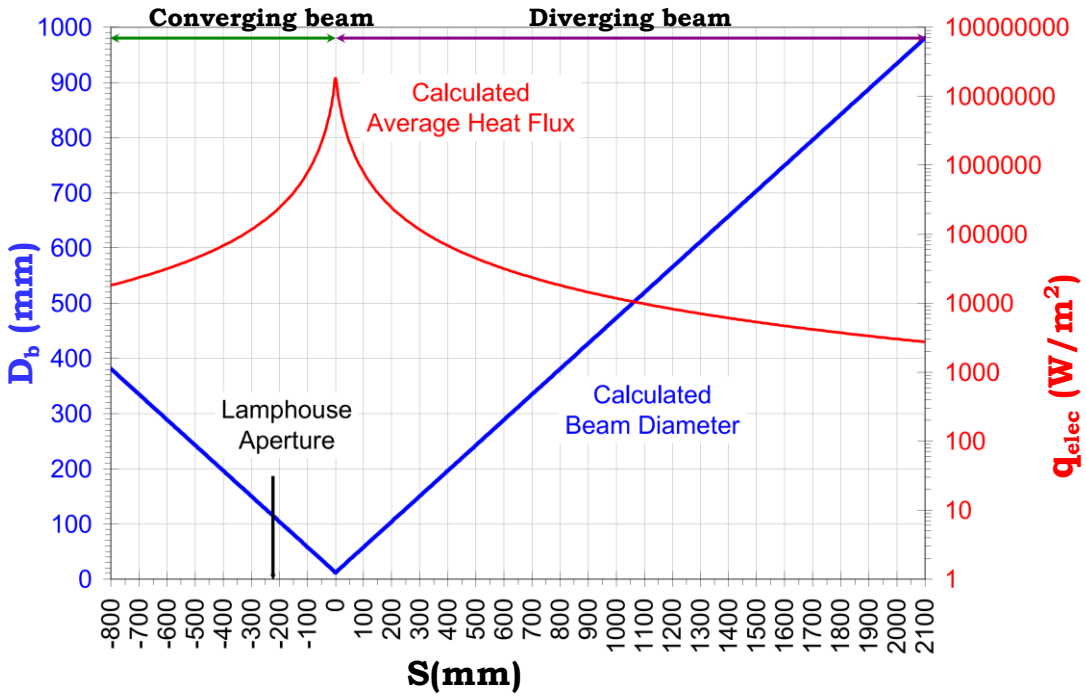

Figure 4.14 Calculated beam diameter D_b and average heat flux q_{elec}, as a function of distance S from the focal point for 49% conversion efficiency.

4.7.1 Heat flux measurement of the solar simulator

The theoretical heat flux of the solar simulator was calculated using the electrical power supply. During the experiments, the solar simulator radiation beam reflected downward using the polished aluminium deflect mirror and then entered the solar receiver passing

through the quartz window aperture. A 64-series Schmidt-Bolter heat flux transducer was used to measure radiant heat flux from the Xenon arc lamp radiation source. Specifications of this heat flux transducer were provided in Table 4.5. The maximum calibrated value of heat flux was 11.35kW/m^2.

Complete design of the heat flux measurement is shown in Figure 4.15. In this experimental design, the mirror and quartz glass were positioned 30mm apart, similar to the thermal test experiment. The transducer was positioned vertically upward at different measurement points using a traverse. Heat flux of the Xenon arc source at the focal region was approximately 1000sun that was outside the nominal calibration range of the transducer**.** Within the nominal range of heat flux, the closest distance to the focal point at which the transducer could be placed was 750mm. Hence, measurements were taken beyond 750mm of the focal point. Data from the heat flux transducer were collected using a data analogue scanner module 7220 unit. An amplifier was used to amplify the signal of the sensor which was adjusted during heat flux calculations. The amplifying signal was captured by the data scanner module and then displayed to the CPU.

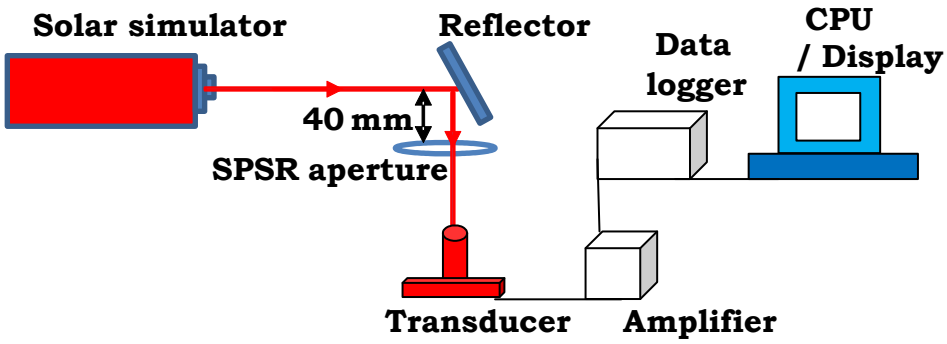

Figure 4.15 Schematic of experimental setup for the heat flux measurement of the Xenon arc solar simulator.

4.8 Summary

A detailed understanding of the design requirements of the solar receiver, test setup, equipment used in these experimental analyses and the methods of investigations were discussed here. Four test

setups namely: (i) fluid flow measurement (ii) recirculating particle concentration measurement (iii) outlet air temperature measurement (iv) measurement of heat flux of the solar simulator was discussed. Techniques and limitations for the measurements were introduced. These overviews of experimental facility and method of investigations were put forward to understand the experimental procedure discussed in the following chapters.

Chapter 5

Fluid dynamics behaviour

5.1 Introduction

This chapter presents the results of experiments that analysed the fluid flow field and particle concentration in the cavity of the solar receiver. The experiments were performed in two campaigns: fluid flow characteristic measurements and internally recirculating particle behaviour tests. In the first section of the analysis, fluid flow behaviour was investigated to characterize recirculating flow. Three dimensional velocity and turbulence intensity were measured using a Cobra probe. Parametric investigation was conducted to determine the required speed of the fan to recirculate the metallic particles. In the second campaign, local concentration of recirculating particles was measured. Stokes numbers were calculated to understand particle recirculation characteristics within the fluid stream for a specific rotational fan speed.

5.2 Flow field measurement

A schematic view of the experimental setup for measurement of the air velocity in the cavity of the solar receiver is shown in Figure 5.1. These measurements involved the test rig solar receiver, data acquisition system and a Cobra probe to measure the three dimensional velocity. A ducted axial flow fan operated by a 0.55kW motor was used to maintain the recirculating flow pattern. The fan rotational speed was controlled using a digital controller. The probe tip was kept aligned vertically and was held in the opposite direction to the flow.

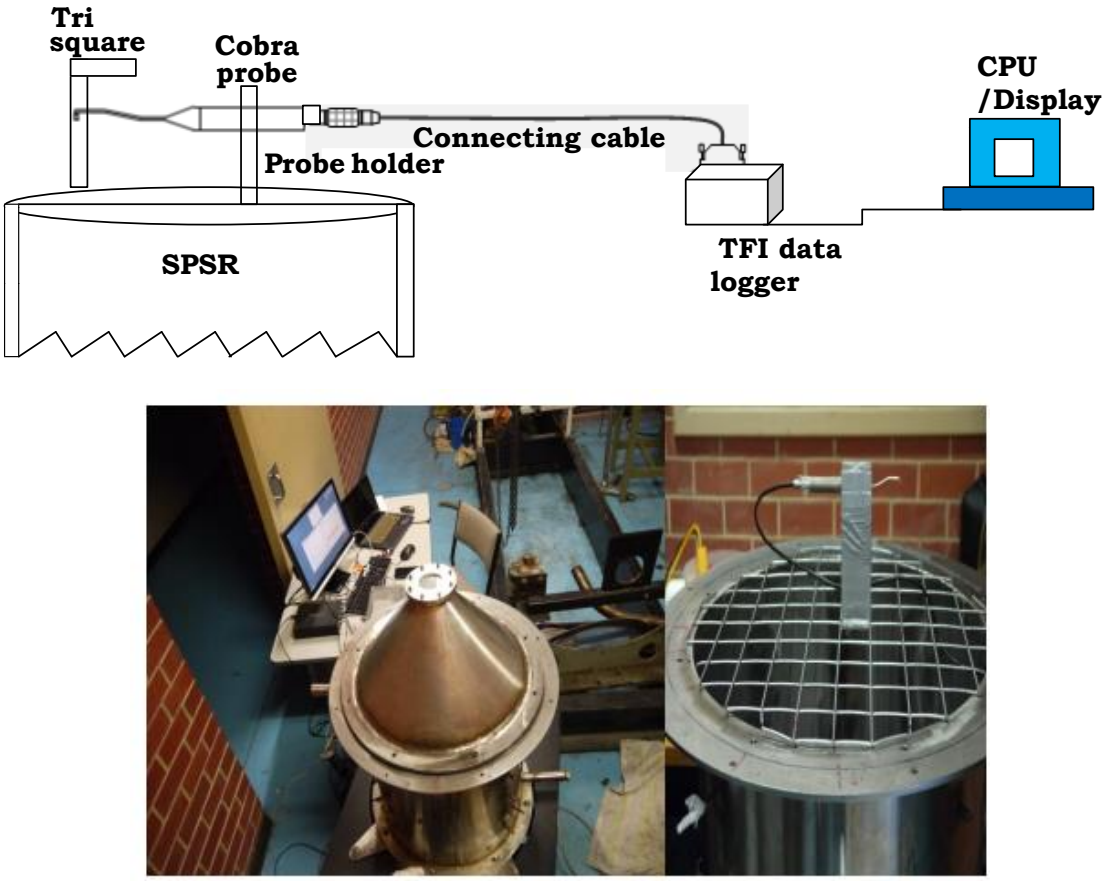

Figure 5.1 Schematic and Photographic view of the velocity measurement setup.

5.2.1 Experimental procedure

Receiver with ducted fan

A 2D view of the receiver with ducted fan system is shown in Figure 5.2a indicating the locations of the measurement points. Velocity was measured at various locations in the cavity to observe fluid flow behaviour over the whole cross section of the receiver. A 50x50mm^2 mesh was used as a grid to position the probe holder at different locations in the cavity. For the first set of measurements, the mesh was placed between the cylinder top and bottom flange of conical top. Then, the probe holder was hung on the mesh using a screw and plate cap. The coordinate system for this measurement was shown in Figure 5.2. In this test, the bottom face of the receiver was considered as the origin. Four different lengths of the probe holder were used to measure velocity at Y=350mm, Y=450 mm, Y=550mm and Y=650mm. Note that

the total height of the receiver was denoted as H=850mm. The bottom of the probe holder consists of a special key operated hole to hold the Cobra probe. The probe was mounted sufficiently below the grid as not to cause major impact on the flow in the cavity. The inlet, outlet and thermocouple ports were sealed using inserts during all measurements. When the motor was started at a specific speed, the Cobra probe measured the velocity at the specified location which then was processed by turbulent flow instrumentation (TFI) software.

Flow test was performed using the arrangement, as shown in Figures 5.2a and 5.2b. In the experimental arrangement, Figure 5.2a, a cylindrical duct was used with the fan to achieve a uniform recirculating flow from the inner to outer periphery of the solar receiver. This flow pattern is expected to achieve a better interaction of the fluid and particle mixture with the receiver wall. However, a set of thermal tests confirmed that as particles flowed upwards near the boundary wall a layer of very fine particles was deposited on the aperture window. At a specific speed, particles were carried to the window and a layer of particle dust restricted the incident beam from entering the receiver uniformly. In order to solve this problem, eight tangential jets of air were installed beneath the aperture to clean the window. While this reduced deposition it did not eliminate the problem entirely as some deposition still appeared on the window after a few minutes of continuous operation.

Receiver with particle stopper

To address the issue of particle deposition on the window a particle stopper, as shown in the schematic view of Figure 5.3, was used and a cold flow test was performed using 200micron SiC particles to investigate the fan rotational speed at which particles did not deposit on the window. The stopper was designed as circular conical cone as shown in the Figure 5.3. The outer diameter of the cone was equal to the inner diameter of the receiver. The inner diameter of the stopper was 319mm which was approximately equal to the outer diameter of the fan. The slope of the cone was taken 45 degree. It was found that

for cold flows the fan could operate at up to 1500RPM without particle deposition on the window (Figure 5.4). Then, the thermal tests were performed using this configuration. For this case, after putting the stopper at Y=350mm, the air flow velocity was also measured for different RPM. The measurement procedure was similar to the previous case (the ducted fan case).

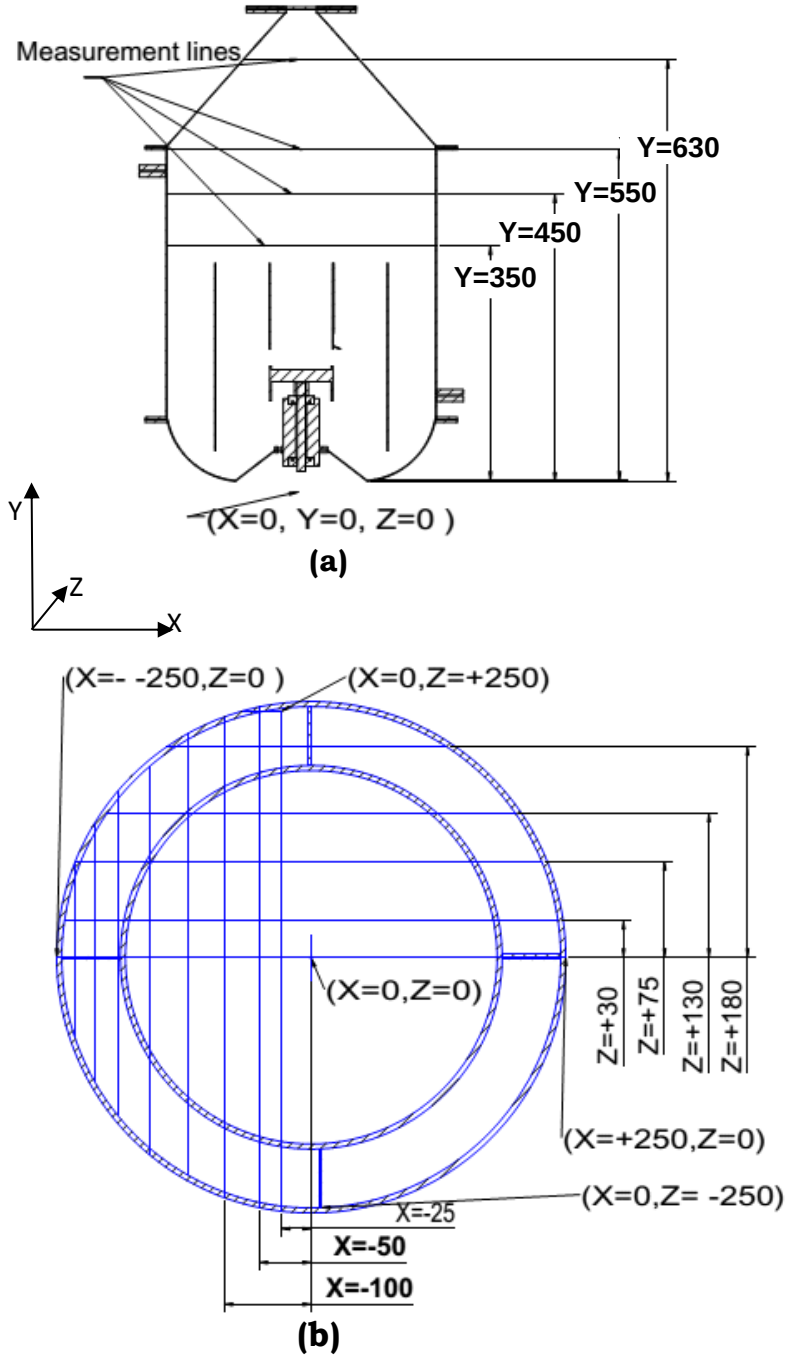

Figure 5.2 Schematic cross section views showing air flow measurement locations (receiver with ducted fan) and geometrical arrangement (a) XY cross section (b) XZ cross section.

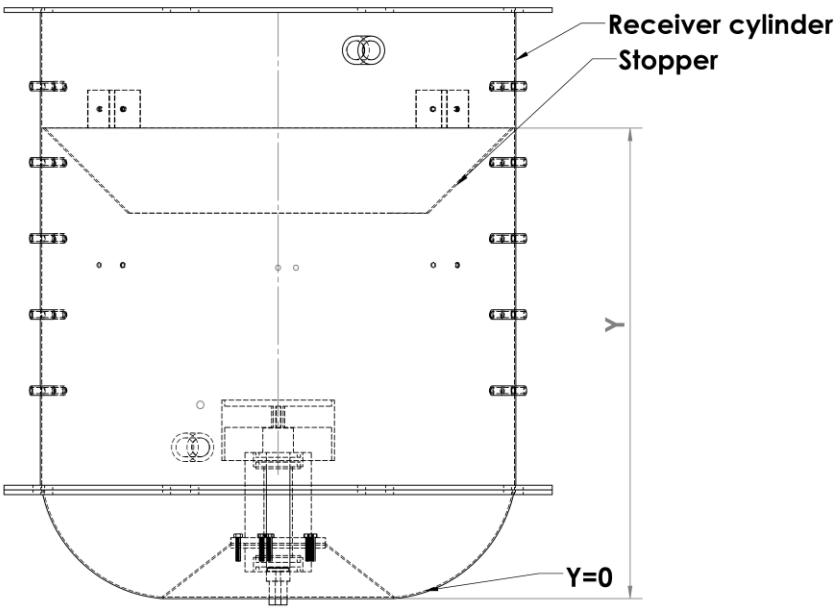

.

Figure 5.3 Schematic of the cross section views of the receiver cylindrical part showing stopper location (receiver with particle stopper).

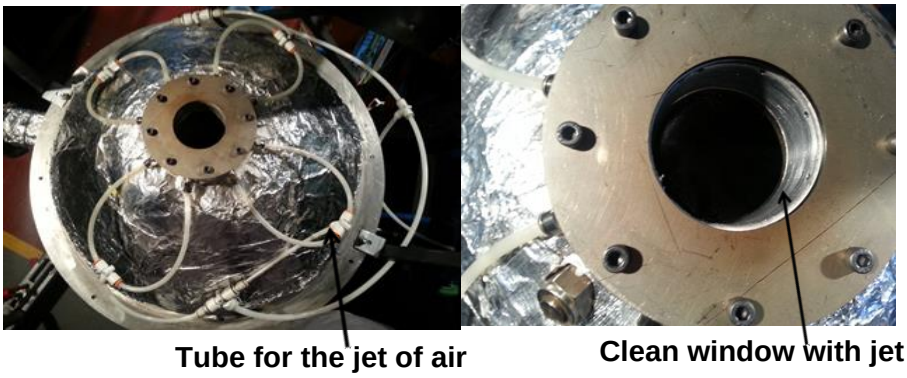

Figure 5.4 Photograph of testing the quartz window with recirculating particles at 1500RPM (with air jet and particle stopper).

5.2.2 Measurement uncertainties

In these experiments measurement uncertainties include system accuracy, random error and repeatability error. The manufacturer accuracy rating of the Cobra probe is within 1% of the measured value for the range of 2-60m/s. Random error was reduced by ensuring that many samples were collected over time and that the average value of the measured data was statistically independent.

Means of total collected data n, of the measured variables x_i were calculated as follows:

$$\bar{x} = \frac{\sum_i^n x_i}{n} \tag{5.1}$$

Then, random uncertainty was calculated as:

$$V_x = \sqrt{\frac{\sum_i^n (x_i - \bar{x})^2}{n(n-1)}}, \tag{5.2}$$

Where the standard deviation of the measured variables set was

$$S_x = \sqrt{\frac{\sum_i^n (x_i - \bar{x})^2}{(n-1)}} \tag{5.3}$$

Total uncertainty was calculated as: $V = \sqrt{V_x^2 + V_y^2 + V_z^2}$ (5.4)

Using the equation (5.2), random uncertainty was calculated from the measured velocity of flow which was less than 0.23%.

A calibrated Cobra probe was used in the experiment. In addition, the axial velocity was calibrated during the experiment using a Pitot-static tube and a second Cobra probe with a 2 to 12m/s velocity range (Figure 5.5). Results of the calibration test were shown in Figure 5.5. Figure 5.5 shows that the velocity measured by the Cobra probe was similar in magnitude and trends as for the Pitot- static tube. The measured velocity was matched with a 45^0 inclined line as shown by the Figure 5.5.

The main source of error in the measurements was misalignment of the probe tip. However, to position the tip parallel to the flow, a square tool (an alignment tool) was used. According to S.Chue [104] a misalignment of less than 10 degree of the tip produces an experimental error of 1%. Thus, an absolute error of 1% was deemed acceptable for misalignment of the probe tip as more accurate alignment was difficult to achieve in practice. Considering the accuracy of the probe and misalignment error, the estimated error calculated by Equation (5.4) was 1.44%.

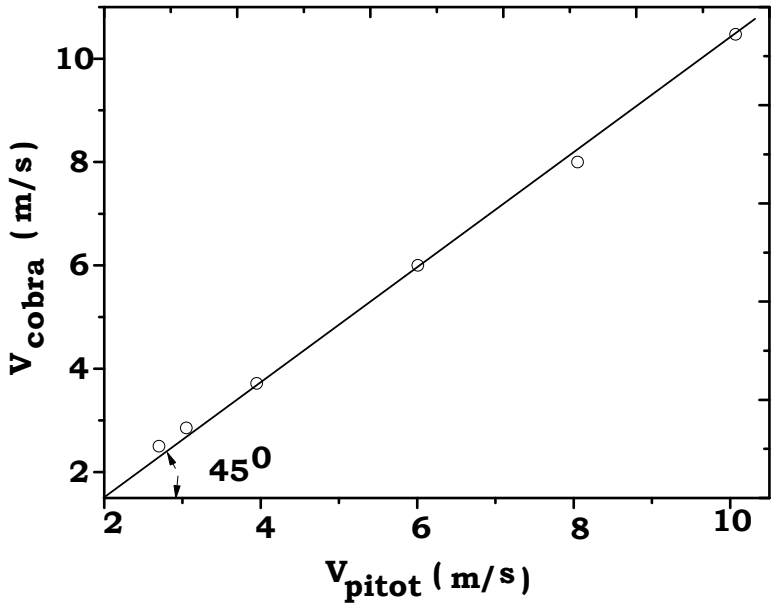

Figure 5.5 Variation of Cobra probe accuracy with respect to Pitot- static probe.

5.2.3 Results and discussion

The co-ordinate system for velocity measurement is shown in Figure 5.2. Velocity was measured along the X axis at Y=350mm, Y=450mm, Y=550 and Y=630 above the duct surrounding the fan (see Figure 5.2a) and plotted against the radial distance of the solar receiver (see Figures 5.6 to 5.8). Table 5.1 shows the measurement points in the XZ plane.

In the experimental investigation, three components of flow velocity were measured, including the axial component Vy, the tangential component V_θ, and the radial component V_r. The flow direction moving from the bottom to the window was referred to as upward flow (a positive sign depicts upward flow in the graph). The flow direction moving from the window to the bottom was referred to as downward flow (a negative sign depicts downward flow in the graph). Figures 5.6 to 5.7 present the total velocity plots of the air flow and show that the flow direction was directed from the bottom to the window between the receiver wall and duct wall. The same Figures show the negative flow velocity of the downward air flow through the middle of the receiver i.e. through the duct. The velocity profile shows that flow was recirculating from the receiver wall towards the centre of

the cavity. Upward flow velocity was higher than downward flow velocity. The difference between upward and downward flow occurred due to suction pressure generated by the fan being lower than delivery pressure. In addition, the radial and tangential components of flow velocity were changed to the axial component near the receiver boundary wall, as the boundary of the receiver acted as a guide vane and changed the tangential and radial components to the axial component.

Table 5.1 Table showing the measurement locations

Probe position, Y (mm)	Probe position, Z(mm)	Probe position X(mm)
Y=+350	±30	±0, ±25, ±50, ±75, ±100, ±125, ±150, ±175, ±200, ±225, ±245
	±75	±0, ±25, ±50, ±75, ±100, ±125, ±150, ±175, ±200, ±225
	±130	±0, ±25, ±50, ±75, ±100, ±125, ±150, ±175, ±200
	±180	±0, ±25, ±50, ±75,±100, ±125, ±155
Y=+450	Same as, Y=+350	Same as above, Y=+350
Y=+550	Same as, Y=+350	Same as above, Y=+350
Y=+650	Same as, Y=+350	Same as above, Y=+350

The velocity profile at Z=±180mm shows that upward flow velocity was at a maximum of 5m/s for 1500 RPM (see Figure 5.6). Near the outside guide vane of the duct, shown in Figure 5.6, an increase in upward velocity was observed at Z=±180mm because the air was pushed up by the straight vane between the duct outer wall and the receiver boundary wall (see Figure 5.6 and Figure 5.7). Upward flow velocity was higher near the receiver wall than the region near the casing wall in all cases. The maximum upward velocity at Y=350mm was 7.8m/s, and at Y= 450mm it was 6m/s which demonstrates that the upward flow velocity decreased when the measurement height increased.

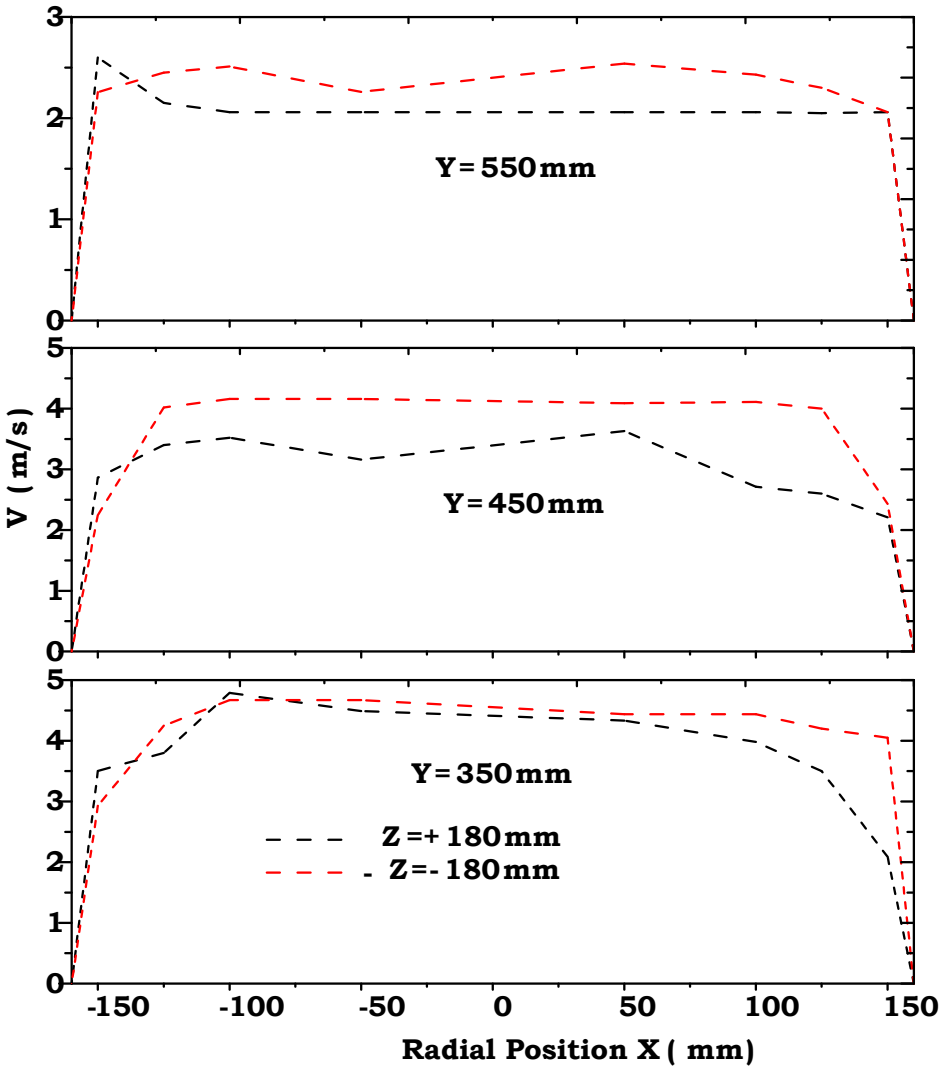

Figure 5.6 Variation of total flow velocity with the radial position along the X axis at Z=±180mm and RPM=1500.

The upward flow velocity profile shape was flattened at higher positions in the receiver. At the position of Y=550mm, air velocity was constant over the entire cross section of the receiver due to the decrease in the turbulence at upper section of the receiver. At higher positions, where the fluid reached the conical section, air flow accelerated as expected. As a result, air velocity increased at the conical part of the cavity (see Figure 5.7 at Z=±30). Consequently, the cone pushes air flow down through the centre of the receiver. Figure 5.6 indicates that the suction velocity profiles were approximately uniform over the entire cross section of the duct. At the centre of the receiver, the effect of the wall and the tip effect of the fan did not affect flow velocity.

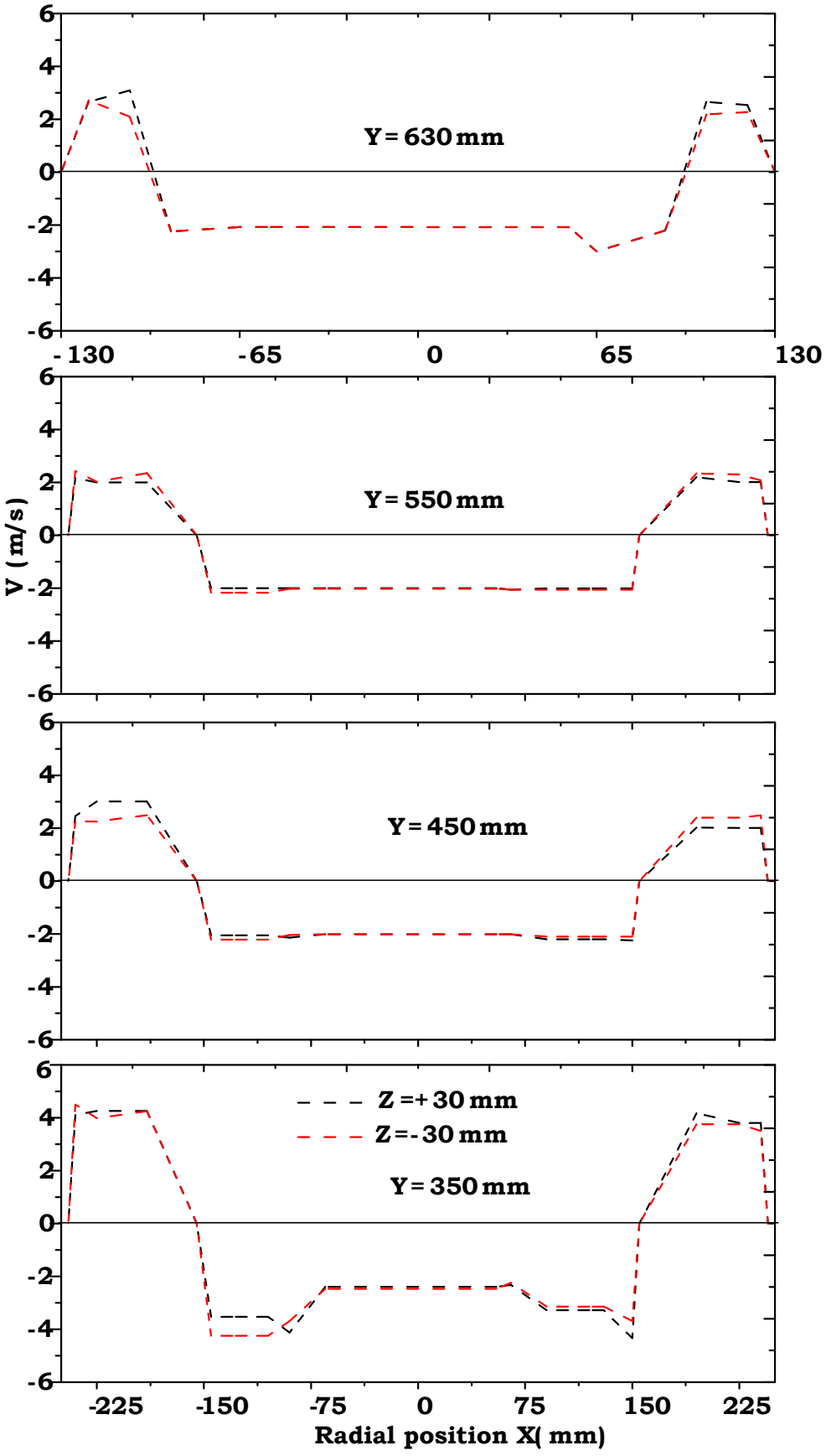

Figure 5.7 Variation of total flow velocity of air with the radial position along the X axis at Z=±30mm at RPM=1500.

The axial component velocity is shown in Figure 5.8. It was observed that the axial component followed a similar trend to the total velocity. The axial velocity was observed to be slightly less than the total velocity. It was also revealed that the tangential and redial component was very small

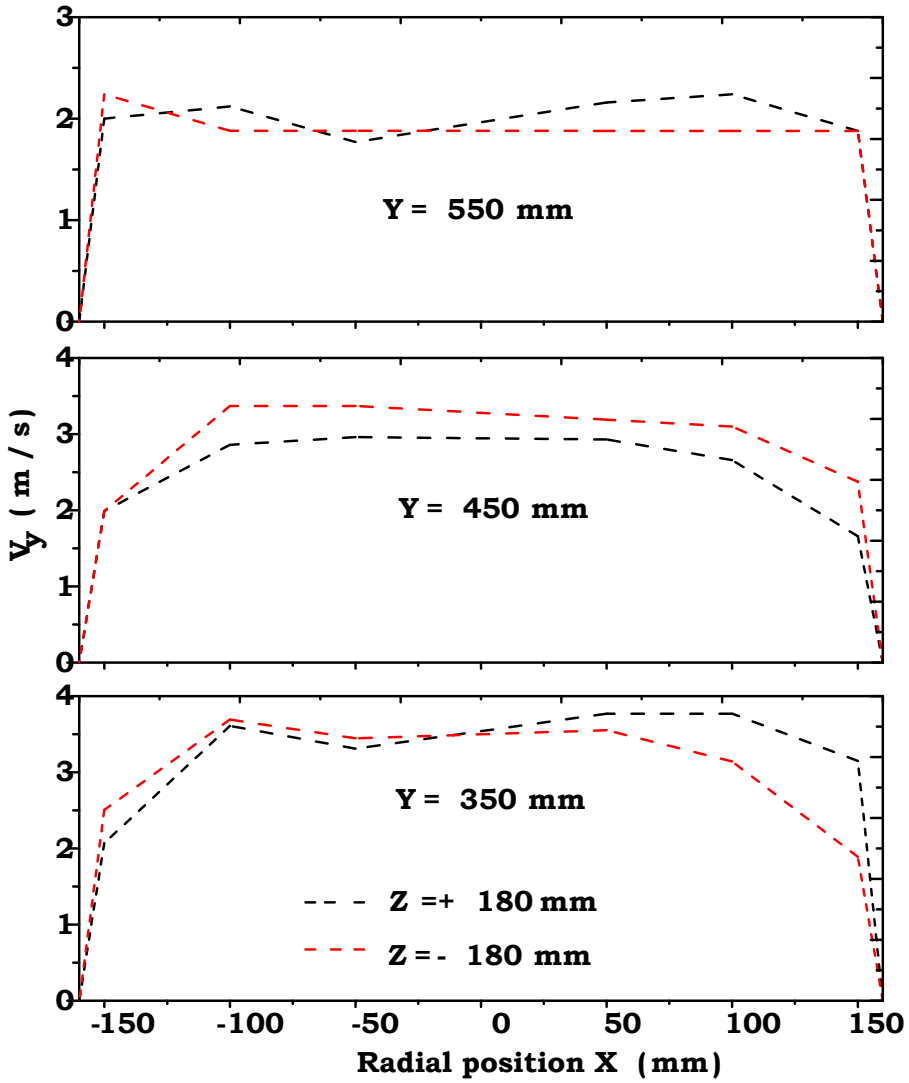

Figure 5.8 Variation of axial flow velocity of air with the radial position along the X axis at Z=±180mm at RPM 1500.

Receiver with particle stopper

The addition of a stopper improved the receiver performance, eliminating the particle deposition problem on the aperture window and increasing receiver thermal efficiency as explained later in the thermal performance investigation. Particle stopper was designed as conical shape with and inclination angle 45 degree to slide the air and

Due to space limitations, velocity measurement was only conducted at axial locations above the particle stopper, as shown in Figures 5.9 to 5.12. Velocity was measured at Y=350mm, and Z=±180mm, Z=±30mm at all points in the cross section of the receiver. The velocities were measured at different cross sectional positions . A comparitive study of total flow velocity and axial velocity at the position of Y=350mm, Z=±180mm and Z=±30mm, shows that the total uplift maximum velocity, V, reached 3.5m/s (Figure 5.11) and the axial velocity, V_y was 2.8m/s (Figure 5.11), at 500RPM fan speed. Total uplift velocity, V, was approximately 5m/s at Y=350mm, Z=±180mm and Z=±30mm (Figure 5.10) and the axial flow velocity, V_y, was 4.5m/s (Figure 5.10) for 800RPM. At every Y=350mm and Z=±180mm, velocity was in the upward direction, as was observed in the duct fan combination system.

Results revealed that most flow velocity was transformed to the axial component which assisted in lifting the particles. The fan generated strong suction and delivery pressure to recirculate the particles. Experimental results show that the tangential components of the flow velocity were less than ±1m/sec (Figure 5.12). Figure 5.9 (c) shows a non-symetrical velocity at Z=+180mm and Z=-180 at fan speed more than 1500RPM. The hanger position at Z=+180mm was acted as a guide vane and changed the swirl velocity.

Figure 5.12 shows the tangential and radial component of the velocity of air flowing in the cavity of the receiver. It is worth noting that even for higher rotational speeds of up to 1000RPM the tangential and radial components are small, with values slightly above ±1m/s .

Dimensionless velocity

To entrain the particles, air flow velocity must be equal to or higher than the particle terminal or settling velocity. To fluidize the particle air flow velocity must be higher than the minimum fluidization velocity of the particle. Therefore, the air flow velocity was compared with the terminal velocity and minimum fluidization velocity.

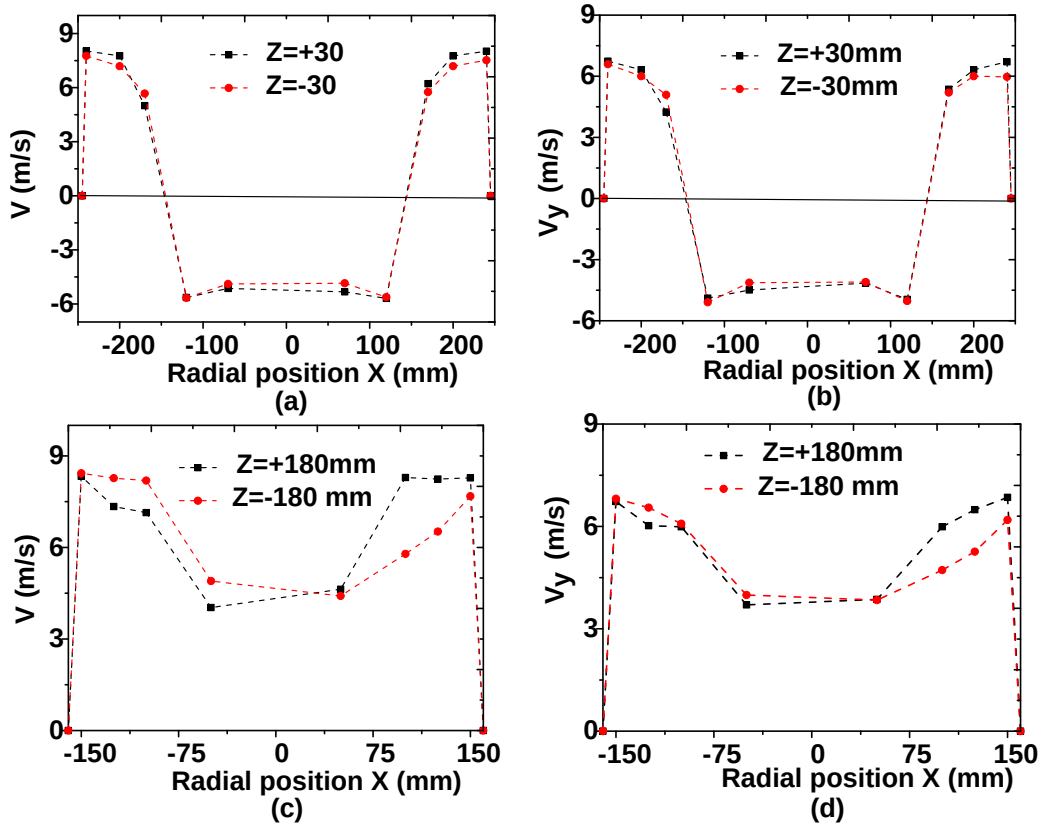

Figure 5.9 Variation of total flow velocity and axial flow velocity with the radial position along the X axis at Y=350mm (RPM=1500).

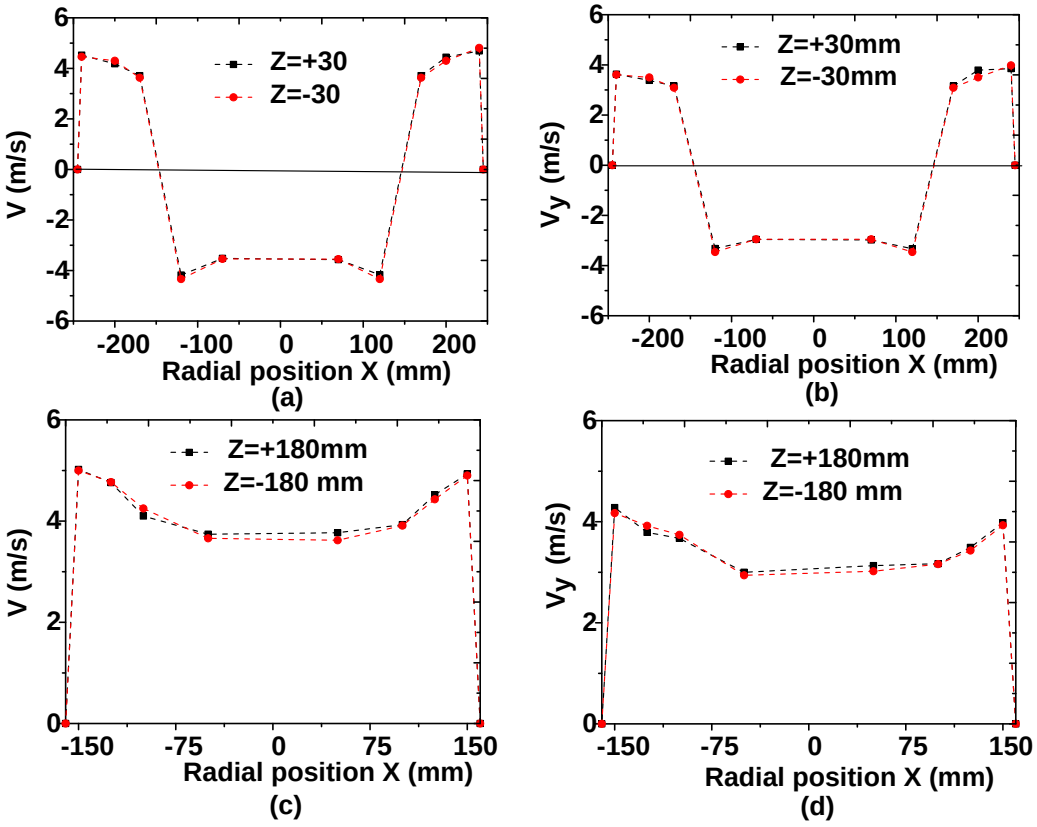

Figure 5.10 Variation of total flow velocity axial flow velocity with the radial position along the X axis at Y=350mm (RPM=800).

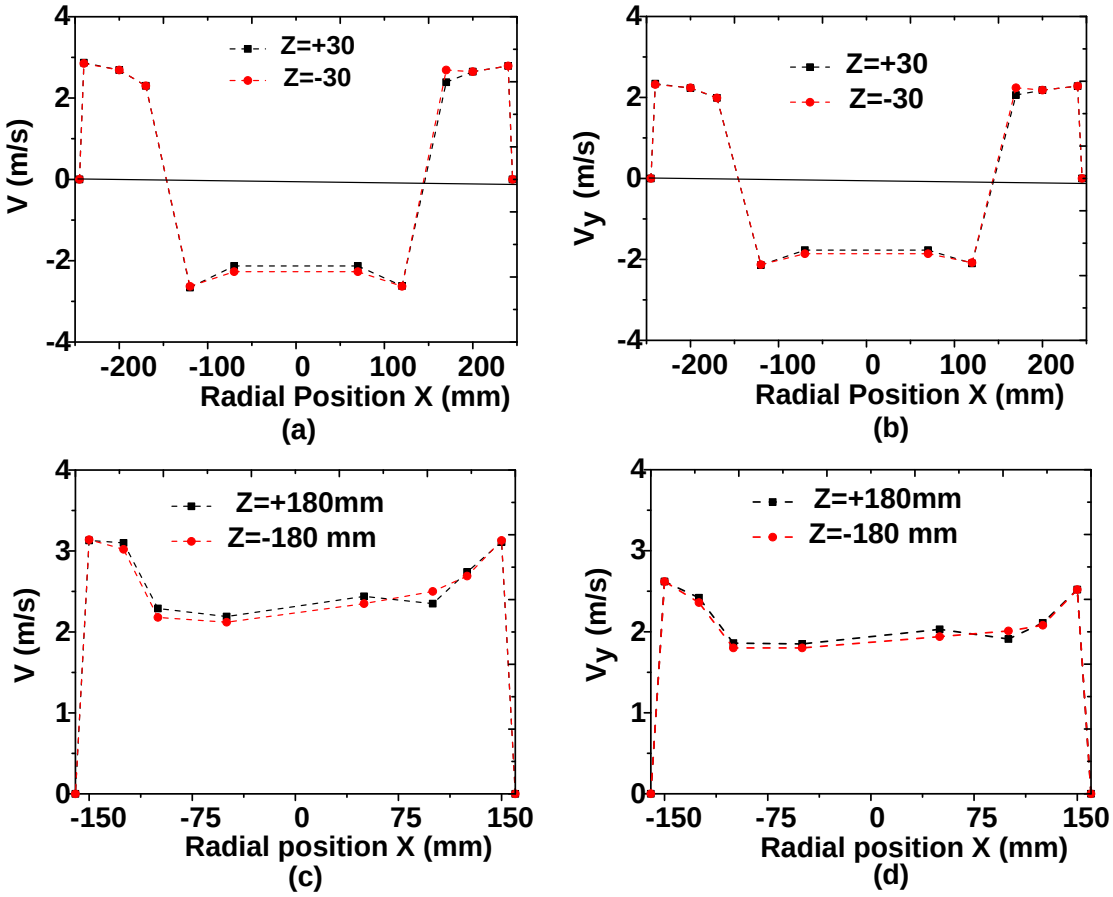

Figure 5.11 Variation of total flow velocity axial flow velocity with the radial position along the X axis at Y=350mm (RPM=500).

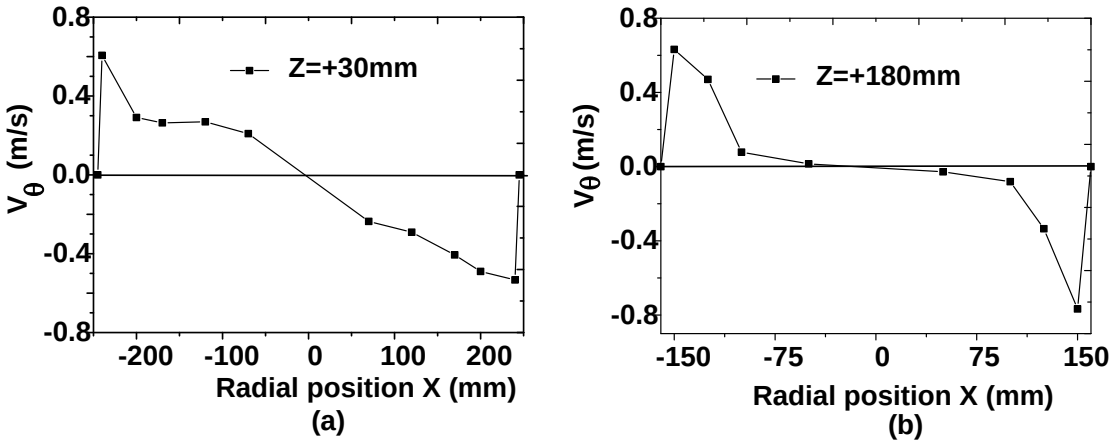

Figure 5.12 Variation of tangential velocity with the radial position along the X axis at (a) Z=+30mm and (b) Z=+180mm (RPM=800).

To better understand the required velocities that ensure particles are carried with the air flow, normalized terminal velocity, v_t^* and minimum fluidization velocity, v_{mf}^* were calculated. v_t^* is the ratio of air

flow velocity V and terminal velocity, v_t of the particle. The terminal velocity is expressed as:

$$v_t = \left[\frac{18}{(d_p^*)^2} + \frac{0.591}{(d_p^*)^{0.5}}\right]^{-1} \left[\frac{\mu(\rho_s - \rho_f)g}{\rho_f^2}\right]^{1/3} \quad (5.5)$$

Where, $d_p^* = d_p\left[\frac{\rho_g(\rho_s - \rho_g)g}{\mu^2}\right]^{1/3}$

The minimum fluidization velocity is expressed as:

$$v_{mf}^* = d_p^2\left[\frac{(\rho_p - \rho_f)g}{150\mu_f^2}\right] \quad (5.6)$$

Variation of the normalized dimensionless velocity along the radial distance of the receiver on an XZ plane is shown in Figure 5.13. Black silicon carbide particles 200microns in diameter were used in the experiment. These particles have a terminal velocity of 0.8m/s (equation 5.5) and a minimum fluidization velocity of 0.07m/s (equation 5.6). The total flow velocity was normalized using this terminal velocity and minimum fluidization velocity of the particle. It was observed that the average normalized turbulent velocity more than 3 (Figure 5.13). Therefore, the obtained flow velocity was capable of carrying the particles upwards between the outer boundary of the duct and the inner cavity wall of the receiver and then sucking particles downwards through the duct even at a rotational speed lower than 500RPM. Particles carrying capability was exist to the height where air velocity was more than 0.8m/s.

Increased turbulence can improve the mixing of air and particles and enhance heat transfer. Turbulence intensity reflects the inter-particles collisions and wall to particle collisions in a two phase flow. Turbulence intensity (TI) in the axial direction can be estimated from the ratio V_{rms}/V. Here, V_{rms} is the fluctuating component of air velocity in the vertical direction. The turbulence intensity variation along the radial

direction of the cavity, V_{rms}/V, was plotted along the radial position at Z=+180 for different axial locations (in the Y direction) in the cavity (see Figure 5.14 to 5.16).

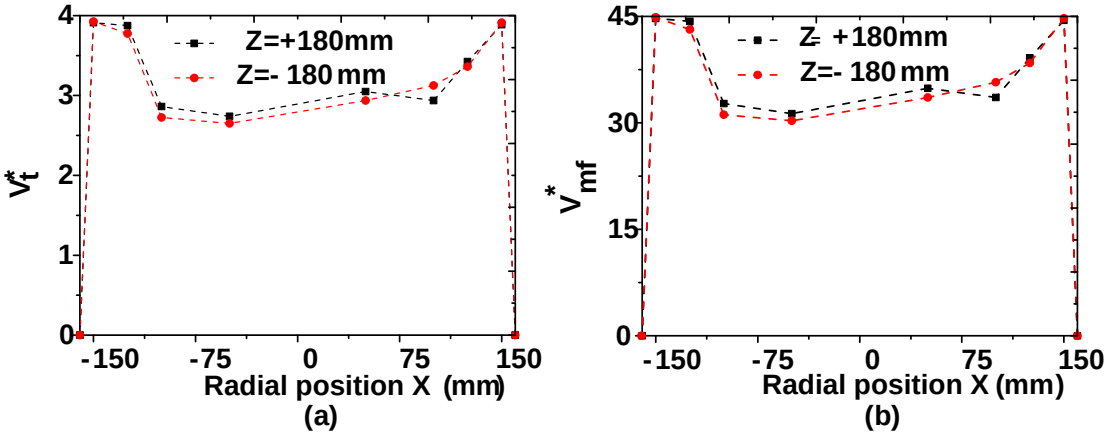

Figure 5.13 Variation of normalized (a) terminal velocity (b) minimum fluidization velocity with the radial position along the X axis at Z=±180mm , RPM=500.

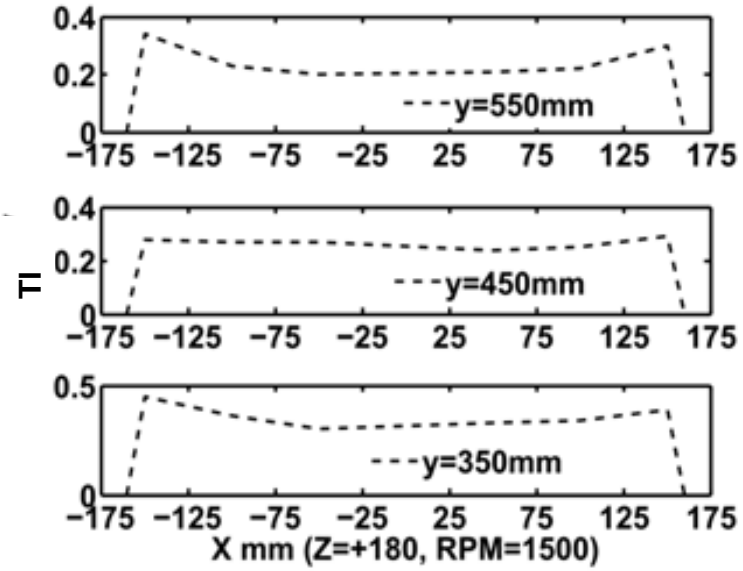

Figure 5.14 Variations of turbulence intensity with the radial position along the X axis at Z=+180 mm at 1500RPM.

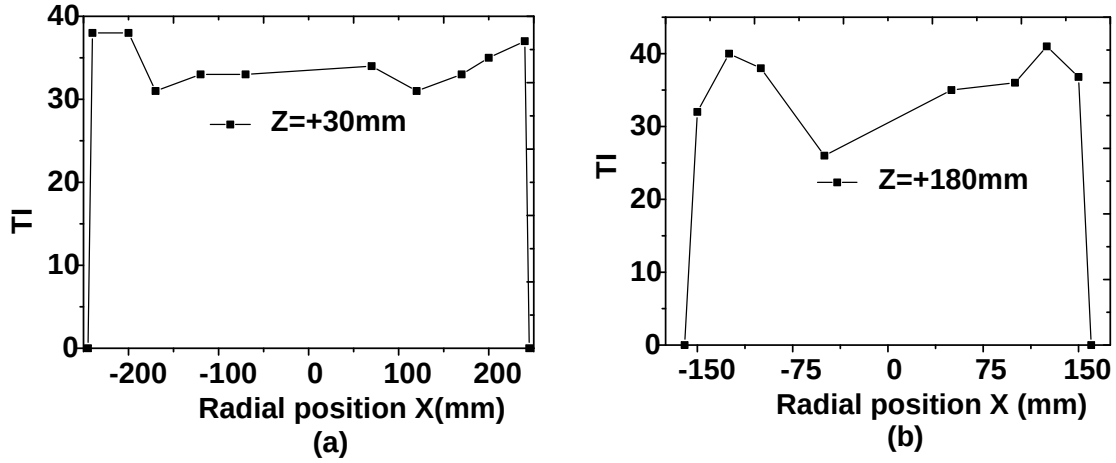

Figure 5.15 Variation of turbulence intensity with the radial position along the X axis at 800RPM.

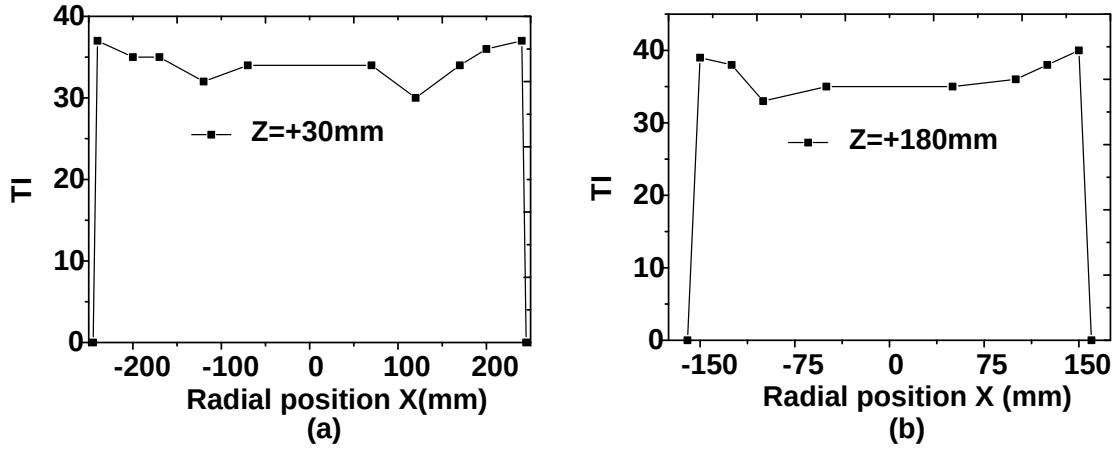

Figure 5.16 Variations in turbulence intensity with the radial position along the X axis at 500RPM.

Figure 5.14 presents the profile of the turbulence intensity at 1500RPM. The turbulence intensity value was 20% near the central region and 45% near the cavity wall at 1500RPM. High axial velocity near the wall, due to the blade tip and rotation of flow velocity, increased the turbulence intensity at this location. In addition, it is postulated that wall roughness has also played a role in increasing the velocity fluctuation near the wall. This variation of intensity along the radial direction in the cavity shows that particle-to-wall collision is higher near the wall as compared with particle-to-particle collision in the central region. Figure 5.14 also shows that the average velocity fluctuation was 45% at Y=350mm, 30% at Y=450mm and 20% at

Y=550mm. The variation of turbulence intensity along the vertical height, Y, indicates that collisions between particles decreased with the increasing free board height, Y, at a constant fan RPM.

Figures 5.15 and 5.16 show the turbulence intensity at 800RPM and 500RPM for the height of Y=350mm. Figures 5.15a and 5.15b showed that the average turbulence intensity was 35% at 500RPM. Whereas, Figures 5.16a and 5.16b showed that the average turbulence intensity was 40% at 800RPM. The trend of the results showed that both turbulence intensity and superficial velocity was increased with the increase of RPM. Hence, an increase in the turbulence intensity increases the momentum transfer in the dispersed medium which in turn can improve the heat transfer between the particles and air.

5.3 Particle concentration measurement

5.3.1 Experimental procedure

The objective of the particle concentration experiment was to quantify local particle concentration at different freeboard heights of the solar receiver, with varying rotational speeds of the operating fan. The experimental apparatus is shown in Figure 5.17.

A calibration cell (an acrylic pipe) of 100mm diameter and 500mm length, which has a similar optical length to the solid particle solar receiver, was used to quantify the extinction coefficient for different concentration solutions of water-particle mixtures. The pipe was filled with water and a known concentration of SiC particles. The mixture was shaken well before calibration in order to ensure homogeneity. It was noted that SiC particles were suspended in the medium of air in the actual solar receiver. However, in this experiment water was used because it allowed particles to be suspended homogenously long enough for the measurements to be conducted in the test cell.

During the test, the calibration cell was positioned horizontally in the pathway of the laser beam, as shown in Figure 4.6 (Section 4.5.1). After turning on the 5mW He-Ne laser, the light beam was passed through

(i) the test pipe filled with atmospheric air,

(ii) the test pipe filled with water only, and

(iii) test pipe filled with water and a known concentration of SiC particles and

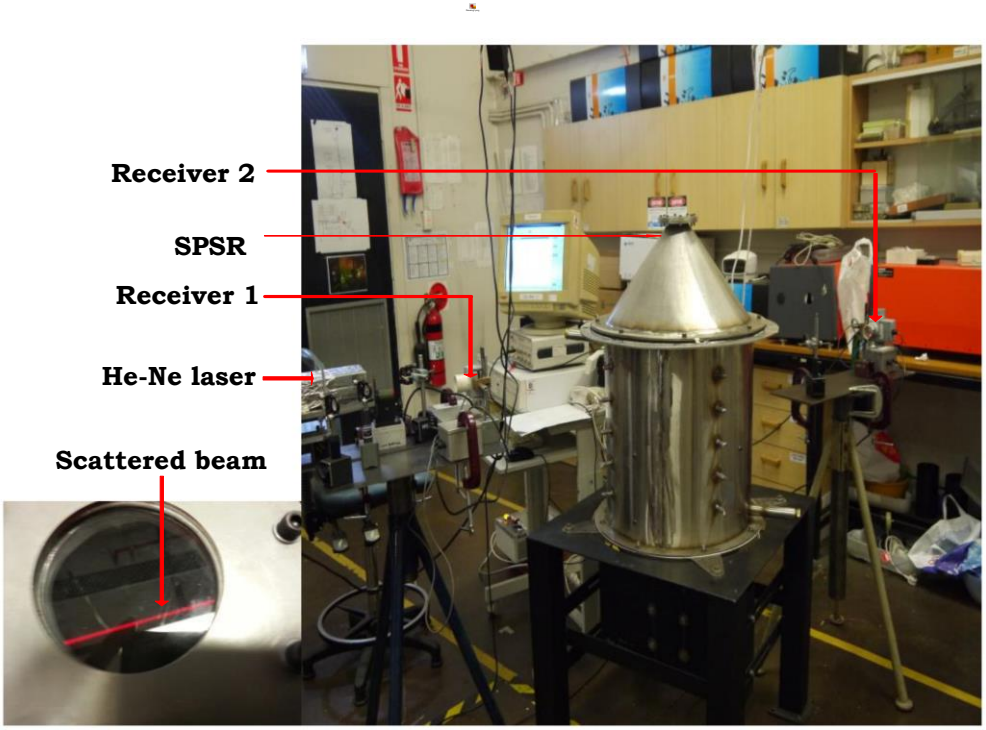

Figure 5.17 Schematic and photograph of the particle concentration measurement experimental setup (schematic shown in Figure 4.7).

The extinction coefficients obtained from the above three tests were used to calculate the extinction coefficient under homogenous air with a particle medium. Then, a calibration curve of the extinction coefficient for a known concentration of particles in the system was plotted. During the particle concentration measurement test in the solar receiver, a specific amount of SiC particles of uniform size were added to the bottom hemisphere of the receiver. Then, the fan was turned on at a specific speed and the He-Ne laser was switched on. A laser beam was passed through the particle cloud inside the receiver and the scattered signal from the opposite side of the receiver was measured.

The intensity of measured signal changed when the concentration of the recirculating particles varied. At high fan speeds, the particle cloud

was in such a dense phase that it absorbed all of incident and the output signal became zero. This test produced particle extinction coefficients with respect to specific fan RPM, whereas the calibration test provided extinction coefficients at a specific particle concentration per litre of fluid. Therefore, comparison of these results provided particle concentrations in the receiver at specific rotational speeds of the fan.

5.3.2 Measurement uncerainities

The measured sources of error in this experiment were the inherent accuracy of collected data, laser vibration, photodiodes alignment and accuracy of the photodiode data. From the measured value of particle concentration, the random error of the measured data calculated by Equation (5.2) was 0.013%. Position alignment of the photodiode was fixed using the mechanical spirit level test. The estimated error associated with this type of misalignment was estimated to be less than 5%. Accuracy of the photodiode was ±5% within the measured range. Hence, the combined uncertainty calculated by Equation (5.4) was 5.8%.

5.3.3 Results and discussion

The measured attenuation of light was linearly dependent on the particle concentration and particle size. As the number of suspended particles in the solution increased, the attenuation coefficient for both 70micron and 200micron particles increased (Figure 5.18). Furthermore, Figure 5.18 shows that the attenuation coefficient for 70micron particles is higher than for the 200micron size particles. In order to compare the measured results, the attenuation coefficient was calculated analytically using the relationship developed by Baker et al. [105]. The theoretical results also supported the theory of linear dependency of the attenuation coefficient with particle concentration. The deviations of experimental and theoretical results were higher for 200 micron compared to 70 micron. It was postulated that 70 micron

particle was mixed more homogeneously compared to 200 micron and so more discrepancy was observed for 200 micron particle.

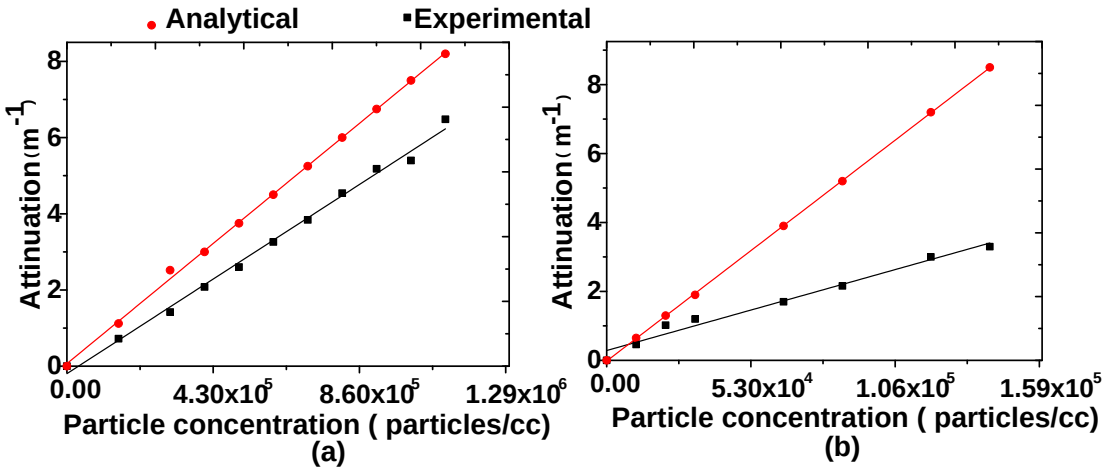

Figure 5.18 Calibration curve for (a) 70 micron and (b) 200micron particles.

In this experiment, particle concentration was measured in the cavity receiver for 70 and 200micron SiC particles. Results from these measurements were used to optimize the rotational speed of the fan and free board height. Figure 5.19 shows the measured particle concentrations under different rotational speeds of the fan for both particle sizes. Particle concentration was measured at different heights in the volume by passing the He-Ne laser beam through the 6mm hole of the cavity receiver. During particle concentration measurement, it was assumed that the particles were uniformly suspended throughout the cavity. However, this assumption may not be accurate at all positions within the receiver. Nonetheless, the mean values measured are indicative of the relative concentration at different heights.

The suspension density of solids within the gas flow stream was referred to as the particle concentration and was denoted as M in particles/m^3. The measured particle concentration at Y=430mm, at a speed of 1000RPM, was $2.75x10^9$ particles/m^3 for 70microns and $5x10^7$ particles/m^3 for 200microns (Figure 5.19a).

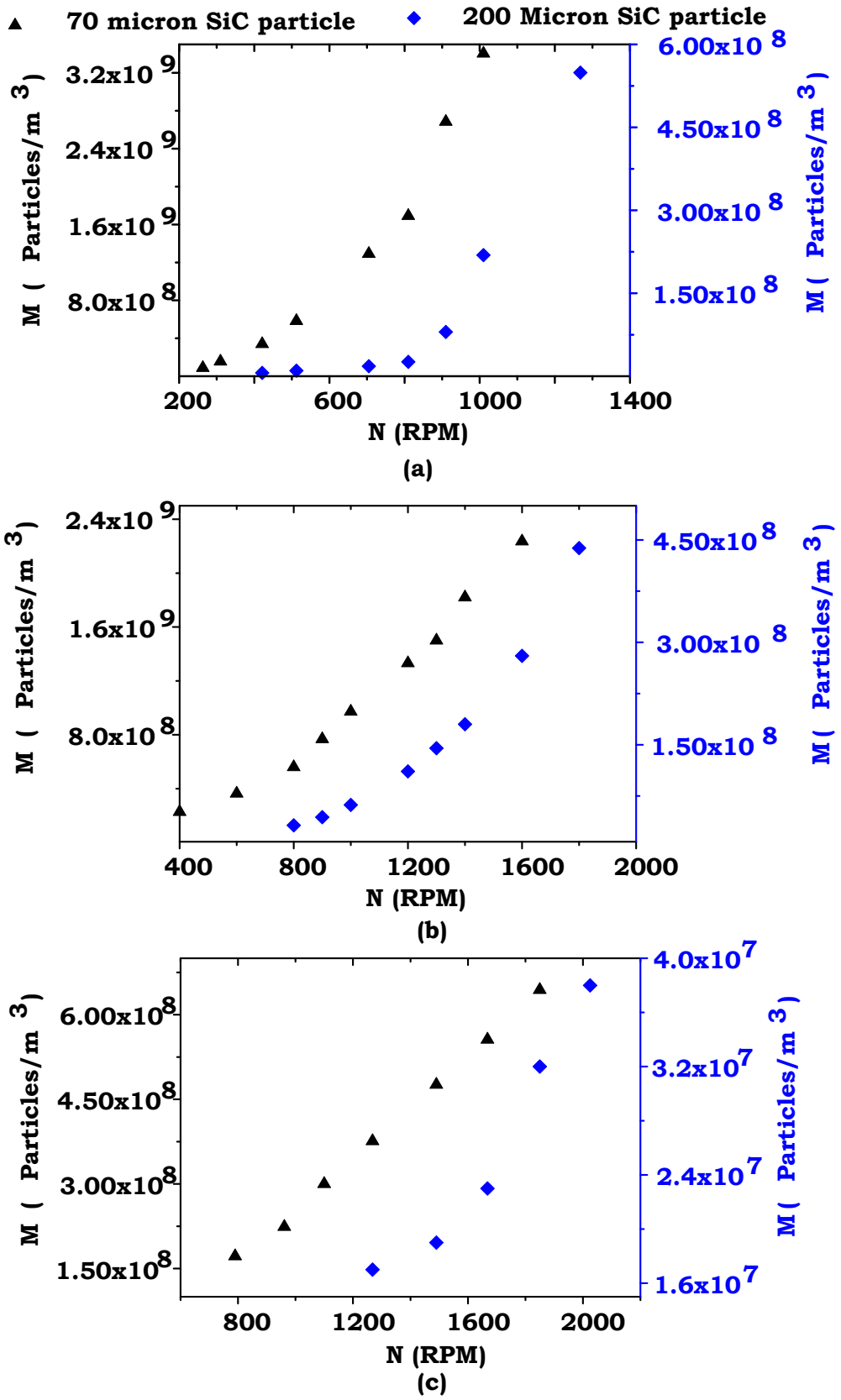

Figure 5.19 Measured particle concentration for 70 and 200micron SiC particles at different fan speed and at a free board height of (a) Y=430mm, (b) Y=590mm, and (c) Y=840mm.

Consequently, the results show that the particle concentration increased exponentially by increasing the fan rotational speed for both sizes of particles (see Figures 5.19 a, b and c). Particle recirculation increased with increasing the rotational speed of the fan, therefore the resultant particle carryover was increased.

Particle concentration at different heights within the receiver differed with the rotational fan speed for both sizes of particles. Particle concentration was lower for 200micron sized particles than for 70micron particles at a the same fan speed and at the same free board height of the receiver (Figure 5.19). The experimental results also show that the 70micron sized particles appeared at the Y=430mm location at a minimum fan speed of 200RPM and had greater particle density at a specific speed when compared with larger sized particles. For a 0.022% volume particle fraction, the measured particle concentration revealed that particle forced recirculation depends on the characteristics of the recirculating air inside the receiver and particle size.

As previously discussed, velocity measurement analysis showed that air velocity close to the wall was higher than at the central region of the cavity. Hence, it was predicted that a cluster formed near the wall region and the cluster concentraton was lower away from the wall. Furthermore, turbulence was higher near the wall at higher fan speeds (as observed in the turbulence measurements, see Figure 5.16). Therefore, increasing turbulence near the cavity wall increased air-particle interaction. As the local heat transfer coefficient varies according to the suspension density of the carrying solids [48], an increase of heat energy transfer to air was expected, when considering the current particle flow characteristics of the receiver.

Particle concentration variation was plotted at different heights within the receiver at a constant fan speed for different sized particles, as shown in Figures 5.20 and 5.21. Figure 5.21 shows that at Y/H=0.5 the particle concentration was 3×10^9 particles/m^3 for 70micron particles, whereas, at the same position, the particle concentration of 5×10^7 particles/m^3 was measured for 200micron particles. The trend

shown in Figure 5.21 indicates that the number of suspended particles is higher at the same position for 70micron size particles as compared to with 200micron size particles. Figure 5.21 also shows that particle concentration was 3×10^9 particles/m^3 at Y/H=0.5 and 1.2×10^9 particles/m^3 at Y/H=0.65, at constant speed. This trend in the results shows that particle concentration decreased with the increasing free board height at the same rotational speed of the fan.

Particle concentration in the free board region is an important factor in particle absorption of incoming irradiation. The higher the concentration of particles, the greater the ability to absorb energy. For further clarity, the opacity of the particle cloud in the cavity was presented for different measurement positions and operating conditions. Figure 5.22a shows changes in opacity of the particle cloud with differing rotational speed of the fan. The opacity of the particles determines the particle local cloud density which was calculted by the modified Equation of Bougures Law, given as Equation (5.7).

$$\text{Opacity} = 1-\frac{I}{I_o}=1-e^{\frac{3fw}{d_p}} \qquad (5.7)$$

Opacity depends on the particle volume fraction, f, cloud concetration, w, and particle diameter, d_p. Opacity was 0.2 at 500RPM for 70micron particle, while 0.2 opacity was obtained at 1100RPM for 200micron particles (Figure 5.22a). Results show that opacity increases when using smaller particles at a certain fan speed, indicating that a uniform opaque cloud of suspended particles may produce higher energy absorption in the cavity. Opacity increased approximately exponentially with the increased fan speed for different sizes particles (Figure 5.22) which is not surprising given that opacity is a function of paricle concentration. Hence, to achieve uniform opaque particle concentration in the cavity, fan speed can be used as an operating parameter to control opacity at a constant volume fraction of particles. Figure 5.22b shows the change in particle cloud opacity with the change in the

dimensionless height of the receiver. In this case, the fan speed was kept constant at 1260RPM and calculated opacity was found to be 0.55 for 70micron particles and 0.20 for 200micron size particles, measured at Y/H=0.95.

The opacity of the particle cloud at Y/H=0.65 was 0.95 for 70micron particles and 0.8 for 200micron particles, as shown in Figure 5.22b. The trend of the results shown in Figure 5.22b indicates that opacity was dependent on particle size, dimensionless free board height and fan speed. Opacity of the particle cloud decreased at higher measurement positions in the receiver due to a reduction in superficial velocity in the upper region of the receiver (Figures 5.6 and 5.7). At Y=840mm, opacity was 0.5 for 1000 RPM (Figure 5.21). This trend indicated that 50% of particles was returned towards downward of the cavity before reaching the Y=840mm location of the receiver.

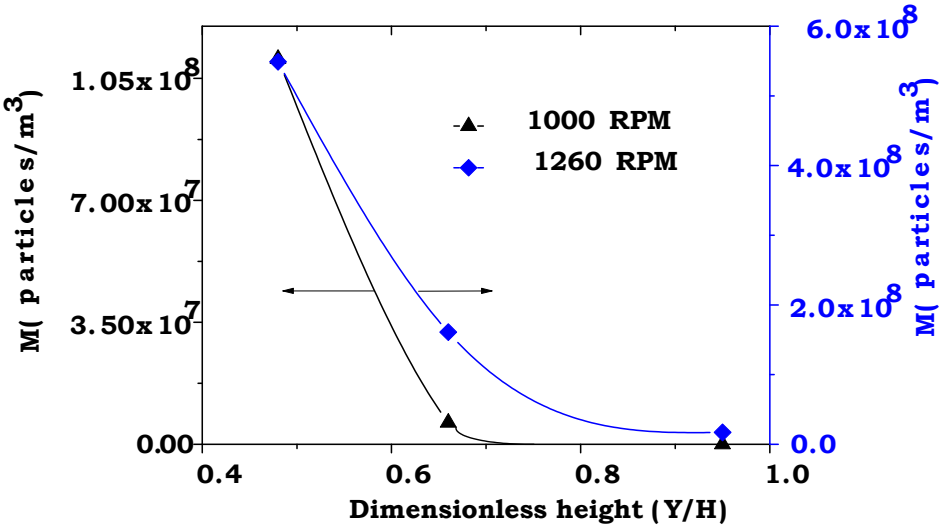

Figure 5.20 Measured particle concentration for 200micron SiC particles at different fan speed and at different dimensionless heights.

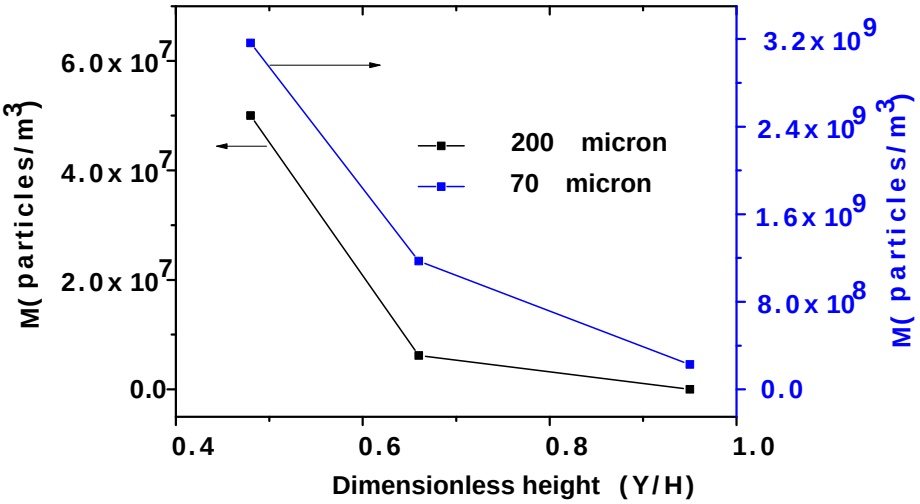

Figure5.21 Measured particle concentration for 200micron SiC particle at different dimensionless height and at a speed 1000RPM.

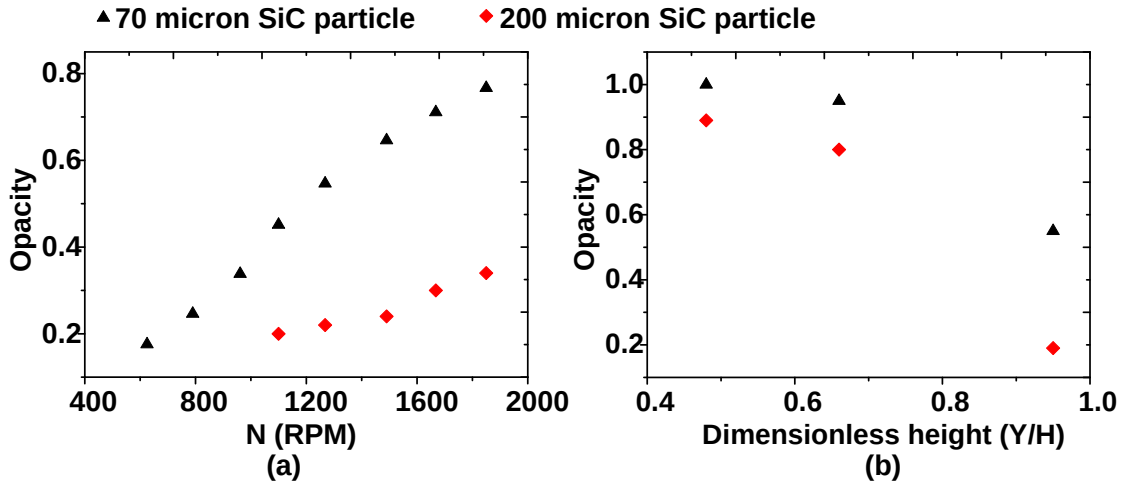

Figure 5.22 Variation of opacity with changing (a) fan speed at Y=840mm and (b) dimensionless height at 1260RPM.

The calculated Reynolds number, based on the receiver diameter, was above 10^5, and the particle volume fraction was less than 10%, i.e. a dilute flow. Therefore, the flow and mixing of air and particles is expected to be a turbulent interaction. Particle motion with the fluid stream was identified by investigating Stokes number values. A dimensionless parameter that measured turbulence intensity between the fluid and particle flow dynamics is governed by the Stokes number which is defined as:

$$St = \left(\frac{\rho_p d_p^2}{18\mu_f}\right) \Big/ \left(\frac{D}{v_f}\right) = \frac{\tau_p}{\tau_f} . \qquad (5.8)$$

Here, D is the characteristic length and v_f is the averaged flow velocity, ρ_p is particle density, and d_p is particle diameter. The Stokes number is an indicator of the relationship between the path of a particular particle and the flow that is carrying it within the receiver. The flow of particles and air is characterized as a dilute phase particle flow when the particle volume fraction $<<1$. In this analysis, the receiver diameter was taken as the characteristic's length.

Figure 5.23 shows Stokes number variations in a radial direction of the solar receiver at Z=±180mm, Y=350mm for 200micron particles at different rotational speeds. The maximum Stokes number for 500RPM was 4, whereas it was 6.5 at RPM=800 for 200micron particles. It is well established that if St>5 then the flow is partially inertia dominated. Therefore, the calculated Stokes number at Z=±180mm, Y=350mm indicates that larger particles do not follow the fluid stream. The fluctuating particle velocity is much higher for higher rotational speeds, as a result, more interactions are expected for RPM=800 than for RPM=500. The Stokes number was 0.8 at 800RPM and 0.5 at 500RPM for 70micron particles. According to the Stokes number variation; 70micron particles are more likely to follow the fluid stream.

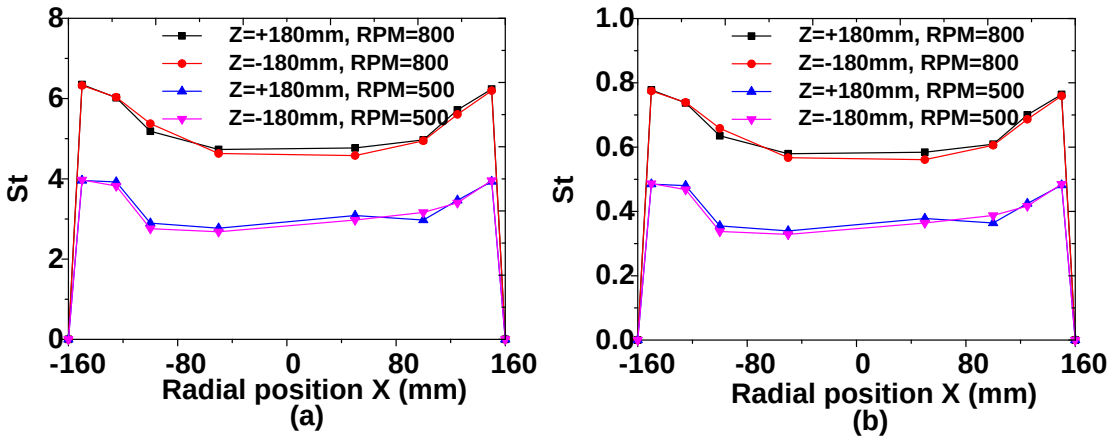

Figure 5.23 Variation of the Stokes numbers with the radial position of the solar receiver for (a) 200 and (b) 70microns SiC.

5.3.4 Discussion on key findings

The current receiver was designed as a cavity type solar receiver with a ducted fan generates the required forced recirculation effect. Figures 5.6 to 5.12, demonstrated the recirculating flow pattern in the designed receiver. Measured velocities in the experimental analysis showed that the flow was recirculated from the bottom to the top of the cavity as shown in Figure 5.24a and 5.9. A comparison between the flow pattern in the current solar receiver and that for a solar receiver without a forced recirculation system is shown in Figure 5.24b. It is shown that a sufficient flow rate of air is required to suspend particles in the free board region in of a cavity type solar receiver with natural flow. However, due to the absence of natural recirculation, the residence time of fluid and solid mixture is not high enough which results in a reduction in receiver efficiency.

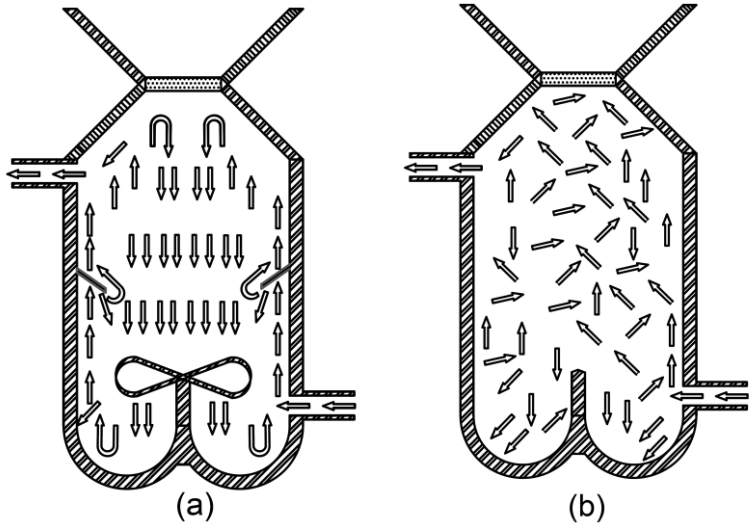

Figure 5.24 Schematic of flow pattern (a) current recirculating flow solid particle solar receiver with fan (b) solar receiver without fan

The addition of a ducted fan arrangement to the solar receiver results in higher residence time of HTM increasing the working fluid temperature through enhanced convective heat transfer which was discussed in the chapter 6. To discuss residence time more quantitatively, the following relationship of contact residence time of the particle developed by Basu et al. [106] is used:

$$t_c = \frac{\rho_m D}{[\rho_p (1-\alpha_p) U_p W^2]^{1/3}} \quad (5.9)$$

Here, U_p is the particle velocity, W is the forced recirculation rate of particles, D is the receiver diameter, t_c is the contact residence time of particle to the wall. Equation (5.9) shows that a higher recirculation rate decreases contact residence time. In the current solar receiver, the air particle mixture forced recirculation rate increased with increasing the fan speed. In addition, fan speed influences the number of recirculation cycles before the hot air leaves the receiver outlet. In this stand-alone receiver, in which the residence time of the particles is infinite and the residence time of air is controlled by varying fan speed, it is difficult to measure the forced recirculation cycle while increasing the fan speed. As mentioned earlier, forced recirculation of air and particles is controlled using the excess air in the conventional cavity type reactor. This excess air is a parameter that can act to reduce cavity temperature. Therefore, the infinite residence time of particles and the increase of residence time of air coupled with an increase a forced recirculation cycle is an advantage to increase thermal efficiency of this receiver.

In the flow measurement test, the tangential velocity component was measured and found to be less than 1m/s (Figure 5.12) at 500RPM. Such low velocities indicate that the transverse movement of the particle is very limited in this receiver under the operating conditions. The axial flow component at 500RPM was 2.8m/s at Y=350mm (Figure 5.11). These velocities indicate that the air and particles mixture movement was mostly in the axial direction vertically upward and downward. Hence, a well interaction among the air, particles and wall is expected as a result of higher axial component and an increase of heat transfer efficiency is anticipated.

Figure 5.25a shows that the effect of the cavity Reynolds number and turbulence intensity with the fan speed. It was observed that both the turbulent intensity and cavity Reynolds number were increased with the increasing the fan speed. Figure 5.25b shows that the Stokes

number was approximately 5 for the cavity Reynolds number of 1.1×10^5. In addition, particle concentration increased with an increase in the cavity Reynolds number. These results show that the Stokes number, Reynolds number and turbulence intensity was changed with changing the fan's speed, rather than changing due to the air flow rate into the cavity.

An efficient solid particle solar receiver is required to maintain a uniform opacity to absorb the maximum incoming solar irradiation. In the current receiver decay of opacity was exponential (Figure 5.22) with increasing dimensionless height, due to the decreasing particle concentration (Figure 5.21). As a result, it was postulated that the increased penetration of the solar irradiation resulted in decreased re-radiation losses and increased absorption efficiency**.** It was shown that using the condition of particles carryover which depends on the particles terminal velocity and particles fluidization velocity an appropriate fan speed can be selected. Optimum speed of fan was chosen based on the condition that the speed at which no particles was reached the inner surface of the quartz window. According to Figure 5.2 (c), the speed at which the normalized velocity V_t^* =1 (below the quartz window) can be selected as the optimum speed to recirculate the particles. Comparing the Equation 5.5 and the condition discussed above, the relation between the particle size and optimum speed can be found.

Particle size selection was based on the following criteria (i) agglomeration properties of different size particle. Particles with the diameters of less than 30micron were agglomerated on the inner cavity wall; (ii) Dependency of the particle and air interaction was depended on higher stokes number. It was observed that for a similar fan speed 200 micron particles had higher stokes number than 70 micron particles; (iii) Companion between the particles terminal velocity, fluidization velocity and superficial velocity.

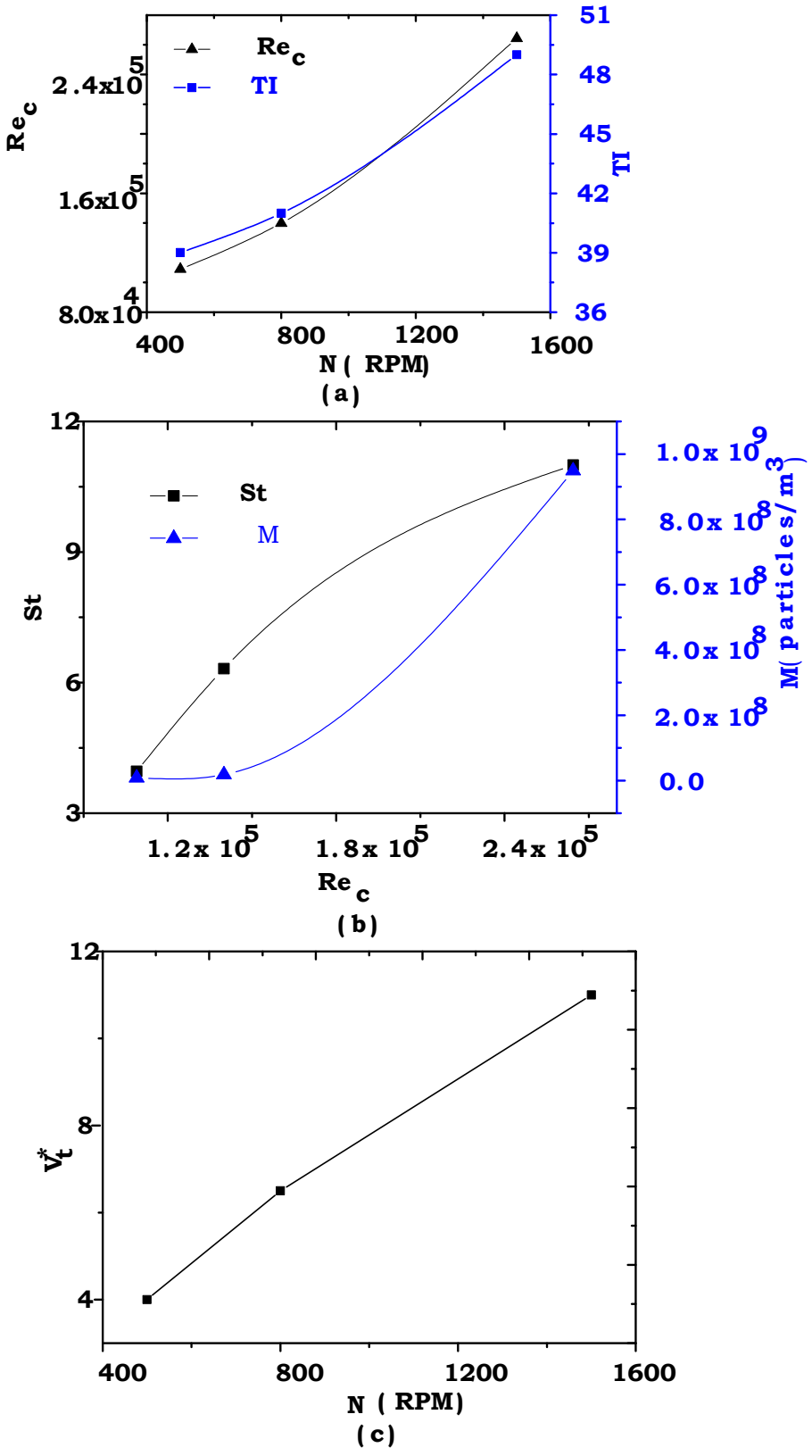

Figure 5.25 (a) Effect of RPM on the cavity Reynolds number and turbulence intensity (b) Variation of Stokes number and particle concentration with the change of Reynolds number (c) Variation of normalized flow velocity with the rotational speed of the fan.

Chapter 6
Thermal behaviour analysis

6.1 Introduction

Thermal performance and efficiency of the developed solar receiver were tested experimentally. The results of these experiments and the analyses of the data are presented in this chapter. Analyses were performed using two steps:

(i) characterization of solar simulator irradiation intensity and measurement of input heat flux into the cavity, and

(ii) measurement of outlet air temperature under different operating conditions.

Data were used to correlate the outlet air temperature variation with the operating conditions, thermal efficiency and power generation. The analyses consider the effect of the forced recirculation rate, mass flow rate of air, particle type and size and free board height of particles.

6.2 Heat flux measurement procedure

Heat flux from the solar simulator Xenon arc lamp radiation was measured in order to determine the net heat input into the receiver and the transmission factor of the quartz glass installed at the aperture. Measurements were conducted with and without quartz glass at the receiver aperture. To measure the heat flux and air temperature, the reflector and aperture of the receiver were located at specific positions as shown in Figure 6.1.

The mirror and top conical section of receiver were kept at the same position during the air temperature measurement experiments. A

schematic of the mirror position, aperture position and the measurement locations with relevant dimensions is shown in Figure 6.1.Measurements were taken at different locations within the receiver for the case of no quartz window and with quartz window (Figure 6.1). Heat flux was determined at the aperture. The theoretical value at the aperture location was approximately 100sun (1sun=1kW/m^2) and the heat flux transducer's maximum nominal value was 11suns. Therefore, the heat flux transducer was placed beyond 750mm (a safe distance from the focal point according to the nominal value of the heat flux sensor) to measure the heat flux at a different locations. The corresponding safe distances from the mirror were S_1, S_2, S_3 and S_4. The averaged heat flux value at different locations was used to calculate the transmission factor of the quartz window and heat flux at the aperture position. For each axial position, the heat flux transducer was traversed on a grid pattern with 50mm interval in both x and z directions, as shown in Figure 6.2.

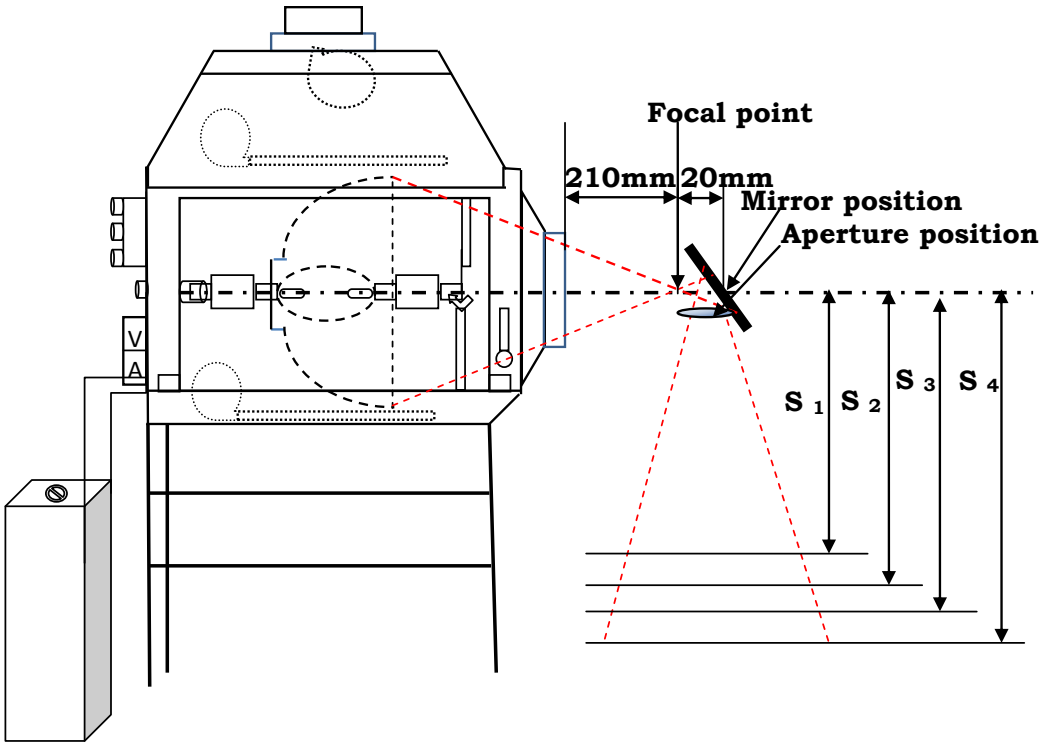

Figure 6.1 Heat flux measurement setup with the location of measurements. S_1=900mm, S_2=1000mm, S_3=1100mm and S_4=1200mm.

Heat flux was measured across 8 × 8 grid locations. The different symbol colours of Figure 6.2 indicate the variation of heat flux at different locations. For each location, data were collected at a rate of 2Hz over a measured time of 40 seconds and 10 measurements were taken for every point. Amplified data were scanned by a data logger and processed by screen recording software installed in the CPU. Then, the display unit displays the real time data as a *.txt file which was converted to an Excel file for analysis. Measured Voltage was then converted to heat flux using the amplified value of the Voltage and the 11kW/m^2 flux limit equivalent Voltage.

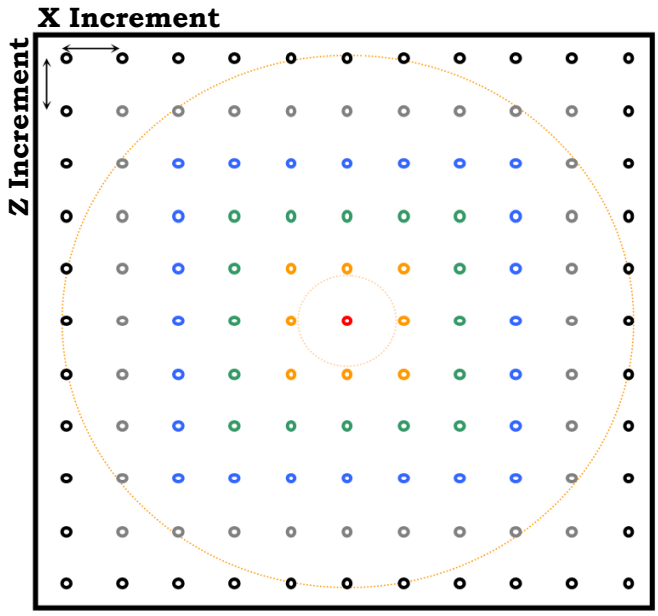

Figure 6.2 Heat flux measurement grid points location on XZ plane.

6.2.1 Measurement uncerainities

During heat flux measurement, sources of errors were the accuracy of the transducer, and any positional error of the sensor. The potential errors associated with the transducer measurements are as follows [107]: (i) Accuracy: ± 3% for most ranges; (ii) Maximum non-linearity: ± 2% for most ranges; (iii) Repeatability: ±0.5%.

A potential source of error during heat flux measurement was the transducer sensor positioning in the X, Y and Z directions. A 64 x 64 grid of 50mm^2 steel wire mesh was used to position the transducer on the XZ plane. Therefore, in the X and Z direction, the uncertainty of the

transducer position was estimated at a maximum of ±0.5mm. Here, XZ is the horizontal plane parallel to the ground and perpendicular to the incident beam. The vertical optical path length could vary according to alterations in Y direction and the intensity of irradiation changes with variations in the vertical optical path length. Therefore, the uncertainty of determining the distance in Y direction was less than ±5mm. The random error calculated from the experimental data was 0.25%. Hence, a maximum of 3.61% inaccuracy was found accounting for all sources of measurement error.

6.2.2 Results and discussion

Experiments were conducted under the following conditions:

(i) measurement of the heat flux at different positions, as shown in Figure 6.1, with a quartz window at the aperture, and

(ii) measurement of the heat flux at different positions, as shown in Figure 6.1, without a quartz window at the aperture.

The measured vertical distance below the mirror was S_1=900mm, S_2=1000mm, S_3=1100mm and S_4=1200mm from the middle point of the 45^0 inclined aluminium mirror. The Irradiation from the lamp at each point was calculated using a method described in reference [108]. The Xenon arc lamp was operated by an electrical current of 140 Amp and 35 Volts. The experimental results are shown in Figures 6.3 and 6.4.

The results show that heat flux distribution intensity decreases with the increasing vertical distance of Y and that flux distribution is approximately uniform (Figures 6.3 and 6.4). A shadow was observed in the centre of the illumination spot which increased in size with the increasing Y distance. Comparison of the heat flux profiles (Figures 6.3 and 6.4) determined that the diameter of the heat flux illumination spot increased with the increasing distance of the illumination point from the focal point. As expected, higher heat flux intensity was observed as the distance reduced along the focal point. Illumination spot intensity reduced when glass was placed on the aperture of the cone section of

the solar receiver due to the re-radiation of the quartz glass. Maximum heat flux was observed at X=0mm, Z=-100mm. Table 6.1 summarizes the maximum heat flux points at different Y locations for the case with and the case without glass at the aperture. Results show that approximately 21% less radiation enters the receiver when the quartz glass is placed at the aperture.

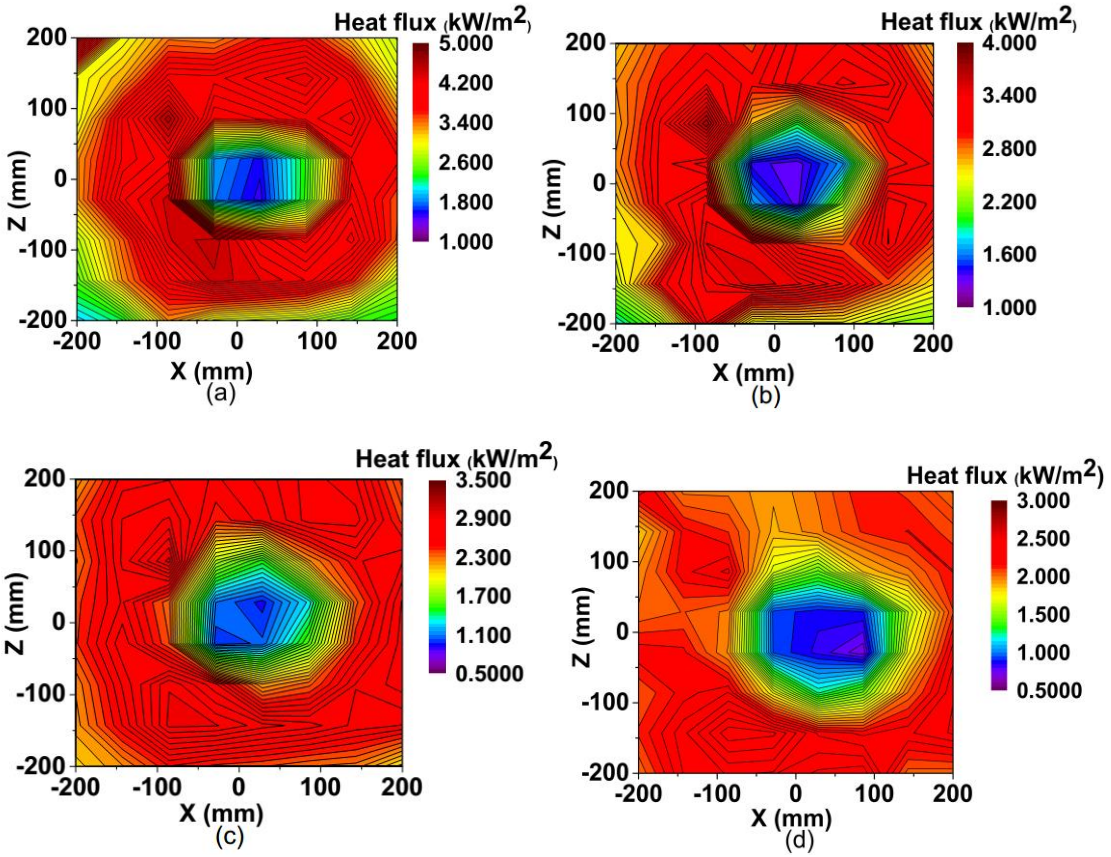

Figure 6.3 Heat flux distribution using only the beam down mirror, with the target point at a distance of 20mm from the focal point; (a) S_1=900mm (b) S_2=1000mm (c) S_3=1100mm (d) S_4=1200mm.

Table 6.1 Comparison of measured heat flux using the mirror and quartz glass at four axial distances from the focal point.

S (mm)	$Q_{max,mg}$ (kW/m²)	$Q_{max,m}$ (kW/m²)	$\frac{Q_{max,\,mg} - Q_{max,\,m}}{Q_{max,\,m}}$ %
S_1	4.57	3.63	-19.51%
S_2	3.46	2.71	-20.00%
S_3	2.75	2.20	-21.68%
S_4	2.46	1.98	-20.57%

Here, S= Distance between the incident target point and the mirror, (mm); $Q_{max,mg}$ = Maximum measured heat flux with mirror and quartz glass (kW/m^2); $Q_{max,m}$ = Maximum measured heat flux with mirror (kW/m^2).

Seventy nine percent of radiation entering the receiver was transmitted though the quartz glass and the remainder was reflected or absorbed by the glass. Heat flux near the focal point was extrapolated to provide the actual focal point intensity which was compared with the theoretical heat flux intensity, as shown earlier in Figure 4.9. This comparison revealed significant deviation from the theoretical value.

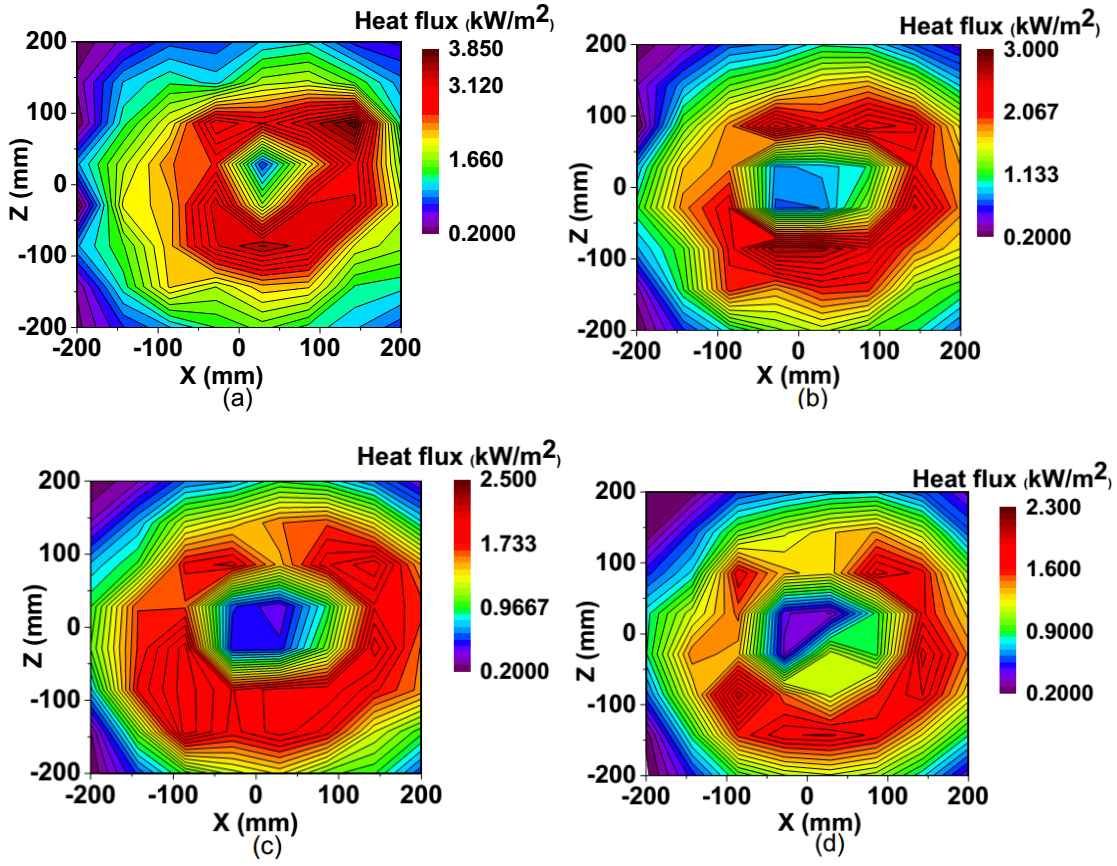

Figure 6.4 Heat flux distribution using the beam down mirror and quartz glass on the aperture, the beam target point on the mirror at a distance 20mm from the focal point; (a) S_1=900mm (b) S_2=1000mm (c) S_3=1100mm (d) S_4=1200mm.

In order to clarify this result, the digital imagery method, as described by Craig [108], was used. Although this method was comparatively complex, it was able to determine the heat flux at the focal point, and

at other points. Using the digital imagery method, the measured heat flux at the aperture was 365,000W/m^2. The total heat input to the cavity was calculated using heat flux at the position of the aperture and the energy loss factor due to the quartz window.

6.3 Thermal behaviour of the receiver

Thermal performance of the solar receiver varied according to the following parameters: air flow, particle concentration and size, and particle free board height. The air flow rate and outlet air temperature are input parameters for the power system. The other parameters can raise the temperature of the outlet air and consequently impact on the thermal efficiency of the receiver.

To understand the effects of recirculating particles inside the receiver, a thermal test was performed with an air and air-particle mixture in two different test cases, as described in Tables 6.2 and 6.3. The test cases were performed using different mass flow rates of air and a different recirculation rate of air inside the receiver. During the experiments, the temperature change of the heat carrying fluid was monitored and the thermal efficiency of the receiver was calculated. The measured data were then further processed to calculate the thermal efficiency, particle volume fraction and power generation efficiency.

6.3.1 Experimental procedure

A rigorous experimental campaign was performed to understand the effect of heat input, via radiation, on the turbulent interaction of the metallic particles and air within the cavity receiver. Figure 6.5 shows a photographic view of the experimental setup to determine the thermal performance of the receiver. The performance of the solid particle solar receiver depends on characteristics of the cavity's inner surface, particle type and size, air flow rate and the optical density of solid particles [60]. Hence, the investigation was conducted by varying the mass flow rate of air, the volume fraction of the particles, particle size, particle concentration, and forced recirculation rate via the internal

fan. Moreover, two different types of particles were used to investigate the effect of particle properties on receiver efficiency and air exit temperatures.

Before running the solar simulator using preheated air, a specific percentage of particles were added to the cavity using the particle port which was then closed during the test run. Next, the cooling air of the beam deflecting mirror was turned on. The solar simulator was then turned on to the specified power level. The air preheater outlet and inlet air valve of the cavity receiver was opened to supply preheated air into the cavity. Preheated air was used to reduce the time required to achieve a thermal equilibrium and a steady state mode. The air electric heater was turned off once the temperature inside the receiver reached 110^0C. The heater remained off for the remainder of the experiment and the ambient air valve was turned on to allow air into the inlet, i.e. inlet air. After turning off the heater, there was no external heating source other than the Xenon radiation source.

After a certain period, the cavities achieved a steady state condition with respect to the cavity temperature under a certain mass flow rate of air and for a specific fan speed. For every mass flow rate of air and fan speed, the steady state temperature cavity temperature and temperature of the exit air were recorded. The fan speed was controlled using the fan controller and pressure inside the cavity was controlled by the pressure regulator valve and pressure safety valve at the inlet, which was monitored continuously. Tables 6.2 and 6.3 summarize the experimental operating conditions.

6.3.2 Measurement uncertainties

Measurement uncertainity of this experiment includes the accuracy of sensor position, instrumental errors, random data collection accuracy. In the case of random error, there was a potential for flow velocity and temperature measurement uncertainty. As outlet air temperature was dependent on the mass flow rate of the air, uncertainity of the flow rate

of the air through the flow meter could affect the inlet velocity of the flow and exit air temperature.

The specifications of the ABB flow meter used in the experiment state an accuracy of 3% of the maximum flow with a repeatability of 0.25% during full scale readings [109]. During the experimental test run, the flow rate varied within 10-40% of the full scale reading, hence the error rate was less than 3%. The general service pressure gauge is another potential source of error for the volumetric flow rate. As per the specifications, 1% accuracy of the presure gauge at a full scale reading was achieved; a very small error in relation to the supplied level of flow. In addition to instrumental errors, parallux errors during the positioning of the flow meter at a specified percentage of flow can occur. The calculated random error of the measured temperature data was 0.12%. The thermocouple accuracy was 0.75%. Temperature data was collected by averaging 1800 samples in 5 seconds, so the standard deviation was reduced due to the high number of observations.

Table 6.2 Test conditions for air as a heat transfer medium.

Location of the stopper, Y (mm)	Air flowrate (kg/s)	Fan speed (RPM)
Y=300	0.0034	0,200,300,400,500
	0.0044	0,200,300,400,500
	0.0065	0,200,300,400,500
Y=400	0.0034	0,200,300,400,500
	0.0044	0,200,300,400,500
	0.0065	0,200,300,400,500
Y=500	0.0034	0,200,300,400,500
	0.0044	0,200,300,400,500
	0.0065	0,200,300,400,500

Therefore, the random error was insignificant. The total calculated uncertainity using Equation (5.4) was 3.25%. This error is omparatively

small and does not have a significant effect on the measured parameters of this analysis.

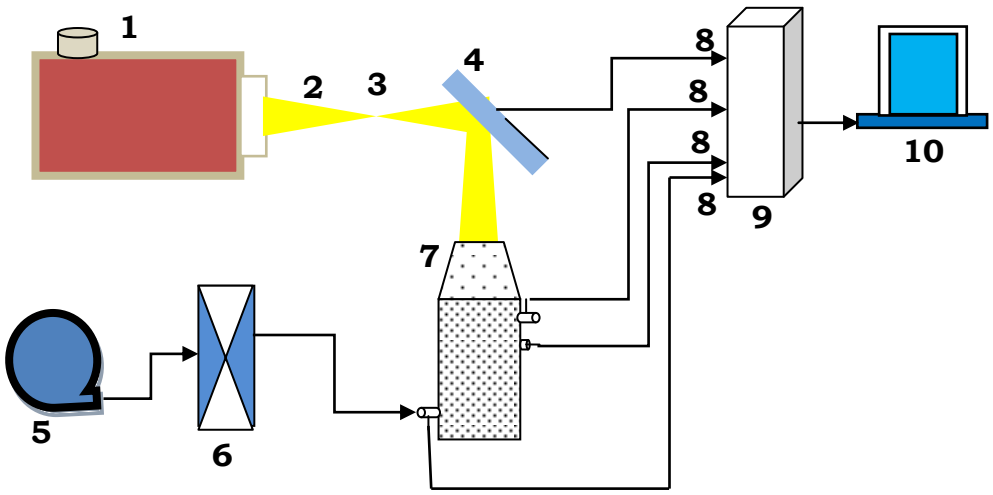

1. Solar simulator
2. Radiation beam
3. Focal point
4. Aluminium reflector
5. Compressor
6. Flow controller
7. SPSR
8. Thermocouple signals
9. DAQ, 10 CPU

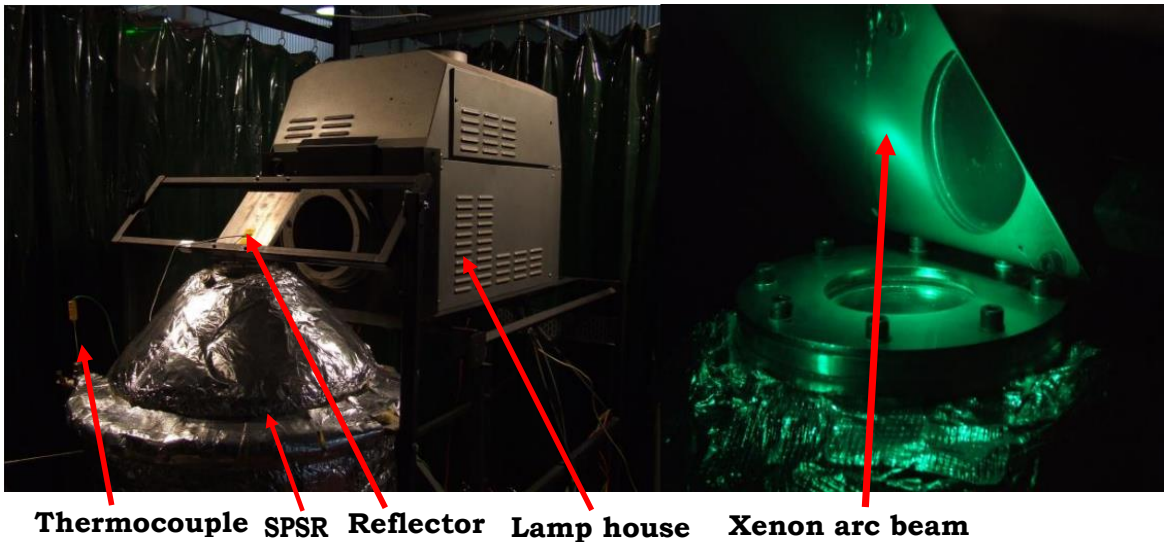

Figure 6.5 Schematic and photograph of the thermal performance experimental setup.

Table 6.3 Test conditions for air and particles as a heat transfer medium.

Particle size (micron)	Volume fractions (%)	Material	Location of the stopper Y(mm)	Mass flowrate of air (kg/s)	Fan speed (RPM)
70	0.044	SiC	No stopper	0.0044	150,200,250,300
70	0.023	SiC	No stopper	0.0044	200,300,400,500,600
200	0.034	SiC	Stopper at Y=300	0.0034	0,200,300,400,500
				0.0044	0,200,300,400,500
				0.0065	0,200,300,400,500
200	0.034	SiC	Stopper at Y=400	0.0034	0,200,300,400,500
				0.0044	0,200,300,400,500
				0.0065	0,200,300,400,500
200	0.034	SiC	Stopper at Y=500	0.0034	0,200,300,400,500
				0.0044	0,200,300,400,500
				0.0065	0,200,300,400,500
200	0.034	Al_2O_3	Stopper at Y=400	0.0034	0,200,300,400,500
				0.0044	0,200,300,400,500
				0.0065	0,200,300,400,500

6.3.3 Results and discussion

Effect of changing particle volume fraction on outlet air temperature

Using the configuration shown earlier in Figure 5.2a, the thermal performance of the receiver was tested using 70micron SiC particles at particle volume fractions of 0.022% and 0.044%. Particle recirculation was observed to start at a fan speed of 150RPM for 70micron particles. Here, the 70micron SiC particles were sized using the average diameter of the particles. The size analyses are shown in Table 6.4. The impact of the forced recirculation rate on the outlet air temperature was investigated by varying the speed from 200 to 600RPM at a constant inlet mass flow rate of air of 0.0044kg/s.

The outlet air temperature remained almost constant, changing from 402K to 406K for an air flow rate of 0.0044 kg/s, when the fan speed was increased from 200 to 300RPM (Figure 6.6). Increasing the particle volume fraction from 0.022%, to 0.044%, had a similar effect on the

outlet air temperature, where the temperature increased from 403K to 406K when the fan speed was increased from 150 to 250RPM.The forced circulation inside the receiver enhanced the mixing of hot and cold particles leading to a steady constant temperature of the system.

The irradiation absorbing particle cloud, composed of different volume fractions in the range of 0.22%-0.0044%, was uniformly mixed and did not lead to a different distribution. Therefore, different particle volume fractions did not show any effect on the outlet air temperature.

An increase in the fan speed, and hence in the forced recirculation rate, resulted in a minor increase in outlet temperature until the fan speed exceeded 250RPM (Figure 6.6a). At this fan speed and higher, particles started depositing on the aperture window. Deposition of particles (starting at point P as shown in Figure 6.6) on the window (see the photograph in Figure 6.7) resulted in a reduction of incident flux into the receiver cavity, in turn resulting in a decrease in the outlet air temperature. An air curtain arrangement near the aperture and a particle stopper were designed to address the particle deposition on the window, as was described earlier in Chapter 5.

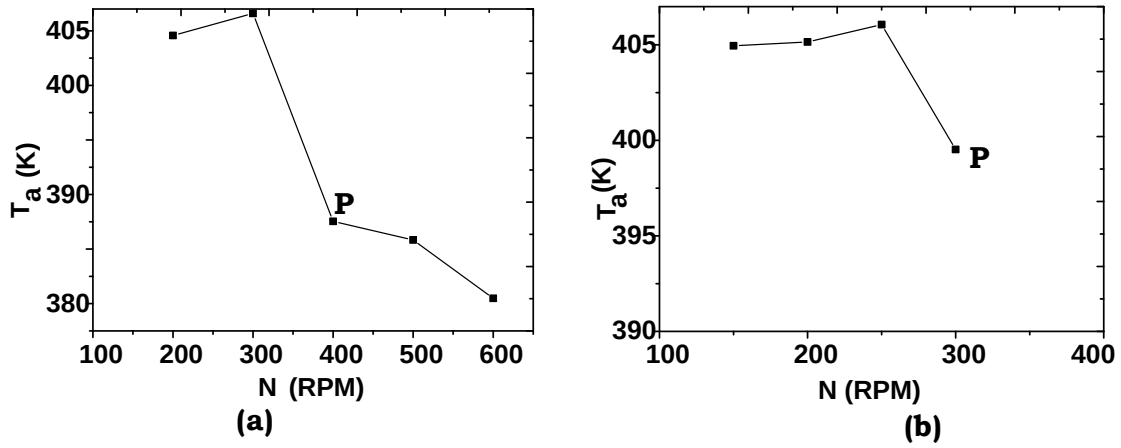

Figure 6.6 Variations of air temperature with changing fan speed at a mass flow rate of 0.0044kg/s; (a) volume fraction=0.022% (b) volume fraction=0.044%.

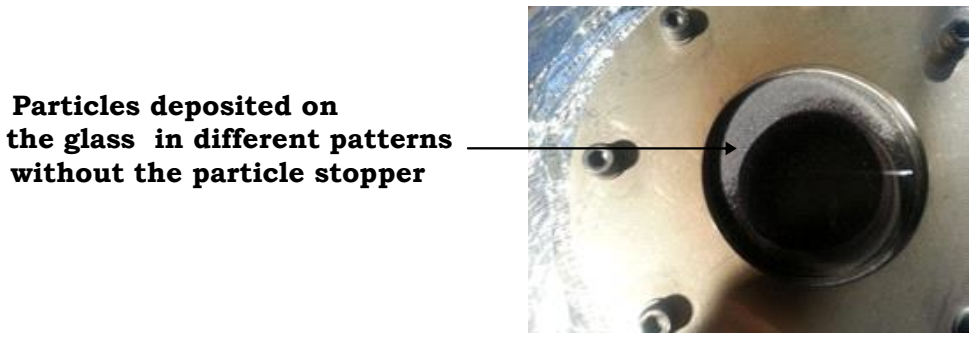

Figure 6.7 Photograph of quartz window showing particle deposition.

A cold test was performed using the configuration shown in Figure 5.3 to determine the fan speed at which no particle was deposited on the window using 200micron SiC and Al_2O_3 particles.

Table 6.4 Size analysis of 70micron SiC particles [109].

Size **70 µm**	**Size distribution (%)**			
	90µm	90~75µm	75~53µm	75~45µm
Limits	0	≤5	≥8	≥38
Analysis	0	4	27	49

The sizing analysis of the 200micron particles is shown in Table 6.5. The 200micron particles were recirculated at a fan speed of 200RPM and above. No noticeable particle deposition on the window occurred until the very high fan speed of 1500RPM.

Table 6.5 Size analysis of 200 micron SiC particles [109].

Size **200 µm**	**Size distribution (%)**				
	300µm	300~212µm	212~180µm	212~150µm	≤125µm
Limits	0	≤25	≥40	≥65	≤3
Analysis	0	19	55	79	1

As reported in previous chapters, particle concentration measurements showed that the particles always followed the cavity wall. Therefore, the stopper near the wall was expected to stop the particles from reaching

the window and forces them to circulate back to the receiver bottom. With the particle stopper installed and the issue of particle deposition eliminated, a new set of experiments was conducted. The experiments used 200micron size SiC and Al_2O_3 particles with a 0.034% volume faction. The receiver was operated with the same radiation input as before and temperatures were monitored to determine the thermal performance of the receiver.

The results show that the particle volume fraction had little effect on the outlet air temperature, once the particles were recirculated at a certain free board height of the receiver cavity (see Figures 6.8a, 6.8d and 6.6). The fan recirculated the air-particle mixture; therefore, the particle cloud consecutively absorbed the solar irradiation and a steady uniform temperature was achieved by the outlet air. Hence, there was no significant change in outlet air temperature with the change of particle volume fractions.

Effect of different particle sizes on temperature of outlet air

Results showed that different particle sizes of 70micron and 200micron, at different volume fractions, resulted in outlet air temperature of approximately 404K at an airflow rate of 0.0034kg/s (see Figures 6.8a, 6.8d and 6.6). Thus, particle size did not increase the outlet air temperature. The surface to volume ratio was higher for the 70micron particles as compared with the 200micron particles. This was expected to enhance convective heat transfer rate from particles to the air. Forced recirculation resulted in a similar particle cloud for different size particles, thus similar effect on outlet air temperature. However, the use of 70micron particles resulted in particle deposition on the window. Hence, the 70micron SiC particles were not used thereafter in this study.

Further parametric analysis was conducted for 200micron sized particles with a SiC/Al_2O_3 particle volume fraction of 0.034%. In this case, the particle free board heights, air flow rate and fan speeds were changed to investigate effects on thermal behaviour of the receiver. The particle free board height was changed by changing the stopper

position to Y=300mm, Y=400mm and Y=500mm from the bottom of the cavity, as shown in Figure 6.8.

Effect of fan speed and air flow rate on outlet air temperature

Outlet air temperature as a function of the fan rotational speed and the mass flow rate of the air at different positions of the particle stopper is shown in Figure 6.8. The experiment was conducted with three different air flow rates of 0.0034kg/s, 0.0055kg/s and 0.065kg/s. To characterize the effect of air alone on outlet air temperature, only air was circulated in the presence of a Xenon lamp heat source. With only air as a heat transfer medium, the results indicate that the maximum outlet air temperature remained almost constant with recorded values of 380K at Y=300mm, 385K at Y=400mm and 381K at Y=500mm for an air mass flow rate of 0.0034Kg/s (Figure6.8). It was also observed that air temperature decreased with the increasing air flow rate from 0.0055kg/s to 0.0065Kg/s. The cavity surface absorbed the incident energy and then transferred the heat to the air through convection. Air temperature was raised at the expense of absorbed energy. As the input energy source was constant, the temperature was reduced according to the increased air flow rate.

The cavity surface absorbed the incident irradiation and transferred the absorbed heat to air when it passed over the cavity's inner surface. Hence, the air flow velocity had a significant effect on heat transfer from the cavity surface to the air. Based on the cavity diameter, the calculated Reynolds number was 10^5 considering the air flow velocity of 500RPM and forced convection was attained due to air forced recirculation.

At a constant inlet mass flow rate of air, increasing the fan speed helped to increase the superficial velocity of the air. Air recirculation by increasing the fan speed did not raise the air temperature significantly. At higher fan rotational speeds of more than 200RPM the thermal performance of the receiver was not improved, as evidenced by the very small increase in the temperature with the increase in fan speed.

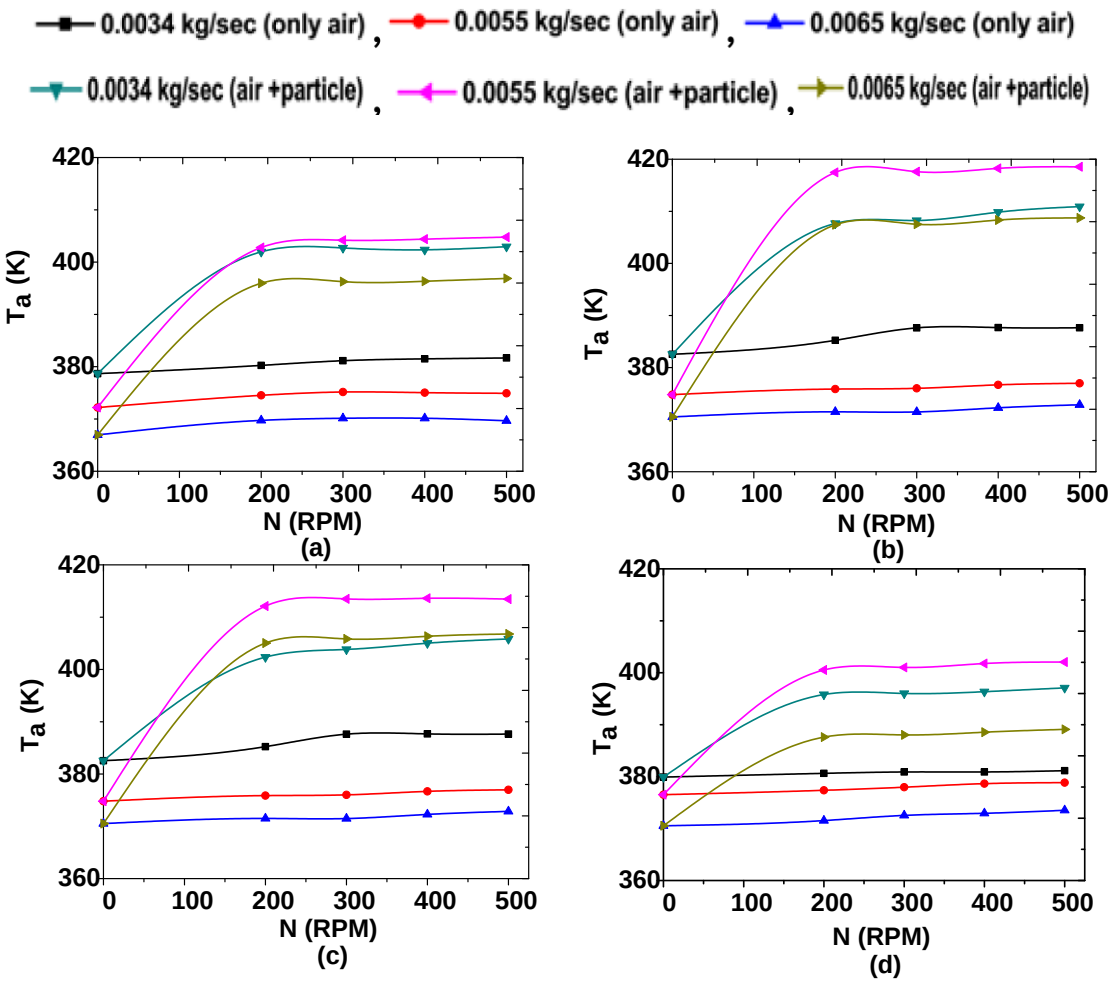

Figure 6.8 Outlet air temperature (T_a) vs fan speed (N) at different mass flow rates of air and different free board height of the receiver; (a) Y=300mm, 200micron SiC (b) Y=400mm, 200micron SiC (c) Y=400mm, 200micron Al_2O_3 (d) Y=500mm, 200micron SiC.

The test case that included particles, recorded a higher maximum outlet air temperature as compared with the test case without particles (Figure 6.8). Also, the measured outlet air temperature was almost constant at different fan speed. For the test case with particles, the outlet air temperature varied between 405K at a particle free board height of Y=300mm, 417K at Y=400mm and 400K at Y=500mm for an air flow rate of 0.0055kg/s. Increasing the air mass flow rate to 0.0065kg/s had a negligible effect on the outlet air temperature at different particle stopper positions. In comparison with the test case of air alone, where the air temperature reached a maximum of 378K, forced recirculation of a specific 0.034% volume fraction of SiC and

Al_2O_3 particles raised the air temperature by ~35K, for a mass flow rate of 0.0055kg/s.

Increasing the fan speed from 200 to 500RPM increased the particles recirculation inside the cavity. Particles and the cavity surface both absorb incoming radiation. The combined effect of convection heat transfer between the cavity surface to air and particles to air occurred and resulted in an increase in the outlet air temperature compared to the test case with only air. A negligible increase in the outlet air temperature was observed at higher rotational speeds when the particles were added into the cavity. Higher rotational fan speeds were shown to change two parameters: (i) air flow velocity increases inside the receiver, as shown in Figures 5.8 and 5.9, and (ii) particle cloud opacity increases for different free board heights, as shown in Figure 5.22. Fast moving air decreased the particle residence time, (see Equation 5.9) resulting in decreased exposure time to the high solar flux zone near the cavity aperture.

Effect of free board height and different particle material on outlet air temperature

Particle concentration decreased with the increasing receiver dimensionless height (Figure 5.21). In addition, the heat transfer rate depends on the particle suspension density and contact length of the cavity surface and residence time of the heat transfer medium [84]. Therefore, the effect of the free board height of suspended particles was investigated by changing the position of the particle stopper (see Figure 6.8). The results show that the outlet air temperature was 405K for a stopper position at Y=300mm, 400K at Y=500mm and 417K at Y=400mm using 200micron SiC. Another experimental run was carried out using 200micron Al_2O_3 for a stopper position at Y=400mm and the outlet air temperature were recorded at 413K (see Figure 6.8c). Hence, it was presumed that sufficient particle suspension density (Figure 5.19 and 5.20) and contact residence time at Y=400mm maximized the transfer of absorbed energy to the air. As a result, the outlet air temperature was higher at Y=400mm when compared with other free

board heights. Interestingly, the outlet air temperature did not change significantly when using Al_2O_3 instead of SiC.

Receiver thermal efficiency and power generation efficiency

Thermal efficiency of a solar receiver is an important parameter in evaluating the working performance of a thermal system, which is defined as the ratio of the heat carried out by the working medium over the incident power. It is expressed as:

$$\eta_{th} = \frac{\dot{m}c_p(T_{a,o} - T_{a,in})}{Q_{in}}. \qquad (6.1)$$

Receiver thermal efficiency, as a function of fan rotational speed and the mass flow rate of air at different positions of the particle stopper, is shown in Figure 6.9. The receiver thermal efficiency did not change significantly by varying the fan speed and the thermal efficiency increased with the increasing mass flow rate of air (Figure 6.9). The thermal efficiency represented by zero RPM shown in Figure 6.9 indicates the thermal efficiency with only air as the HTM. In this test case, a thermal efficiency of 37% was achieved at an air flow rate of 0.0034kg/s and 55% thermal efficiency was achieved at an air flow rate of 0.0065kg/s.

With the air-particle mixture as HTM, the maximum receiver thermal efficiency was 82% at an air flow rate of 0.0065 kg/s and was 45% for a 0.0034kg/s air flow rate at a particle free board height of Y=300mm (Figure 6.9a). The maximum receiver thermal efficiency was 75% at a flow rate of 0.0065kg/s and 42% for 0.0034kg/s at a free board height of Y=500mm (Figure 6.9d). At Y=400mm, the maximum receiver thermal efficiency was about 90% at a flow rate of 0.0065kg/s and 47% for 0.0034kg/s (Figures 6.9b and 6.9c). At a free board height of Y=350mm, the particle' interactions with the wall was lower than at Y=400mm and Y=500mm because of the smaller surface area between the stopper and receiver bottom. In addition, the beam diameter and beam penetration distance, along with the beam intensity, were lower at Y=350mm than at the other two heights.

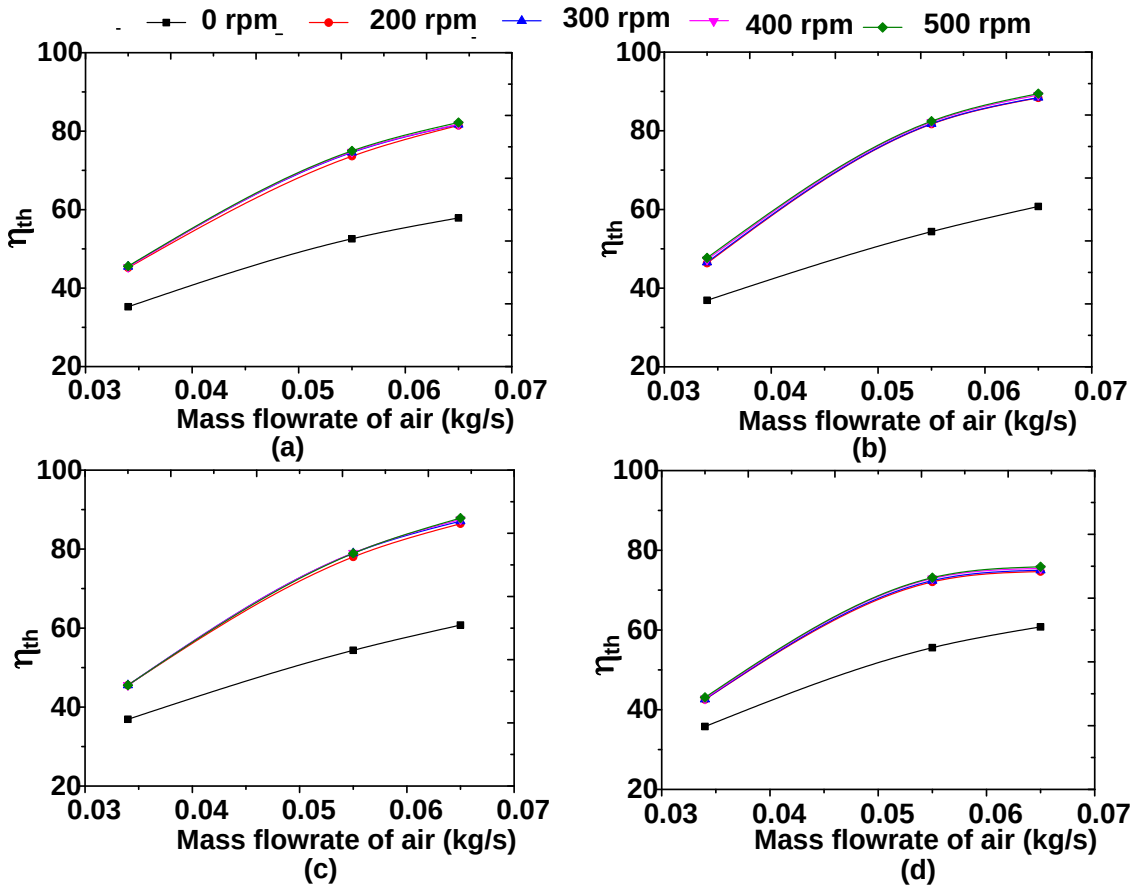

Figure 6.9 Receiver thermal efficiency vs air mass flow rate at different fan speeds; (a) Y=300mm, 200micron SiC (b) Y=400mm, 200micron SiC (c) Y=400mm, 200micron Al_2O_3 (d) Y=500mm, 200micron SiC.

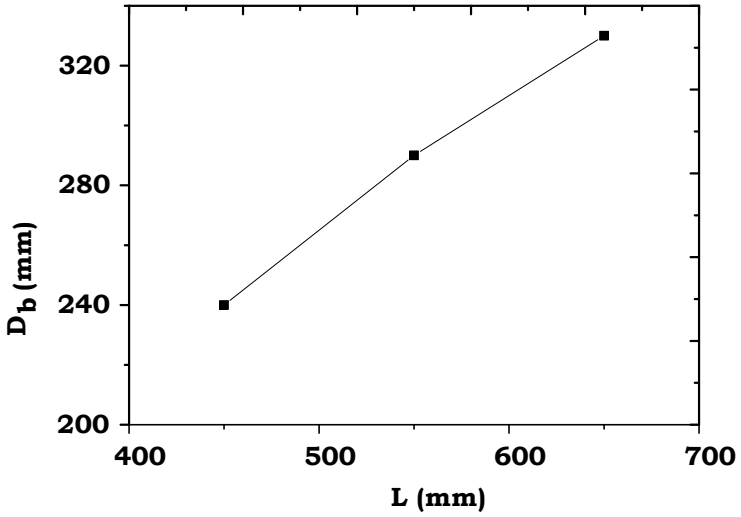

Figure 6.10 change of diverging beam diameters at a distance L (mm) away the focal point.

The beam diameter at Y=350mm was greater than the stopper aperture diameter, which caused re-radiation losses from the cavity. At a distances of Y=500mm and Y=400 mm, the beam diameter was smaller

than the stopper aperture (Figure 6.10) and the resultant beam penetration was higher, when compared with Y=350mm. In addition, at Y=500mm, the particle concentration was lower at the upper free board region (see Figure 5.21) and so reduced the heat transfer to air. At Y=400mm, the beam penetration and particle concentration were optimized and energy absorption increased. The expected interaction of particles, air and wall at Y=400mm was sufficient to minimize re-radiation and other losses and maximize thermal efficiency. Therefore, Y=400mm was treated as the optimum free board height for this recirculating solar receiver. In addition, the higher air flow rate played an important role in increasing the receiver thermal efficiency.

Power generation efficiency was calculated as a function of the outlet air temperature and receiver thermal efficiency. It is obtained by multiplication of the receiver thermal efficiency and Carnot efficiency of the system. It is expressed as:

$$\eta_o = \eta_{th} \times (1 - \frac{T_{a,in}}{T_{a,o}}) \qquad (6.2)$$

Power generation efficiency followed the same trend as receiver thermal efficiency when the fan rotational speed and mass flow rate of air were changed. The maximum power generation efficiency was 24% at a mass flow rate of 0.0065kg/s at a free board height of Y=400mm (see Figure 6.11). The trend of increasing power generation efficiency was dependent on the outlet air temperature and the mass flow rate of air (see Figures 6.11b and 6.11c).

Normalized efficiency was a parameter used to compare the receiver efficiency with efficiencies achieved for the air only test case. Normalized thermal efficiency was defined by the ratio of the receiver thermal efficiencies which were obtained with the air-particle mixture and air only as a heat transfer medium.

The normalized thermal efficiency is expressed as follows:

$$\eta_\tau^* = \frac{\eta_{thap}}{\eta_{tha}} \qquad (6.3)$$

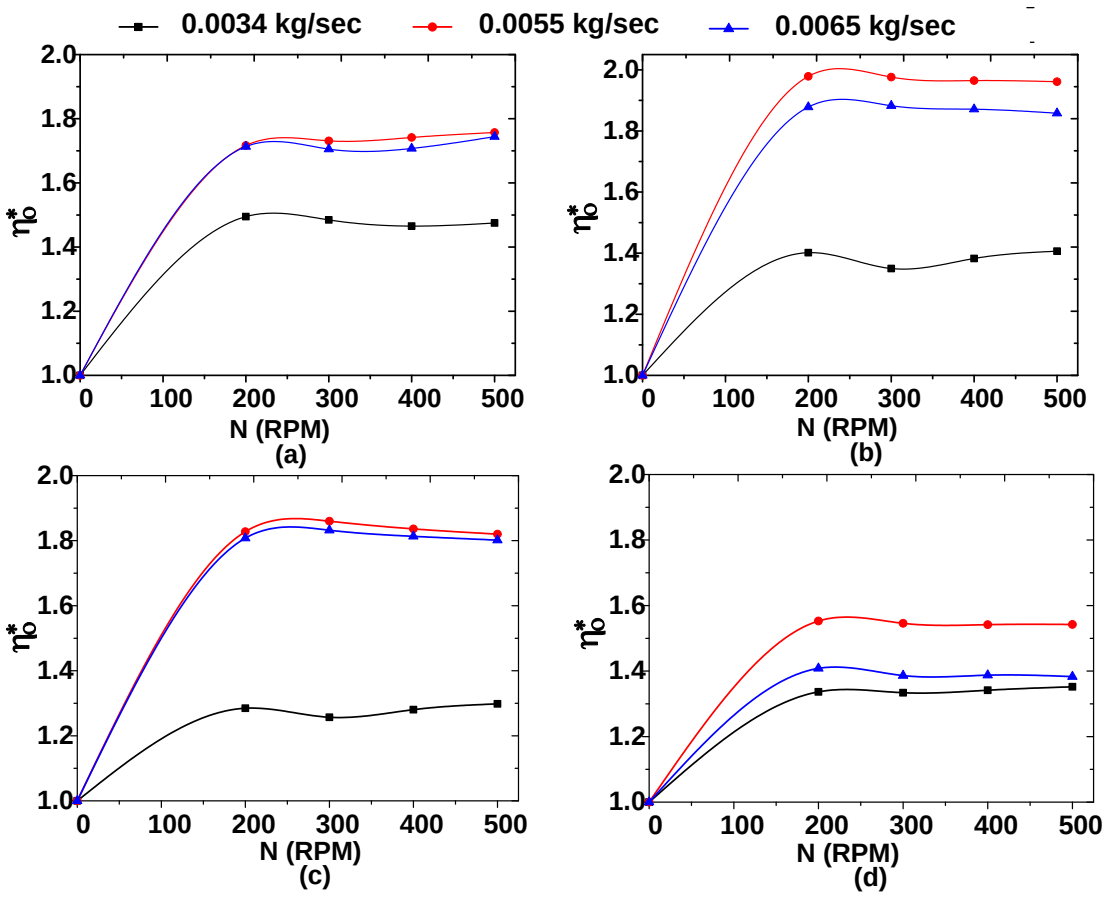

Figure 6.11 Power conversion efficiency vs mass flow rates of air at different fan speeds; (a) Y=300mm, 200micron SiC (b) Y=400mm, 200micron SiC (c) Y=400mm, 200micron Al_2O_3 (d) Y=500mm, 200micron SiC.

Variations of the normalized receiver thermal efficiency with changes of fan rotational speed for different mass flow rates of air are shown in Figure 6.12. Comparing the air-particle and air only test cases, at an air flow rate of 0.0055kg/s, 43% greater thermal efficiency was obtained using the air-particle mixture as a heat transfer medium at a free board height of Y=400mm (Figure 6.12b) and 37% higher thermal efficiency was obtained at a free board height of Y=300mm (Figure 6.12a). Normalized thermal efficiency followed the same trend as the air temperature increased when using the air-particle mixture as a heat transfer medium.

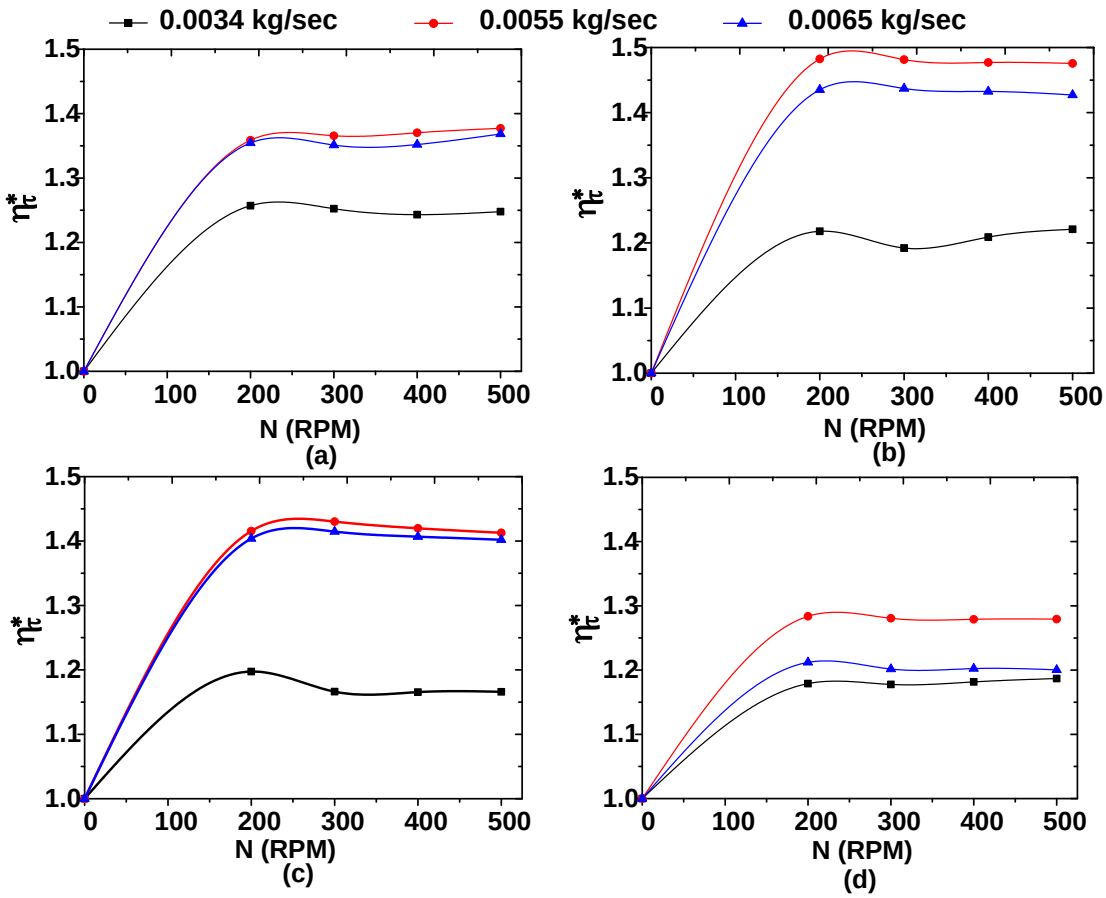

Figure 6.12 Normalized thermal efficiency vs fan speed at different mass flow rates of air; (a) Y=300mm, 200micron SiC (b) Y=400mm, 200micron SiC (c) Y=400mm, 200micron Al_2O_3 (d) Y=500mm, 200micron SiC.

Normalized power generation efficiency was defined by the ratio of receiver power generation efficiencies which were obtained with the air-particle mixture and with only air as a heat transfer medium in the solar receiver. The normalized power generation efficiency is expressed as follows:

$$\eta_o^* = \frac{\eta_{oap}}{\eta_{oa}} \qquad (6.4)$$

Figure 6.13 shows the variation of the normalized power generation efficiency with changing the fan's rotational speed for different mass flow rates of air. Again, comparing the two test cases of air only and the air-particle mixture, at an air flow rate of 0.0055kg/s, 90% more power generation efficiency was recorded using the air-particles mixture as a heat transfer medium at a free board height of Y=400mm (Figure

6.13b), 72% higher power generation efficiency was achieved at a free board height of Y=300mm (Figure 6.13a), and 54% more power generation efficiency was achieved at a free board height of Y=500mm (Figure 6.13d). Increases in the receiver efficiencies indicate that the addition of particles to the air enhanced thermal efficiency, power generation efficiency and outlet air temperature. It is anticipated that forced recirculation of the air and particles increases the residence time of the working medium, which in turn enhances irradiation absorption resulting in higher energy transfer from the particles to the air.

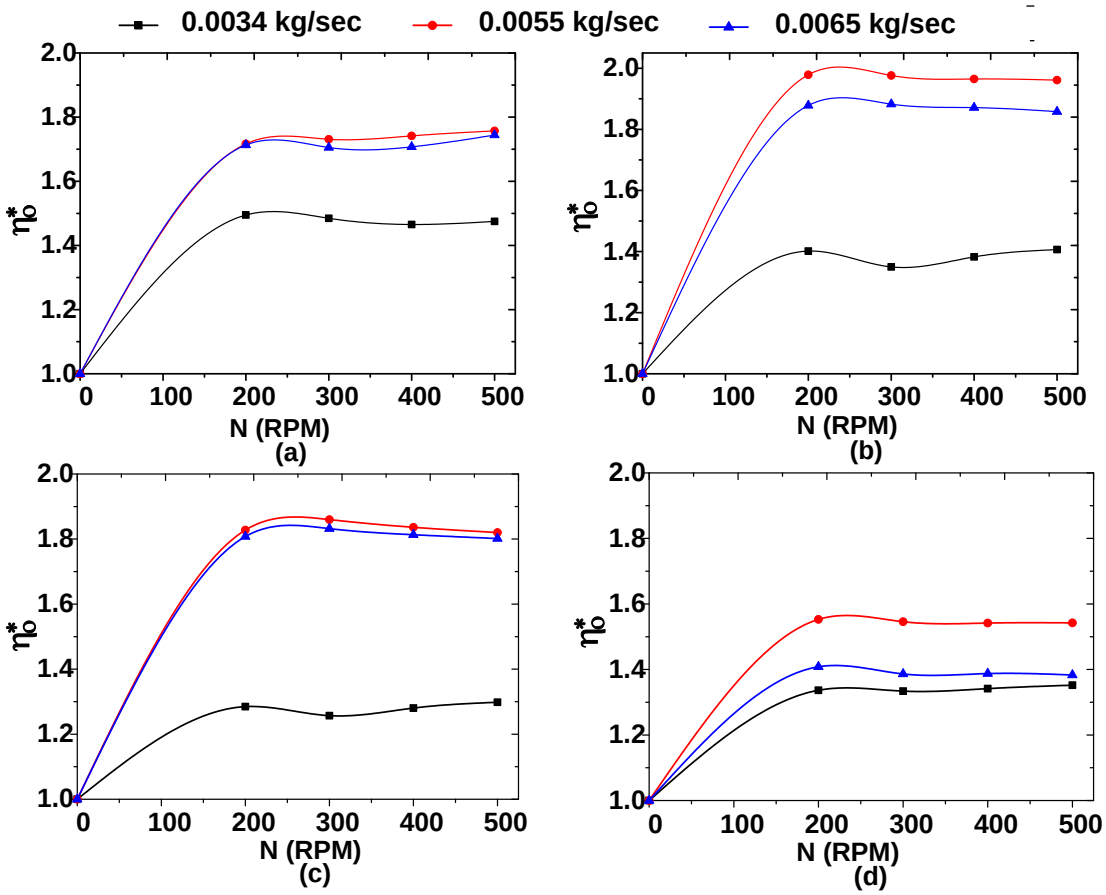

Figure 6.13 Normalized power conversion efficiency vs fan speed at different mass flow rates of air; (a) Y=300mm, 200micron SiC (b) Y=400mm, 200micron SiC (c) Y=400mm, 200micron Al_2O_3 (d) Y=500mm, 200micron SiC.

6.3.4 Discussion on key findings

Efficiency enhanced by recirculating particles with the air

When considering the whole cavity as a free board region, the addition of particles into the solar receiver cavity increased the outlet air temperature by 107K (Figure 6.6) and the thermal efficiency by 23% (Figure 6.14a). An additional thermal efficiency of 49% and an outlet air temperature increase of 123K were achieved when a stopper was added at Y=400mm free board height. In Figure 6.14a the dimensionless temperature T^* is defined by the ratio of outlet air temperature with recirculating particle and outlet air temperature without recirculating particle in the receiver. Thus, by limiting the height of particle circulation, greater radiation was absorbed and less was lost via back reflection.

Changing the volume fraction, α_p, of particles from 0.022% to 0.044% did not change the outlet air temperature or thermal efficiency significantly, as is shown in Figures 6.6 and 6.8a. Changing the particle volume fraction from 0.022% to 0.044% increased the heat transfer coefficient from 190W/m^2.^{0}C to 233W/m^2.^{0}C (Figure 6.14b). For clarity, the heat transfer enhancement as a result of adding particles at different volume fractions, h_p/h_g, and the cavity Reynolds number were plotted for different particle volume fractions (Figure 6.15). Here, h_p and h_g denote the heat transfer coefficient from the air-particle mixture to the air and cavity surface to air respectively which was mentioned in Chapter 3. Figure 6.15 shows that the ratio of h_p/h_g increased from 2.9 to 3.4 when the particle volume fraction was doubled from 0.022% to 0.044%. Also, increasing fan speed increased the cavity Reynolds number and Nusselt number (Figure 6.15). Consequently, h_p/h_g increased with the increasing Reynolds number. Hence, for a significant improvement in the outlet air temperature, a wider range of fan speed and particle volume fractions in the cavity should be investigated.

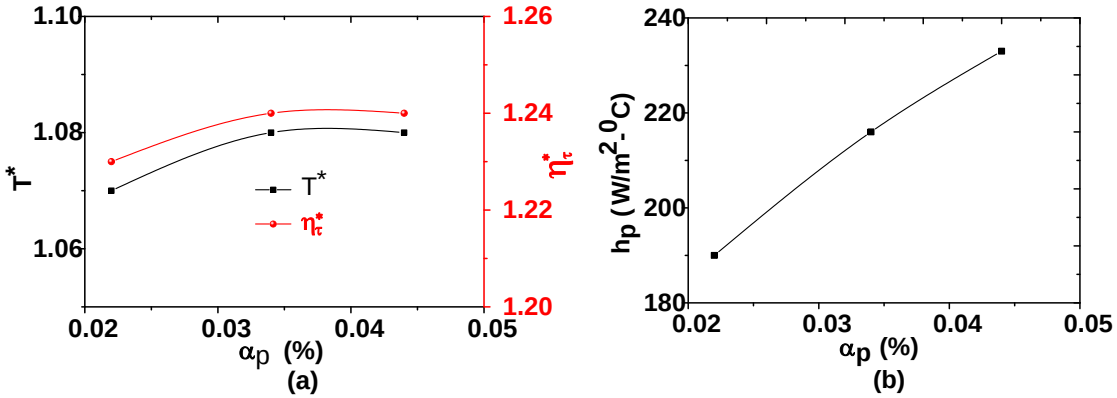

Figure 6.14 Effect of (a) volume fraction on temperature, thermal efficiency and (b) heat transfer coefficient between particles and air.

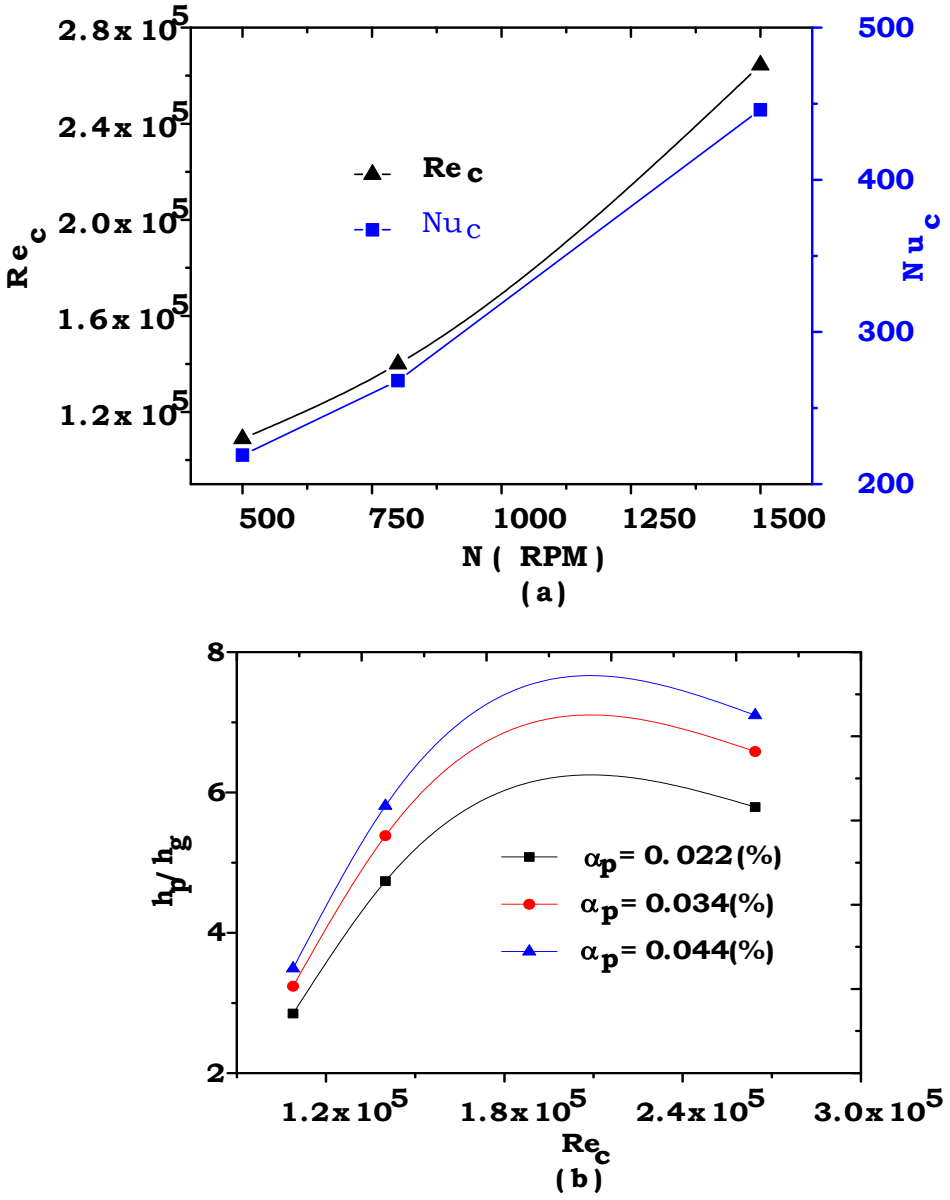

Figure 6.15 Effect of (a) Fan speed on cavity Reynolds number and Nusselt number (b) heat transfer enhancement with the cavity Reynolds number.

Achievements of uniform cavity temperature due to the forced recirculation effect by changing fan speed.

Particle concentration at the free board region increased with an increase in rotational fan speed (Figures 5.19 and 5.20). Using the forced recirculation effect, the upper region of heated suspended particles was mixed with cooler particles from the bottom region consecutively. Figure 6.16 presents the cavity temperature for different RPM at an air flow rate of 0.0055kg/s, showing that a uniform and steady temperature was attained at a certain time period. Therefore, the temperature of the outlet air did not change with a change of fan speed.

Particle spheres exchange heat to air through convection, depending on the relative velocity between the air and particle suspension density and turbulence intensity. Higher Reynolds numbers and Stokes numbers resulted in a higher outlet air temperature with the changing of fan speed (Figures 6.16 and 5.23). Stokes number variations between 200 and 500RPM showed that the slip velocity between the particles and air was not significantly large. The lower slip velocity at this fan speed had a very small effect on the outlet air temperature within this operating fan speed.

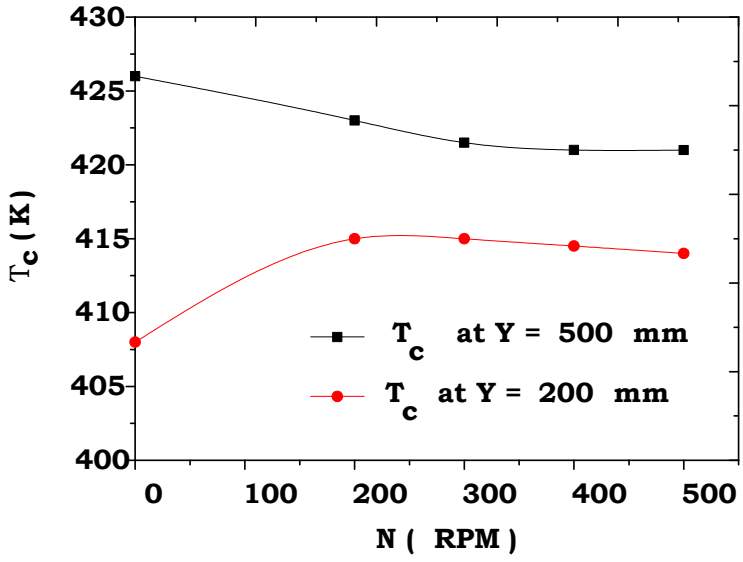

Figure 6.16 Variation of cavity wall temperature (T_c) for different RPM at air flow rate of 0.0055kg/sec.

As mentioned in Chapter 5, forced recirculation induced by the fan and its speed, and the inlet air did not influence the carriage of particles in the free board region. This is a specific difference between a fluidized bed solar receiver and the developed solar receiver where it provides the flexibility of adjusting the air flow rate into the cavity. Hence, for specific input power, this receiver has the potential to control the outlet air temperature by controlling the inlet air flow rate.

Enhanced thermal efficiency for different free board height of particles

The results of an experimental investigation of flow pattern were discussed in the previous chapter. The flow pattern was determined at locations above the duct and above the particle stopper due to limited access and complexity. Using the model developed in Section 3.5, simulated flow patterns for the different configurations were investigated. Velocity vector contours for the case with a duct show that the flow attached itself to the receiver wall with sufficient velocity to carry the particles (Figures 6.17a and 5.6). The flow continued in its upward trajectory until it reached the aperture (glass window). Therefore, more particles were carried near the window, as shown earlier in Figure 5.20. As a result, particles were deposited on the window when the fan speed exceeded 300RPM (see Figure 6.7).

When a particle stopper was used, the flow behaviour changed inside the receiver, as shown in Figure 6.17b. Using the stopper, restriction of the particle flow above the duct solved the problem of particle deposition on the quartz glass window. A recirculating flow with high air velocity was observed below the particle stopper, as compared with the locations above the particle stopper. Particle deposition on the glass was a major problem for all types of solar particle receivers operated with the quartz window system.

The effect of suspended particle concentration, for different free board heights, on thermal efficiency and outlet air temperature of the solar receiver are illustrated graphically in Figure 6.18. Four cases are considered in regards to flow pattern, particle concentration and beam

penetration. Further comparison is shown in Figure 6.19 where temperature ratio and thermal efficiency ratio are plotted versus dimensionless height. Here, temperature ratio is the ratio between outlet air temperature without addition of particles and outlet air temperature with the addition of particles. The four cases are discussed separately as follows:

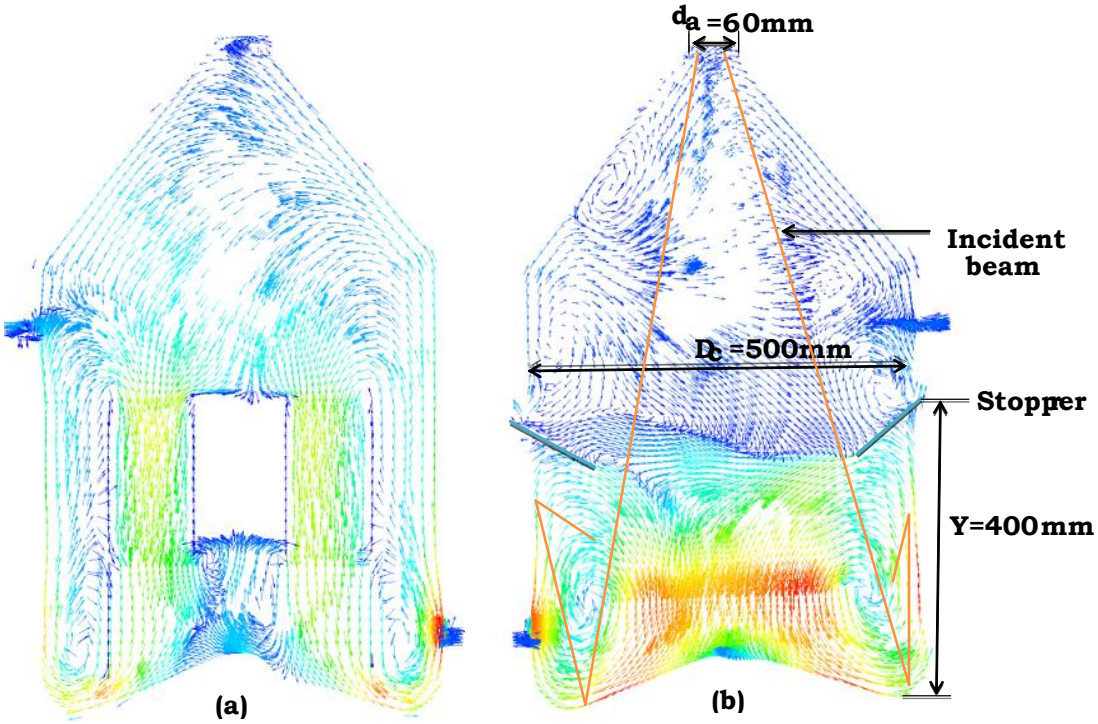

Figure 6.17 Simulated fluid flow pattern (a) with the duct and (b) with the stopper.

(a) Without the particle stopper (Figure 6.18a)

Figure 6.19 shows that the ratio of the temperature of the outlet air was T^*= 1.05 (Here, T^*, the ratio of temperatures of the outlet air when the receiver was operated with the air and particles and without the particle) and thermal efficiency ratio was η^*_τ=1.25 at Y/H=1. The flow patterns presented in Figures 6.17a and 6.18a show that air can carry particles till near the glass window, which was also observed in the experimental investigation as shown earlier in Figure 5.20. The beam penetration was reduced due to the excess particles near the window. Therefore, more re-radiation and reflection losses from particles were

encountered through the window. In practice, and for fan speeds higher than 300RPM, the particles impacted on the glass and reduced the beam penetration into the receiver.

(b) The particle stopper at Y=500mm (Figure 6.18b)

Figure 6.19 shows that the ratio of the temperature of outlet air was T^*= 1.06 and thermal efficiency ratio was η^*_τ=1.28 at Y=500mm (at Y/H=0.57). According to the flow pattern shown in Figures 6.17b and 6.18, the stopper positions of Y=300mm, Y=400mm and Y=500mm resulted in reduced interaction of the flow with the receiver wall as the stopper was moved downwards. For lower positions re-radiation losses were reduced as the radiation beam had penetrated and expanded further into the receiver and away from the aperture window. Also worth noting is that particle concentration was reduced with the increase of freeboard height, as observed in Figure 5.20. In addition, incident beam intensity decreased with increasing depth of the particle receiver, as shown in the Figure 4.14. Noteworthy, is that the lower particle concentration, at Y=500mm, reduced the absorbed energy from the beam leading to a reduction in thermal efficiency, as compared with Y=400mm.

(c) The particle stopper at Y=400mm (Figure 6.18c)

Figure 6.19 shows that the ratio of the temperature of outlet air was T^*= 1.11 and thermal efficiency ratio was η^*_τ=1.48 at Y=400mm (at Y/H=0.46). The flow pattern in Figure 6.17b shows a very low velocity of air at the central region above the stopper position. Here, the beam penetrated through the opening of the aperture with less restriction by the particles near the aperture. It is considered that the beam would have interacted with the upward moving particles and further penetrated all the way to the bottom of the receiver where it would have been reflected back and consequently absorbed by the particles and the walls. The particle concentration was higher than at Y=500mm, as shown in Figure 5.20. Therefore, more energy was absorbed. As there was sufficient cavity space, multiple internal reflections of the beam reduced re-radiation losses and increased energy absorption by the

particles and cavity wall. Hence, an increase in receiver thermal efficiency was observed at this free board height.

(d) The particle stopper at Y=300mm (Figure 6.18d)

Figure 6.19 shows that the ratio of the temperature of the outlet air was T^*= 1.06 and thermal efficiency ratio was η^*_τ=1.28 at Y=300mm (at Y/H=0.35). The flow pattern in Figures 6.17b and 6.18d show that the air and particles recirculate within a small space within the cavity, as compared with freeboard height at Y=400mm and Y=500mm. The beam is able to penetrate through as there were no particles until ~610mm from the window. At Y=300mm, the distance between the bottom and opening of the particle stopper was only 240mm which is the reason that part of the incident beam reflected from the bottom surface or from the recirculating particles. At 500RPM, recirculation velocity was 3.5m/s. Figure 5.6 showed that this velocity increased with decrease in the cavity height. This revealed that the particle and gas residence time in the cavity space at Y=300mm was less as compared to Y=400mm and Y=500. Consequently, the residence time of particles in the irradiation was lower. Hence, energy absorption and convection by the particles is expected to be lower which results in lower temperature and thermal efficiencies at Y=300mm compared with Y=400mm.

The above analysis shows that the penetrated beam was internally reflected and absorbed by the particles in the cavity space below the stopper (Figure 6.17b). This feature ensures efficient energy absorption and transfer by the recirculating particles in the cavity.

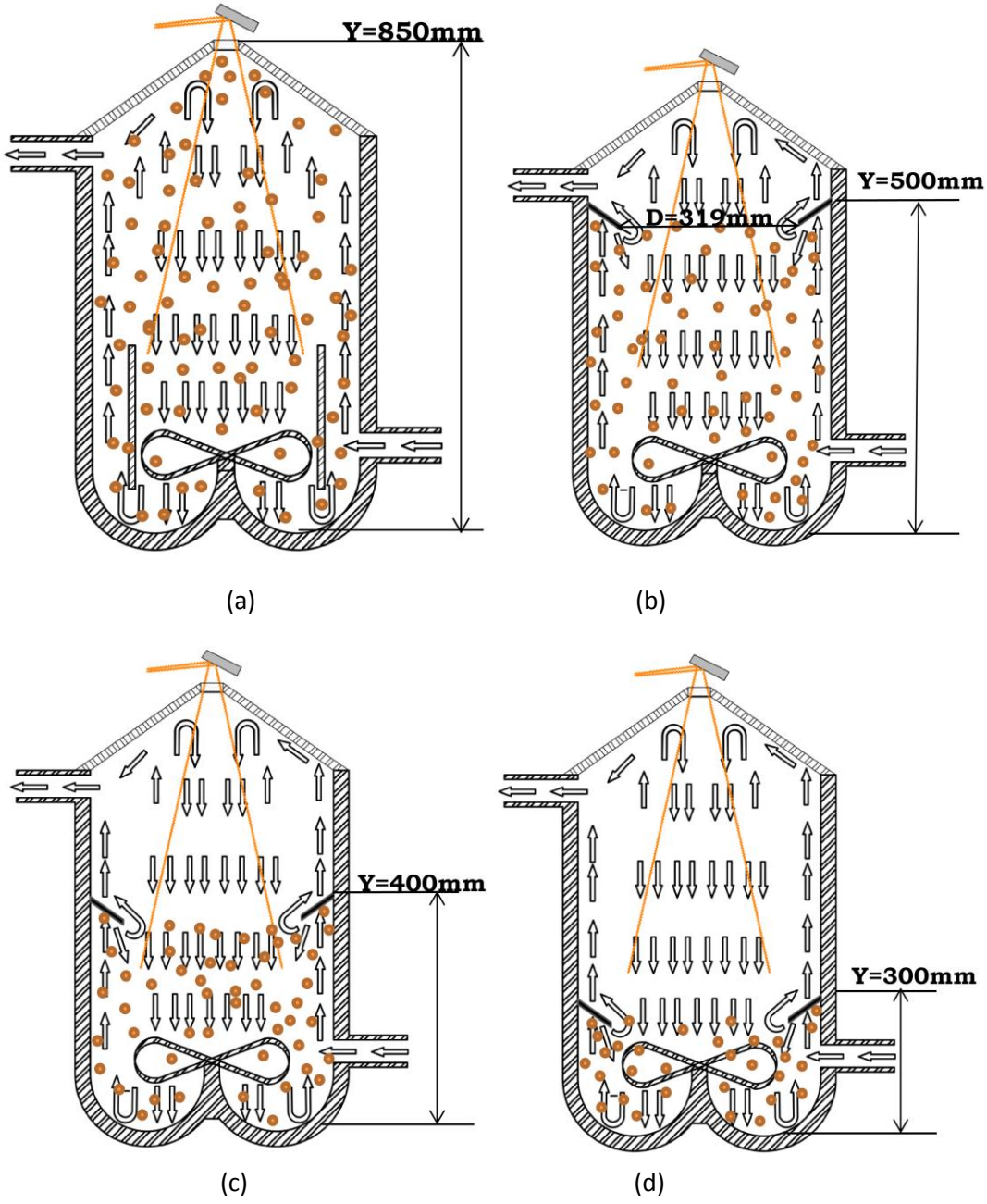

Figure 6.18 Schematic of the receiver showing beam penetration, (a) without particle stopper (b) particle free board height at Y=300mm (c) particle free board height at Y=400mm (d) particle free board height at Y=500mm.

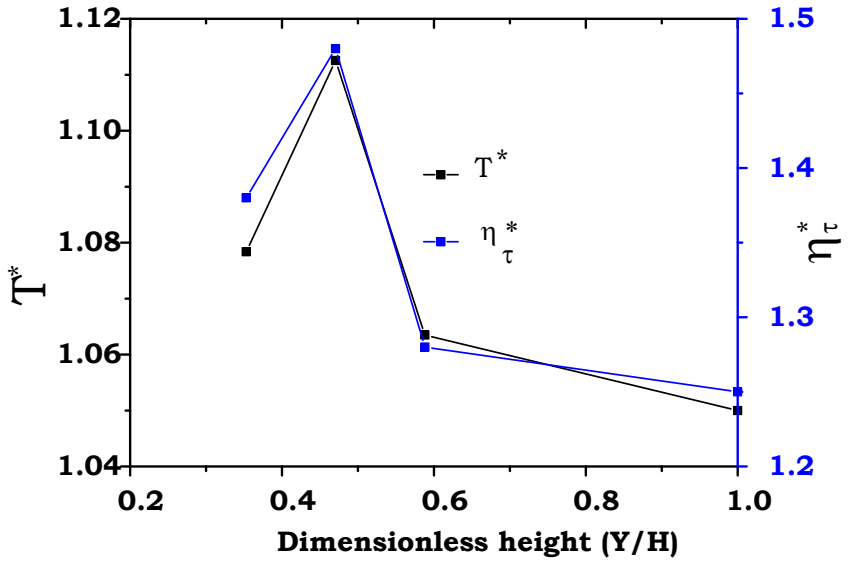

Figure 6.19 Variation of dimensionless temperature and thermal efficiency with dimensionless height.

Chapter 7
Conclusions and Future study

7.1 Introduction

This thesis addresses the need for improved thermal performance of solar receivers. This research project overviewed different types of solar receivers in order to identify and develop a concept with the potential to increase performance of solar receivers. As a result, a recirculating flow solid particle cavity type solar receiver, was designed, fabricated and tested experimentally. The developed solar receiver features a cavity configuration with a ducted fan that continuously recirculates a mixture of air and non-reacting particles in the directly irradiated solar receiver. A comparative analysis was performed to investigate aerodynamic behaviour and thermal performance of the newly developed recirculating flow solid particle solar receiver. Experimental testing involved differing particle sizes and types, namely black SiC and Al_2O_3, and various air flow velocities and speeds of the fan.

7.2 Conclusions

The motivation behind this research was to develop a solid particle solar receiver with higher heat transfer efficiency as compared with conventional solar receivers. The concept of continuously recirculating the air and particle mixture was tested experimentally and a new cavity type solar receiver was constructed. Fluid dynamics and thermal tests were performed to characterize the new conceptual cavity type solid particle solar receiver. Results of the fluid dynamics behaviour of air and particles show that complete forced recirculation of air and particle was achieved by introducing an axial flow fan. forced recirculation

characteristics of air and particles in the cavity increased residence time of the HTM which resulted in an increase in the heat transfer to air. Opacity of the particle cloud in the cavity decreased with the increasing free board height of the cavity which provided better penetration for the incident beam of the Xenon lamp.

A 5kW Xenon lamp based solar simulator was used as a radiation source to perform the thermal test of the solar receiver. Measurements of the heat transfer to the air were performed for air flowing with and without micron sized SiC and Al_2O_3 particles. Using a Xenon Arc power level of 4200 watt, the following conclusions were drawn from the thermal testing of the developed cavity type solar receiver:

(i) The addition of 0.034% volume fraction of SiC particles to the air significantly increased total heat transfer to air in the presence of both forced convection and radiation heat sources. In particular, the outlet air temperature increased to 83K and a thermal efficiency of 55% was achieved without adding any particles to the air. With the addition of air to the 0.034% volume fraction particles, the outlet air temperature was increased by 123K and the thermal efficiency was increased to 89%. Comparatively, better heat transfer was observed for SiC particles than Al_2O_3.

(ii) With the addition of metallic particles into the cavity, thermal efficiency was increased to 49% and power generation efficiency was increased to 90% which shows the effectiveness of continuously recirculating the air and particles into a cavity type solid particle solar receiver. Thermal efficiency and outlet air temperature did not change significantly with an increase in rotational fan speed and particle volume fraction. Thermal efficiency and the outlet air temperature increased at a higher mass flow rate of air.

(iii) An increase in thermal and power generation efficiency of more than 50% demonstrates that the developed concept has

the potential to enhance the heat absorption and heat transfer capacity of the solar receiver.

(iv) Increasing the outlet air temperature and thermal efficiency by increasing the injected mass flow rate of air into the receiver reveals that mixing plays an important role in increasing the efficiency of the cavity type solid particle solar receiver. Improved mixing of air and particles in the cavity can provide uniform temperature distribution which results in the effective absorption of incident energy and convection heat transfer between the HTMs.

Potential applications for this receiver include hot air and high temperature particle production for operating Brayton cycles, decomposition of biomasses and solar combustion of coal, solar chemical combustion to produce solar fuel, and so forth.

7.3 Recommendations for future research

Recommendations for future research are:

(i) Development of a numerical model to optimize the design and performance parameters;

(ii) Investigation of particle flow patterns using Particle Image Velocimetry (PIV) and investigation of slip velocity to improve the performance of the solar receiver;

(iii) Investigation of methods to improve the quartz window cleaning system;

(iv) Spectral absorptivity of the solar receiver cavity and particles should be explored to improve the thermal efficiency of the current solar receiver.

(v) Testing involving other particle materials and different particle sizes may lead to further optimization of the thermal performance.

(vi) A better design of the particle recirculating system that can remove the fan.

(vii) The claimed temperature was the required operating temperature of a high temperature Brayton cycle. Of course,

the current technology is an efficient technology to use more input heat effectively and achieve higher outlet temperature of air. However, it was achieved only 406K. Only 49% heat was converted to solar energy at the wavelength's ranges of solar radiation. The 5kW light source was not activated as an 5 kW input radiation energy source. The preliminary numerical investigation showed that about air temperature of 800K was possible to achieve, if whole 5kW is kept as an input heating source. Hence, another additional 2.5 kW was required to add into the system to achieve 800K temperature with the existing system. If the cavity depth and cavity diameter ratio is reduced, then it is possible to increase the outlet air temperature using the current solar simulator. Hence, this parametric analysis is suggested for further investigation.

References

[1] N. Nakicenovic, "A special report of working group III of the intergovernmental panel on climate change," Cambridge university press, Cambridge, U.K.2000.

[2] IPCC, "Impacts, adaptation & vulnerability: technical summary: climate change 2001," Cambridge university press, UK: 56.2001a.

[3] Greenpeace, "Concentrating solar power outlook 09. Why renewable energy is hot",Technical report," European solar thermal electricity association and IEA solar PACES, A Technical report2009.

[4] N. Lewis and D. G. Nocera, "Powering the planet: chemical challenges in solar energy utilization," *Proceedings of the National Academy of Sciences,* vol. 103, pp. 15729-15735, 2006.

[5] S. Vergura and V. de Jesus Lameira, "Technical-financial comparison between a PV plant and a CSP plant," *Sistemas & Gestão,* vol. 6, pp. 210-220, 2011.

[6] O. Behar, A. Khellaf, and K. Mohammedi, "A review of studies on central receiver solar thermal power plants," *Renewable and Sustainable Energy Reviews,* vol. 23, pp. 12-39, 2013.

[7] Maria, "Technology roadmap:solar thermal electricity," *International Energy Agency, Tech. Rep,* 2014.

[8] www.3tier.com/maps/3tier_solar_irradiance.pdf,/15/02/2015.

[9] D. Arvizu, "Fulfilling the promise of renewable energy: a look at the future," National renewable energy Lab., Golden, CO (US)2005.

[10] http://www.solarpowerworldonline.com/15/02/2015.

[11] A. L. Ávila-Marín, "Volumetric receivers in solar thermal power plants with central receiver system technology: A review," *Solar Energy,* vol. 85, pp. 891-910, 2011.

[12] S. A. Kalogirou, "Solar thermal collectors and applications," *Progress in energy and combustion science,* vol. 30, pp. 231-295, 2004.

[13] http://mcensustainableenergy.pbworks.com/15/02/2015.

[14] http://www.futures-e.org/ CSP_State_of_the_Art.pdf/17/02/2015.

[15] S. Sukhatme, Solar energy-principles of thermal collection and storage, Second edition ed. New Delhi: Tata McGraw-Hill, 1999.

[16] E. C. (EC), "SOLGATE Solar hybrid gas turbine electric power system-final published report," European commission contract ENK5-CT-2000-03333, Publication office2002.

[17] R. Buck, E. Lüpfert, and F. Tellez, "Receiver for solar-hybrid gas turbine and CC systems (REFOS)," in *Proc. 10th SolarPACES Int. Symp. Solar Thermal 2000*, 2000, pp. 95-100.

[18] K. Kitzmiller and F. Miller, "Thermodynamic cycles for a small particle heat exchange receiver used in concentrating solar power plants," *Journal of Solar Energy Engineering,* vol. 133, pp. 031014-031014, 2011.

[19] A. Hunt and C. Brown, "Solar test results of an advanced direct absorption high temperature gas receiver (SPHER)," in *Proceedings of the Solar World Congress*, 1983, pp. 959-63.

[20] A. Steinfeld, M. Brack, A. Meier, A. Weidenkaff, and D. Wuillemin, "A solar chemical reactor for co-production of zinc and synthesis gas," *Energy,* vol. 23, pp. 803-814, 1998.

[21] A. Meier, "A predictive CFD model for a falling particle receiver/reactor exposed to concentrated sunlight," *Chemical engineering science,* vol. 54, pp. 2899-2905, 1999.

[22] S. Granz .J, Th., Sturzenegger M.,, "A new design for volumetric gas/particle reactors for the solar thermal reduction of metal oxides," Annual report 1997.

[23] K. Kim, N. Siegel, G. Kolb, V. Rangaswamy, and S. F. Moujaes, "A study of solid particle flow characterization in solar particle receiver," *Solar Energy,* vol. 83, pp. 1784-1793, 2009.

[24] N. Siegel and G. Kolb, "Design and on-sun testing of a solid particle receiver prototype," in *Energy Sustainability,*, Florida, USA, 2008, pp. 10–14.

[25] J. Hruby, R. Steeper, G. Evans, and C. Crowe, "An experimental and numerical study of flow and convective heat transfer in a freely falling curtain of particles," *Journal of fluids engineering,* vol. 110, pp. 172-181, 1988.

[26] "Evaluating policies in support of the deployment of renewable power, IRENA " 2012.

[27] www.cspworld.com/16/02/2015.

[28] C. K. Ho and B. D. Iverson, "Review of high-temperature central receiver designs for concentrating solar power," *Renewable and Sustainable Energy Reviews,* vol. 29, pp. 835-846, 2014.

[29] P. Heinrich, G. Keintzel, and C. Streuber, "Technology program solar air receiver—2.5 MWt system test on volumetric air receiver technology," in *Proceedings of the 6th International Symposium on Solar Thermal Concentrating Technologies*, 1992, pp. 247-261.

[30] L. Aichmayer, "Solar receiver design and verification for small scale polygeneration unit," Master of Science, Graz University of Technology, Austria, Stockholm , Sweden, 2011.

[31] O. Behar, A. Khellaf, and K. Mohammedi, "A review of studies on central receiver solar thermal power plants," *Renewable and Sustainable Energy Reviews,* vol. 23, pp. 12-39, 2013.

[32] H. R. W. Stine W.B. (1986). *Solar Energy Systems Design.*

[33] O. K. Mande, "Window and seal design for a small particle solar receiver," 2012.

[34] T. Fend, B. Hoffschmidt, R. Pitz-Paal, O. Reutter, and P. Rietbrock, "Porous materials as open volumetric solar receivers: experimental determination of thermophysical and heat transfer properties," *Energy,* vol. 29, pp. 823-833, 2004.

[35] O. K. Mande, "Window and seal design for a small particle solar receiver," 2012.

[36] T. Fend, "High porosity materials as volumetric receivers for solar energetics," *Optica Applicata,* vol. 40, pp. 271-284, 2010.

[37] B. Treece and B. Anderson, "Brayton-cycle baseload power tower CSP system," Concentrating solar power program review *2013,* p. 37, 2013.

[38] M. Roeb, M. Neises, N. Monnerie, C. Sattler, and R. Pitz-Paal, "Technologies and trends in solar power and fuels," *Energy & Environmental Science,* vol. 4, pp. 2503-2511, 2011.

[39] T. Kodama, T. Moriyama, T. Shimoyama, N. Gokon, H. Andou, and N. Satou, "Ru/ Ni–Mg–O Catalyzed SiC-foam absorber for solar reforming receiver-reactor," *Journal of solar energy engineering,* vol. 128, pp. 318-325, 2006.

[40] R. Pitz-Paal, B. Hoffschmidt, M. Bohmer, and M. Becker, "Experimental and numerical evaluation of the performance and flow stability of different types of open volumetric absorbers under non-homogeneous irradiation," *Solar Energy,* vol. 60, pp. 135-150, 1997.

[41] A. Kribus, P. Doron, R. Rubin, R. Reuven, E. Taragan, S. Duchan, and J. Karni, "Performance of the directly-irradiated annular pressurized receiver (DIAPR) operating at 20 bar and 1,200^{0}C," *Journal of solar energy engineering,* vol. 123, pp. 10-17, 2001.

[42] J. Karni, A. Kribus, R. Rubin, and P. Doron, "The" Porcupine": A novel high-flux absorber for volumetric solar receivers," *Transaction, American Society of Mechanical Engineering, Journal of Solar Energy.,* vol. 120, pp. 85-95, 1998.

[43] J. Karni, A. Kribus, P. Doron, R. Rubin, A. Fiterman, and D. Sagie, "The DIAPR: a high-pressure, high-temperature solar receiver," *Journal of solar energy engineering,* vol. 119, pp. 74-78, 1997.

[44] B. Hoffschmidt, F. M. Tellez, A. Valverde, J. Fernandez, and V. Fernandez, "Performance evaluation of the 200-kW HiTRec-II open volumetric air receiver," *Journal of solar energy engineering,* vol. 125, pp. 87-95, 2003.

[45] R. Buck, C. Barth, M. Eck, and W. D. Steinmann, "Dual-receiver concept for solar towers," *Solar Energy,* vol. 80, pp. 1249-1254, 2006.

[46] A. Carotenuto, F. Reale, G. Ruocco, U. Nocera, and F. Bonomo, "Thermal behaviour of a multi-cavity volumetric solar receiver: Design and tests results," *Solar Energy,* vol. 50, pp. 113-121, 1993.

[47] B. Variot, T. Menigault, and G. Flamant, "Modelling and optimization of a two-slab selective volumetric solar receiver," *Solar energy,* vol. 53, pp. 359-368, 1994.

[48] W. E. Pritzkow, "Pressure loaded volumetric ceramic receiver," *Solar energy materials,* vol. 24, pp. 498-507, 1991.

[49] J. Karni, A. Kribus, B. Ostraich, and E. Kochavi, "A high-pressure window for volumetric solar receivers," *Journal of Solar Energy Engineering,* vol. 120, pp. 101-107, 1998.

[50] T. Fend, R. Pitz-Paal, O. Reutter, J. Bauer, and B. Hoffschmidt, "Two novel high-porosity materials as volumetric receivers for concentrated solar radiation," *Solar energy materials and solar cells,* vol. 84, pp. 291-304, 2004.

[51] A. Kribus, P. Doron, R. Rubin, J. Karni, R. Reuven, S. Duchan, and E. Taragan, "A Multistage solar receiver the route To high temperature," *Solar Energy,* vol. 67, pp. 3-11, 1999.

[52] R. Buck, M. Abele, J. Kunberger, T. Denk, P. Heller, and E. Lüpfert, "Receiver for solar-hybrid gas turbine and combined cycle systems," *Le Journal de Physique IV,* vol. 9, pp. Pr3-537-Pr3-544, 1999.

[53] I. Hischier, D. Hess, W. Lipi ski, M. Modest, and A. Steinfeld, "Heat transfer analysis of a novel pressurized air receiver for concentrated solar power via combined cycles," *Journal of Thermal Science and Engineering Applications,* vol. 1, pp. 041002-6, 2009.

[54] A. J. Hunt, "Small particle heat exchangers," 2011.

[55] T. Tan and Y. Chen, "Review of study on solid particle solar receivers," *Renewable and Sustainable Energy Reviews,* vol. 14, pp. 265-276, 2010.

[56] M. Abdelrahman, P. Fumeaux, and P. Suter, "Study of solid-gas-suspensions used for direct absorption of concentrated solar radiation," *Solar Energy,* vol. 22, pp. 45-48, 1979.

[57] J. Martin and V. J. Jr., "A solar central receiver utilizing a solid thermal carrier," Sandia National Laboratories SAND-82-8203; EDB-82-088243English, 1982.

[58] J. HRUBY and V. BUROLLA, "Solid particle receiver experiments: Velocity measurements," ed: Sandia National Labs., Livermore, CA (USA), 1984.

[59] H. Chen, Y. Chen, H. T. Hsieh, and N. Siegel, "Computational fluid dynamics modeling of gas-particle flow within a solid-particle solar receiver," *Journal of solar energy engineering,* vol. 129, p. 160, 2007.

[60] N. P. Siegel, C. K. Ho, S. S. Khalsa, and G. J. Kolb, "Development and evaluation of a prototype solid particle receiver: on-sun testing and model validation," *Journal of solar energy engineering,* vol. 132, pp. 021001-8, 2010.

[61] N. P. Siegel, C. K. Ho, S. S. Khalsa, and G. J. Kolb, "Development and evaluation of a prototype solid particle receiver:on-sun testing and model validation," *Journal of solar energy engineering,* vol. 132, p. 021008, 2010.

[62] A. Steinfeld, "Solar thermochemical production of hydrogen—a review," *Solar Energy,* vol. 78, pp. 603-615, 2005.

[63] T. Kodama, S.-i. Enomoto, T. Hatamachi, and N. Gokon, "Application of an internally circulating fluidized bed for windowed solar chemical reactor with direct irradiation of reacting particles-article no. 014504," *Journal of solar energy engineering,* vol. 130, 2008.

[64] A. Z'Graggen and A. Steinfeld, "Hydrogen production by steam-gasification of carbonaceous materials using concentrated solar energy–V. Reactor modeling, optimization, and scale-up," *international journal of hydrogen energy,* vol. 33, pp. 5484-5492, 2008.

[65] C. C. Agrafiotis, C. Pagkoura, S. Lorentzou, M. Kostoglou, and A. G. Konstandopoulos, "Hydrogen production in solar reactors," *Catalysis today,* vol. 127, pp. 265-277, 2007.

[66] R. Adinberg and M. Epstein, "Experimental study of solar reactors for carboreduction of zinc oxide," *Energy,* vol. 29, pp. 757-769, 2004.

[67] E. Bilgen and J. Galindo, "High temperature solar reactors for hydrogen production," *international journal of hydrogen energy,* vol. 6, pp. 139-152, 1981.

[68] C. Agrafiotis, M. Roeb, A. Konstandopoulos, L. Nalbandian, V. Zaspalis, C. Sattler, P. Stobbe, and A. Steele, "Solar water splitting for hydrogen production with monolithic reactors," *Solar energy,* vol. 79, pp. 409-421, 2005.

[69] A. Steinfeld, "Solar hydrogen production via a two-step water-splitting thermochemical cycle based on Zn/ZnO redox reactions," *international journal of hydrogen energy,* vol. 27, pp. 611-619, 2002.

[70] W. Gernjak, M. Maldonado, S. Malato, J. Cáceres, T. Krutzler, A. Glaser, and R. Bauer, "Pilot-plant treatment of olive mill wastewater (OMW) by solar TiO photocatalysis and solar photo-fenton," *Solar energy,* vol. 77, pp. 567-572, 2004.

[71] R. Goslich, R. Dillert, and D. Bahnemann, "Solar water treatment: principles and reactors," *Water Science and Technology,* vol. 35, pp. 137-148, 1997.

[72] S. PACES. (2011b). Technology charecterization solar power tower ,availablet www.solarpaces.org/CSP_Technology/docs/solar_tower.pdf.

[73] G. Evans, W. Houf, R. Greif, and C. Crowe, "Numerical modeling of a solid particle solar central receiver," 1985.

[74] P. Fernández and F. Miller, "Assessment of the overall efficiency of gas turbine-driven CSP plants using small particle solar receivers," *Energy Procedia,* vol. 49, pp. 334-343, 2014.

[75] S. S. S. Khalsa, J. M. Christian, G. J. Kolb, M. Rö̈ger, L. Amsbeck, C. K. Ho, N. P. Siegel, and A. C. Moya, "CFD simulation and performance analysis of alternative designs for high-temperature solid particle receivers," in *ASME 2011 5th International Conference on Energy Sustainability*, 2011, pp. 687-693.

[76] M. Röger, L. Amsbeck, B. Gobereit, and R. Buck, "Face-down solid particle receiver using forced recirculation," *Journal of Solar Energy Engineering,* vol. 133, p. 031009, 2011.

[77] J. Hruby, "Technical feasibility study of a solid particle solar central receiver for high temperature applications," Sandia National Labs., Livermore, CA (USA)1986.

[78] M. RÃķger, L. Amsbeck, B. Gobereit, and R. Buck, "Face-down solid particle receiver using forced recirculation," *Journal of Solar Energy Engineering,* vol. 133, p. 031009, 2011.

[79] A. AS, "Augmentation of heat transport in laminar flow of polystyrene suspensions," *J Appl Physics* vol. 46, pp. 3408-3416, 1975.

[80] W. John, Ed., *Principle of enhanced heat transfer*. New York: Wiley & Sons, 1993, p.^pp. Pages.

[81] A. Hunt and C. Brown, "Solar test results of an advanced direct absorption high temperature gas receiver (SPHER)," in *8 Solar World Congress*, 1983, pp. 959-963.

[82] W. Yuen, F. Miller, and A. Hunt, "Heat transfer characteristics of a gas-particle mixture under direct radiant heating," *International communications in heat and mass transfer,* vol. 13, pp. 145-154, 1986.

[83] H. H. Klein, J. Karni, R. Ben-Zvi, and R. Bertocchi, "Heat transfer in a directly irradiated solar receiver/reactor for solid-gas reactions," *Solar Energy,* vol. 81, pp. 1227-1239, 2007.

[84] D. Shi, R. Nicolai, and L. Reh, "Wall-to-bed heat transfer in circulating fluidized beds," *Chemical Engineering and Processing: Process Intensification,* vol. 37, pp. 287-293, 1998.

[85] J. Hruby, R. Steeper, G. Evans, and C. Crowe, "An experimental and numerical study of flow and convective heat transfer in a freely falling curtain of particles," *Journal of fluids engineering,* vol. 110, pp. 172-181, 1988.

[86] M. Rightley, L. Matthews, and G. Mulholland, "Experimental characterization of the heat transfer in a free-falling-particle receiver," *Solar energy,* vol. 48, pp. 363-374, 1992.

[87] P. Falcone, J. Noring, and J. Hruby, "Assessment of a solid particle receiver for a high temperature solar central receiver system," Sandia National Labs., Livermore, CA (USA)1985.

[88] S. W. Churchill and H. H. Chu, "Correlating equations for laminar and turbulent free convection from a vertical plate," *International journal of heat and mass transfer,* vol. 18, pp. 1323-1329, 1975.

[89] A. Zukauskas, *Convective heat transfer in cross flow* vol. 6: Wiley, New York, 1987.

[90] L. Aichmayer, "Solar receiver design and verification for small scale polygeneration unit," 2011.

[91] L. Godson, B. Raja, D. M. Lal, and S. Wongwises, "Enhancement of heat transfer using nanofluids—an overview," *Renewable and Sustainable Energy Reviews,* vol. 14, pp. 629-641, 2010.

[92] Y. Xuan and Q. Li, "Investigation on convective heat transfer and flow features of nanofluids," *Journal of Heat transfer,* vol. 125, pp. 151-155, 2003.

[93] S. Kakaç and A. Pramuanjaroenkij, "Review of convective heat transfer enhancement with nanofluids," *International journal of heat and mass transfer,* vol. 52, pp. 3187-3196, 2009.

[94] J. D. Gabor, "Wall-to-bed heat transfer in fluidized beds," *AIChE Journal,* vol. 18, pp. 249-250, 1972.

[95] A. Costa and G. Macedonio, "Viscous heating effects in fluids with temperature-dependent viscosity: triggering of secondary flows," *Journal of Fluid Mechanics,* vol. 540, pp. 21-38, 2005.

[96] J. Y. Jung, H. S. Oh, and H. Y. Kwak, "Forced convective heat transfer of nanofluids in microchannels," *International Journal of Heat and Mass Transfer,* vol. 52, pp. 466-472, 2009.

[97] Y. Courbariaux, T. Pugsley, and M. Couturier, "Heat transfer between FCC catalyst and an electrically heated horizontal cylinder in a circulating fluidized bed," *The Canadian Journal of Chemical Engineering,* vol. 77, pp. 213-222, 1999.

[98] http://alexis.jtlnet.com/~escoprod/escoproducts.com/html/bk-7_optical_glass.html/25/02/2015.

[99] A. Steinfeld and M. Schubnell, "Optimum aperture size and operating temperature of a solar cavity-receiver," *Solar Energy,* vol. 50, pp. 19-25, 1993.

[100] ASTM, "Terrestrial reference spectra for photovoltaic performance evaluation," American Society for Testing and Materials2003.

[101] http://commons.wikimedia.org/wiki/File:HLR-OSRAM.jpg/25/02/2015.

[102] Nostel, "Preparation and optical characterisation of antireflection coats and reflector materials for solar energy systems," PhD, Faculty of Science and Technology - Solid State Physics, Uppsala University, Uppsala, 2000.

[103] B. Treece, "Brayton- cycle baseload power tower CSP system," in *SunShot Concentrating Solar Power Program Review 2013*, USA, 2013.

[104] S. Chue, "Pressure probes for fluid measurement," *Progress in aerospace sciences,* vol. 16, pp. 147-223, 1975.

[105] E. T. Baker and J. W. Lavelle, "The effect of particle size on the light attenuation coefficient of natural suspensions," *Journal of Geophysical Research: Oceans (1978–2012),* vol. 89, pp. 8197-8203, 1984.

[106] P. Basu, "Heat transfer in high temperature fast fluidized beds," *Chemical Engineering Science,* vol. 45, pp. 3123-3136, 1990.

[107] www.dr- infomaterial/Heat_Flux_Transduvcer.pdf/25/02/2015.

[108] C. Richard, "Investigating the use of concnetrated solar energy to thermally decompose limestone," PhD, School of Mechanical engineering, The University of Adelaide, Adelaide, Australia, 2010.

[109] www.abbascaustralia.com.au/25/02/2015.